2012

FINITE ELEMENT ANALYSIS OF CANCELLOUS BONE

Lucas T. Wilkerson
University of Kentucky, lucas.wilkerson@gmail.com

STUDENT AGREEMENT:

I represent that my thesis or dissertation and abstract are my original work. Proper attribution has been given to all outside sources. I understand that I am solely responsible for obtaining any needed copyright permissions. I have obtained and attached hereto needed written permission statements(s) from the owner(s) of each third-party copyrighted matter to be included in my work, allowing electronic distribution (if such use is not permitted by the fair use doctrine).

I hereby grant to The University of Kentucky and its agents the non-exclusive license to archive and make accessible my work in whole or in part in all forms of media, now or hereafter known. I agree that the document mentioned above may be made available immediately for worldwide access unless a preapproved embargo applies.

I retain all other ownership rights to the copyright of my work. I also retain the right to use in future works (such as articles or books) all or part of my work. I understand that I am free to register the copyright to my work.

REVIEW, APPROVAL AND ACCEPTANCE

The document mentioned above has been reviewed and accepted by the student's advisor, on behalf of the advisory committee, and by the Director of Graduate Studies (DGS), on behalf of the program; we verify that this is the final, approved version of the student's dissertation including all changes required by the advisory committee. The undersigned agree to abide by the statements above.

Lucas T. Wilkerson, Student

Dr. Keith Rouch, Major Professor

Dr. James McDonough, Director of Graduate Studies

FINITE ELEMENT ANALYSIS OF CANCELLOUS BONE

THESIS

A thesis submitted in partial fulfillment of the requirements for
the degree of Master of Science in Mechanical Engineering in
the College of Engineering at the University of Kentucky

By

Lucas T. Wilkerson

Lexington, Kentucky

Co-Directors: Dr. Keith Rouch, Professor of Mechanical Engineering
And Dr. David Pienkowski, Professor of Biomedical Engineering

Lexington, KY

2012

ABSTRACT OF THESIS

FINITE ELEMENT ANALYSIS OF CANCELLOUS BONE

A variety of pathologies exist which increase the likelihood of bone fracture. Present methods for determining the fracture risk of a specific patient are based exclusively on the amount of bone present. While the quantity of bone tissue is correlated with strength, it neglects to account for bone's intricate microarchitecture. To assess the effect of bone quality on strength, a methodology was developed for the structural analysis of cancellous bone biopsies. Thirty biopsies were selected from a pre-existing biopsy bank, and scanned using a SCANCO μCT-40 at a resolution of 30 microns. Cortical bone was removed from the resulting three-dimensional geometry, and the remaining cancellous bone was meshed with solid tetrahedral elements. A linear static uniaxial compression test was performed using ANSYS v14.0 to determine the apparent-level Young's modulus. The maximum von Mises stress was also investigated, but showed poor convergence with increased mesh density. Consistent with the methodology of Pistoia et al., the failure load was assumed to occur when 2% of the bone volume exceeded 7000 μstrain. The results of the finite element analysis compared favorably with known values for cancellous bone strength.

KEYWORDS: Finite Element Method, MicroCT, Human Iliac Bone, Bone Strength, Bone Stiffness

__Lucas Wilkerson__

___Nov. 29, 2012__

FINITE ELEMENT ANALYSIS OF CANCELLOUS BONE

By

Lucas Tyler Wilkerson

Dr. Keith Rouch, Ph.D.
Director of Thesis

Dr. David Pienkowski, Ph.D., M.B.A.
Co-Director of Thesis

Dr. James McDonough, Ph.D.
Director of Graduate Studies

November 29, 2012

ACKNOWLEDGEMENTS

My advisor, Dr. Keith Rouch was instrumental in guiding me through the process of graduate education at the University of Kentucky, and his technical expertise was greatly appreciated throughout the course of my research. Of equal importance on the medical aspects of this project was Dr. David Pienkowski. His direction, judgment, and encouraging words were invaluable to my progress. Vijayalakshmi Krishnaswamy, whose prior work on this subject laid the groundwork for my research, deserves a great deal of recognition for making this possible.

I would also like to thank Dr. Hartmut Malluche for granting me access to his impressive collection of bone biopsies. He, along with Dr. Marie Faugere, provided input throughout my research that was consistently appreciated. I owe Daniel Porter an immense debt of gratitude for teaching me the detailed biopsy archival procedures, and for tolerating my initial ignorance of the medical field. Jonathan Ward deserves a thank you for both his general assistance and his input on the MATLAB code.

Dr. Puleo graciously trusted me with his SCANCO μCT-40, without which my research would not have been possible. Yuan Zou and Bryan Orellana selflessly sacrificed their time to train me on the μCT, for which I am perpetually grateful.

I am also thankful for the mechanical engineering director of graduate studies, Dr. McDonough. His leadership allows the graduate school to thrive, and he personally

reviewed my course selection. The entire Engineering Computer Services team, Kyle Dippery in particular, was essential in keeping the analysis software up to date.

My penultimate expression of gratitude is extended to the University of Kentucky for providing me with two years of financial support through the multi-year fellowship. Without such generous assistance, it is unlikely that I would have pursued a graduate education. Lastly, I must thank my parents for their unfailing support.

TABLE OF CONTENTS

LIST OF TABLES

LIST OF FIGURES

1 Introduction

1.1 Prevalence of Osteoporosis

Osteoporosis is a bone disease characterized by decreased bone mineral density and increased fracture rates. The disease is most prevalent in post-menopausal Caucasian women, but it is present in all ethnicities and age levels. According to the National Osteoporosis Foundation, 50% of women, and up to 25% of men over age 50 will experience an osteoporosis-induced fracture [1]. By 2020, it is estimated that osteoporosis will affect 14 million Americans [2]. With the number of Americans over the age of 65 expected to double from 2010 to 2040 [3], osteoporosis will become an ever more pressing medical problem.

There is no single treatment for osteoporosis. The condition can be prevented and abated by proper intake of calcium and vitamin D [4], and by physical activities which safely increase bone loading [5,6]. However, for advanced cases of osteoporosis, medication is the *de facto* course of action. Hormone replacement therapy, raloxifene, teriparatide, calcitonin, denosumab, and bisphosphonates are all used to combat osteoporosis. Of all of the treatment options, bisphosphonates are the most often prescribed solution [7]. From May 2003 to April 2004, 22 million prescriptions were written for Fosamax (a specific bisphosphonate) alone [8].

1.2 Research Objectives

The high-order objective of this research is to reduce the rate of bone fractures in patients suffering from osteoporosis. As with most non-trivial problems, there are a myriad of ways one may attempt to accomplish the objective. Time could be devoted to creating new medications, understanding present therapies, preventing falls, or an untold number of potentially fruitful endeavors. Work is being done to comprehend the physiopathology of osteoporosis [9], the role of genetics in susceptibility to osteoporosis [10], and in preventing the falls which are often associated with fracture [11].

In this research, the goal of reducing osteoporotic fractures will be fulfilled by investigating the long-term effect of bisphosphonate use on bone strength. Bisphosphonates function by decreasing the resorption of bone. Initially, bone strength is unarguably increased because the net rate of bone formation increases. However, it has been hypothesized that long term use could actually decrease strength due to increased mineralization or accumulation of unrepaired

microdamage [12]. Alteration of micro-architecture has also been shown to be an important factor in bisphosphonate's function [13], and it is the main factor investigated in this work.

If it is shown that long-term bisphosphonate use decreases bone strength, then putting a cap on the duration of bisphosphonate use should decrease the number of fractures seen in the population. If, on the other hand, the null hypothesis cannot be rejected, doctors and patients can be slightly more comfortable with the extended use of bisphosphonate treatment.

In order to assess the effect of bisphosphonate use on bone strength, a method is needed to determine the failure load of bone tissue. Currently, dual-energy x-ray absorptiometry (DXA) is the standard test for diagnosing osteoporosis. The test measures bone mineral density (BMD). The result of the test is a two dimensional image, with each point representing the x-ray attenuation of the corresponding 1-D path through the bone. DXA cannot compute true density, since the bone volume is not known. Instead, the BMD score is based on the cross sectional area of the bone. Other, more invasive tests are occasionally used to evaluate bone strength. If a biopsy is taken, a smorgasbord of parameters can be collected, all of which play a role in bone strength. In concert with tetracycline double labeling [14], a biopsy can determine turnover rate [15], mineralization, collagen cross-linking, trabecular thickness, trabecular separation, hardness, young's modulus, osteoid thickness, and erosion depth.

Unfortunately, the above methods only measure bone strength indirectly. What is needed is a way to determine the stresses and strains inside the tissue in response to load; only then can a failure mechanism be determined. Thankfully, the mechanics of materials is a well-established field, and engineers have been putting the knowledge to good use for decades [16]. So, while the objective is rooted in the medical arena, the means to accomplish the goal is well within the wheelhouse of mechanical engineering.

By developing a finite element model to gage the load capability of cancellous bone tissue, the true effect of bisphosphonate use can be determined. Furthermore, the same finite element method can be used in future studies. Ideally, with high-resolution in-vivo scans, the population may one day benefit from improved identification of at-risk patients.

Figure 1-1: Visualization of Objectives

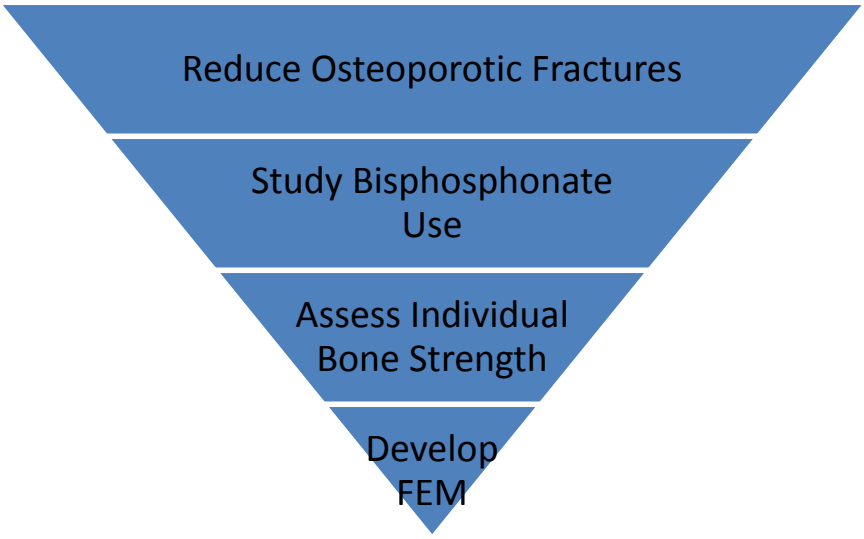

1.3 Motivation

The motivation underpinning this research may seem obvious: to save and improve the lives of those afflicted with osteoporosis. However, what may be less apparent is just how devastating a fracture is for the typical osteoporotic person. After fracturing a hip, 17-33% of patients die with one year of being discharged from the hospital [17]. (To be fair, not all of the deaths can be directly attributed to the fracture [18,19].) Of the patients who survive a hip fracture, less than half regain their previous level of independence [20].

Based on those grave statistics, anything that can be done to reduce the frequency or severity of osteoporotic fractures is well worth the effort. As a purely secondary consideration, preventing fractures would not only improve quality of life, but also save the medical system billions of dollars. It is projected, that by 2025, the US will experience more than 3 million osteoporosis-related fractures per year, at a financial cost of $25.3 billion [1]. While it is crass to put a dollar value on human life, there is no denying that there is an opportunity cost for every dollar spent. Funds spent repairing bone fractures could instead be spent researching heart disease, providing medical treatment to underprivileged children, or engineering advanced surgical devices, all of which would likely save lives.

So, the empathetic motivation has been vividly established, but that alone doesn't justify research. The technical motivation stems from the fact that none of the widely-used bone metrics fully assess the strength of bone. BMD, for example, has been correlated with fracture

risk beyond any doubt [21]. However, the relationship between BMD and bone strength on a population level does not tell us the bone strength of an individual. In fact, current research already indicates that there is significant room for improvement [22,23]. By looking at the microarchitecture of a specific patient's bone, it should be possible to generate a much more accurate estimate of bone strength.

1.4 Study Design

In order to determine the relationship between duration of bisphosphonate use and cancellous bone strength, it is necessary to have bone tissue which has been exposed to the drug for varying periods of time. In an ideal situation, a group of patients who were freshly prescribed bisphosphonates would have high-resolution in-vivo bone scans at the hip prior to their first dose of bisphosphonates. Then, periodically, they would be re-scanned for the next decade of treatment. This would eliminate a host of uncontrolled variables, and allow for a more powerful paired statistical test. In addition to being lengthy and expensive, the study described would also be impractical with present technology. In-vivo scanning by peripheral quantitative computed tomography (pQCT) is currently limited to scanning at the distal radius and tibia.

In order to work within the limitations of microCT scanning, research duration, and cost, it was decided to perform the study on previously extracted bone biopsies rather than new patients. For decades, Dr. Hartmut H. Malluche, MD of the University of Kentucky has been cataloging iliac crest biopsies. The biopsies are embedded in acrylic, preserving them indefinitely. They require no special storage conditions, and are organized using the system depicted in Figure 1-2. A typical biopsy is shown in Figure 1-3.

Figure 1-2: Biopsies Collected During Year 2005

Figure 1-3: A Representative Biopsy

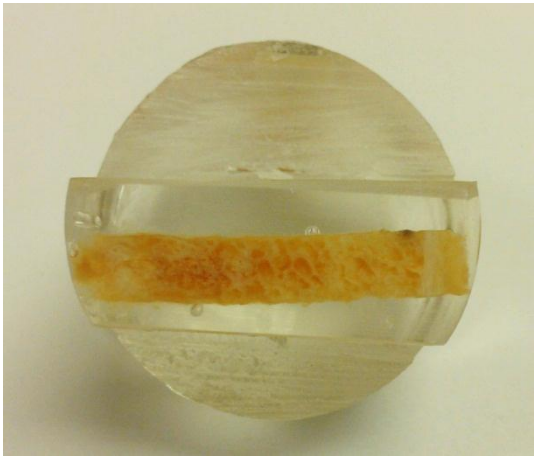

The total collection has over 8000 biopsies, but this study selected from a much smaller set of approximately 700 patients. The reduction is primarily the result of eliminating biopsies extracted prior to 1997. (The FDA approved the use of Fosamax in 1995.) While the older biopsies are still valid for study, they have less detailed documentation and are unlikely to contain bisphosphonate patients. The small subset is also attributable to the fact that only osteoporotic patients were considered for study.

From the set of 700 osteoporotic biopsies, three sets of 10 groups were chosen. The first set had been diagnosed with osteoporosis, but had not yet taken bisphosphonates. The second set had been using bisphosphonates for one to five years at the time of the biopsy. Finally, the third set had more than 5 years of bisphosphonate use at the time of the biopsy.

2 Background

Due to the interdisciplinary nature of this work, an overview of both the medical aspects and the engineering aspects is in order. In an effort to cater to the widest possible audience, the material starts at a fairly basic level. Those proficient in both disciplines, namely biomedical engineers, may wish to skip to the Prior Work section.

2.1 Overview of Bone

2.1.1 Anatomy

2.1.1.1 Gross Anatomy

At the macroscopic level, bones are responsible for resisting routine locomotive forces and protecting vital soft tissue during traumatic events. The adult skeleton contains 206 bones, and has a dry fat-free mass 6-7% of total body mass [24]. Bones are classified into 5 categories based on their shape: long, short, flat, sesamoid, and irregular. Long bones, such as the humerus, are further subdivided into epiphyseal bone at the ends, and diaphyseal bone along the central portion (Figure 2-1). The carpals, connecting the hand and forearm, are short bones. They have no one dimension that dominates the others. The biopsy location in this study, the ilium, is categorized as a flat bone. Flat bones generally offer protection, or an expansive site for muscular attachment. Sesamoid bones protect tendons that have to span over joints. Finally, the irregular classification is nothing but a catch-all for the misfits, like vertebrae.

Figure 2-1: Long Bone[1]

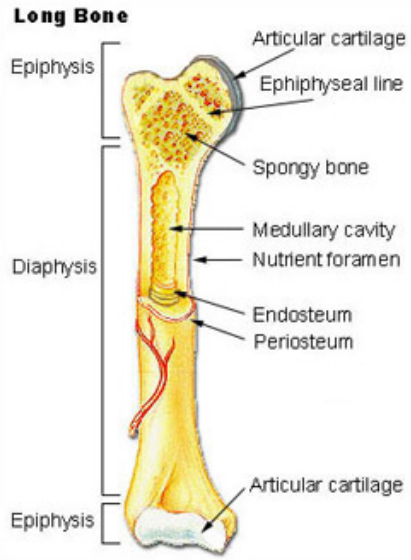

There are two types of bone based on the amount of structural material present. Compact bone is dense, low-porosity (5-10%) bone tissue that forms the outer shell of bones [25]. Because it is located at the cortex, it also goes by the name cortical bone. Cortical bone comprises approximately 80% of total bone mass, and is thickest in the shaft of long bones. Its role is primarily structural.

Cancellous (also spongy or trabecular) bone forms the interior volume of bone encompassed by the cortical shell. (Although, the shafts of long bones are notably absent of cancellous bone. The space—known as the medullary cavity—is reserved for fatty yellow marrow.) The porosity of trabecular bone is typically 75-95% [25]. The space is commonly filled with red marrow, which is responsible for the creation of blood cells. Unlike cortical bone, whose structure appears more or less uniform without magnification, cancellous bone looks like an open-cell foam. The rods connecting the nodes of spongy bone are termed trabeculae (sing. trabecula). They can exhibit a wide range of shapes, but are most often 0.1 to 0.2 mm in diameter and on the order of 1 mm long. The exact architecture of the bone can vary widely on a continuum from rod-like to plate-like.

[1] Public Domain: http://training.seer.cancer.gov/anatomy/skeletal/classification.html

2.1.1.2 Microanatomy

At the microscopic level cortical bone is composed of osteons running down the longitudinal axis of the bone. Each osteon is a cylindrical unit composed of concentric layers (lamellae) of bone tissue. At the center of the osteon is a hollow core, the Haversian canal, which provides a passageway for blood vessels and nerves. The Haversian canals are connected transversely by Volkmann's canals, creating a network throughout the bone. Osteons have an outer diameter of roughly 0.2-0.3 mm, and an inner diameter of about 0.05 mm. The lamellae range in thickness from 3 to 10 microns. All of the structures are shown (not to scale) in Figure 2-2.

Trapped between the lamellae are osteocytes, mature bone cells. The space they reside in is called a lacuna, and is about 8 microns in the long axis, but varies from 3-20 microns [26]. The lacunae are connected via a network of narrow passageways termed canaliculi. They are about 225 nm in width, and vary in size depending on whether they are circumferential (between lamellae) or radial (crossing lamellae) [27].

Cancellous bone, like cortical bone, is composed of lamellae. Unlike in cortical bone, the lamellae are not arranged into osteons. They form irregular patterns just a few layers thick. Aside from their arrangement, the lamellae themselves are the same in trabeculae and osteons. The load-bearing extracellular material of bone is essentially the same regardless of where it is found. The material is a composite of organic proteins and inorganic mineral (hydroxyapatite: $Ca_{10}(PO_4)_6(OH)_2$). The proteins are 90% collagen, with type I collagen fibers being the dominant variety. The fibers are oriented in the same direction within a given lamella, but lamella orientations differ, not unlike the layers in a sheet of plywood. Collagen has a low elastic modulus (around 6 GPa), but is has a large strain at failure, making it tough. Bone mineral is stiff and brittle, and it accounts for three fourths of dry-bone weight. Single crystals of hydroxyapatite have a modulus of 54-79 GPa [28]. (For comparison, the Young's modulus of aluminum is 70 GPa.) The modulus of bone tissue fluctuates based on patient, anatomical site, and orientation, but generally falls around 10-20 GPa. The failure stress varies from ~50MPa in tension perpendicular to the collagen fibers, to ~190 MPa for compression parallel to the fibers.

It is important to bear in mind that when mechanical properties are reported for cancellous bone they are often given at the apparent level, which treats the entire structure of the bone like its own homogeneous material. The resulting values for young's modulus and strength are drastically reduced from the material level due to the reduced volume fraction. That being said,

there is some evidence that cancellous bone is more compliant than cortical bone, even at the material level [29].

Figure 2-2: Cross Section of Diaphyseal Bone[2]

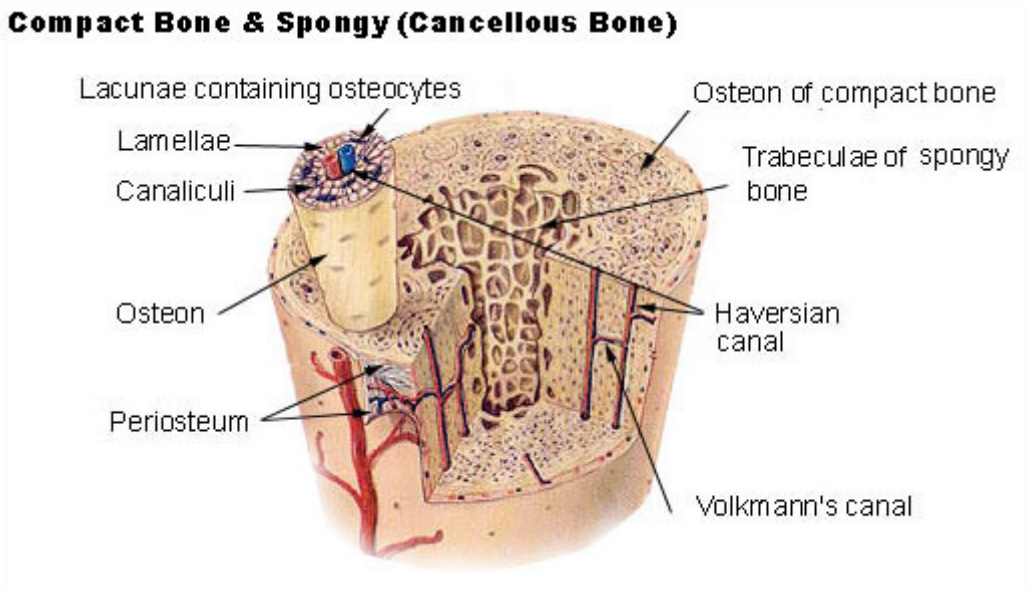

2.1.2 Physiology

Bone is often thought of as static by the uninitiated. To the contrary, it is a dynamic organ that is constantly regenerating itself. The rate of bone remodeling (or turnover) is dependent on anatomical location and bone type. In normal adults, 4-5% of cortical bone is renewed each year. The space between osteons is filled with interstitial lamellae, which are fragments of previously whole osteons that were partially destroyed by remodeling. Trabecular bone is remodeled to the tune of 20-25% per year. Bone remodeling repairs microcracks that appear in bone as the result of normal activity. It also adjusts the amount of bone by location depending on the applied loading, which is why astronauts lose bone mass in space and why athletes have increased bone density tailored to their sport's demands. (The concept of bone adapting to stress is known as Wolff's law.) Lastly, remodeling is used to heal fractures. Initially, the collagen matrix of freshly-repaired bone is an unorganized web. The so-called woven bone is generated quickly, but it is weaker. Remodeling gradually replaces the woven bone with lamellar bone.

[2] Public Domain: http://training.seer.cancer.gov/anatomy/skeletal/tissue.html

The process of bone remodeling starts with activation, which may be brought on by a fatigue crack severing bone lining cells (and osteocytes). After detecting the biochemical signal of the distress, stromal cells differentiate into osteoclasts. Osteoclasts are large multi-nucleated cells which resorb bone mineral for 2-3 weeks before undergoing apoptosis. Their ruffled edge and specialized proteins allow them to seal against the surface of exposed mineralized bone. Once connected, they use carbonic acid to dissolve the extracellular matrix (ECM). The next stage, reversal, takes about 2 weeks, during which time the osteoclasts undergo apoptosis. Formation begins with the creation of osteoblasts from stromal cells. The osteoblasts fill the resorption pit with osteoid, which is new unmineralized bone. Osteoid is a network of predominantly parallel cross-linked collagen fibers which lay the framework on which mineral will later be deposited. As the osteoblasts work, some of them trap themselves within the osteoid. When the bone matures, those cells become the osteocytes described earlier. Osteoblasts left at the surface of the bone become bone lining cells. The formation phase is the most time-consuming part of bone remodeling, taking anywhere from 3 to 6 months. However, the bone will continue to gather mineral and increase in hardness for years. Collectively, bone remodeling cells form a BMU, or basic multicellular unit. The time required to complete a remodel at a particular site is the bone remodeling period.

2.1.3 Pathology

Due to the complex signaling pathways responsible for regulating bone turnover, bone is susceptible to several pathologies. By far, the most common is osteoporosis. The standard definition of osteoporosis in women, as set by the World Health Organization, is having a bone mineral density (BMD) t-score of -2.5 or less. The t-score is the number of standard deviations the patient BMD lies from the mean BMD of a 20-year-old reference population. Z-scores are also used in diagnosis; they reference an age-matched population.

Osteoporosis may be sorted into two categories: primary and secondary. Primary osteoporosis occurs naturally due to the inevitable decline of bone mass after age 30. It is a natural, if unpleasant, part of the human condition. Primary osteoporosis is itself separated into two more groups: Type I and Type II. Type I, or high-turnover, osteoporosis presents itself before the age of 70 and is most common in post-menopausal women. Type II, or senile, osteoporosis is observed in patients over 70 and is caused by a gradual thinning of cancellous and cortical bone.

Finally, secondary osteoporosis has a clearly discernible cause, such as the use of corticosteroids or anticonvulsants.

This research focuses primarily on type I osteoporosis, since it is the most prevalent variety. The precipitous decline in estrogen levels after menopause adversely affects bone turnover. Estrogen is at least partially responsible for osteoclast apoptosis, and for suppressing the production of osteoclastogenic cytokine [30]. With more osteocytes being formed, and fewer osteocytes dying on command, the balance of bone resorption to formation is set up for the net destruction of bone. Treatments generally serve to either increase osteoblast activity, or decrease osteoclast activity. Bisphosphonates take the latter approach.

2.1.4 Bisphosphonate Function

Bisphosphonates are similar to naturally-occurring pyrophosphate, but with the central oxygen atom replaced by a carbon atom and two side chains. Because bisphosphonates have an affinity for calcium, they selectively target the ECM of bone. When osteoclasts begin the remodeling process, they ingest the bisphosphonates, which leads to early apoptosis by interfering with the normal uses of pyrophosphate. The decreased osteoclast activity slows the rate of bone loss, thereby reducing the risk of fractures.

Depending on the chemical composition of the two side chains, bisphosphonates have potencies that vary by orders of magnitude. Non-nitrogen-containing varieties were the first to be developed. Etidronate, the first bisphosphonate used to treat osteoporosis, had a methyl group and a hydroxyl group. It interrupts the Krebs cycle of osteoclasts by forming a non-functional version of ATP. Using etidronate as a unit of potency, other non-N containing drugs were developed with potencies of 10. Second generation bisphosphonates contain nitrogen in their side chains, and have potencies ranging from 100 (pamidronate) to 1000 (ibandronate). Their mechanism of action is to inhibit farnesyl pyrophosphate synthase in the HMG-CoA reductase pathway. Third generation bisphosphonates have a heterocyclic nitrogen-containing ring in one of their side chains. Risefronate has a potency of 2000, and zoledronate a potency of 10,000. The type of bisphosphonate was not a controlled variable in this research, but the majority of non-control patients were on second generation bisphosphonates at the time of biopsy.

Oral bioavailability of bisphosphonates is poor (<5%), but of the dose that makes it to the bloodstream, approximately half is absorbed by the bone with the remainder being expelled in

urine [31]. Once in bone, bisphosphonates can remain there for up to 10 years [31]. Because oral intake can upset the stomach and esophagus, ibandronate is available as a quarterly injection, and zoledronate as a yearly injection. The long intervals between treatments are possible because of bisphosphonate's permanence in the ECM of bone tissue.

There is widespread agreement that bisphosphonates are beneficial to bone strength in the short term. However, there is dissonance in the community about their efficacy and safety in the long term (>5 years). Suspicions were raised when an increased occurrence of atraumatic fractures were observed in bisphosphonate patients. An atraumatic fracture is defined as any fracture occurring during normal activities. Any event more serve than a fall from standing height is considered traumatic. For the most part atraumatic fractures are synonymous with low-energy fractures, pathologic fractures, spontaneous fractures, fragility fractures, fatigue fractures, and insufficiency fractures.

The observation of low-energy fractures in long-term patients does not prove that bisphosphonates are the cause, but the correlations are striking nonetheless. A retrospective review by Neviaser et al. in 2008 identified 70 low-energy fracture patients admitted to the Hospital for Special Surgery [32]. Twenty-five of the patients were using alendronate, of which 19 presented with "a simple, transverse fracture with a unicortical beak in an area of cortical hypertrophy". Only one of the 45 non-bisphosphonate patients showed a similar fracture pattern. The 19 patients with the fracture pattern had been taking alendronate for an average of 6.9 years, compared to only 2.5 years for the 6 patients without the pattern ($p=0.002$). Atypical femoral fractures have been observed in bisphosphonate patients by other researchers as well, notably Meulen and Boskey [33].

It has been hypothesized that the rash of atraumatic fractures may be the result of unrepaired microdamage. With less osteoclast activity, the cracks that naturally form as a part of daily activities cannot be repaired at the necessary rate. As time passes while on bisphosphonate treatment, it is suspected that the cracks proliferate in number, increase in length, and coalesce. Eventually, the accumulation of microdamage results in global failure. In concert with the microdamage, changes are observed in the microarchitecture of the cancellous bone. Both factors play a role in determining overall bone strength.

2.2 Basics of Finite Element Analysis

The finite element method (FEM) is an approach for solving partial differential equations over geometrically complex domains. The method works by solving the equations over a simple domain, a rectangle for example. By combining many rectangles, it is possible to create complex shapes. Using small enough rectangles, any object can be well-represented, just as pixels can characterize an image. The simplified domain is called an element, and a finite number of them are used to form the global geometry. Depending on the problem at hand, elements may be lines, triangles, quadrilaterals, tetrahedrons, hexahedrons, or any shape which allows the PDE to be solved.

The phrase "finite element method" was first coined by Ray W. Clough in 1960, but the work of Argyris, Courant, Turner, and Zienkiewicz all contributed to the method's development [34]. Today, FEM has been applied to PDEs for heat transfer, fluid flow, and electromagnetic fields, but it was originally developed for the analysis of aircraft structures. The method has enjoyed widespread use to determine stress and strain in complex structures [35], and when applied correctly it closely matches experimental data [36]. The behavior of most structural engineering materials is approximated by the equations of linear elasticity.

The governing equations of linear elasticity are the equations of motion, the strain-displacement relations, and the constitutive equations. Using indicial notation, the equations of motion reduce to the following for static problems:

$$\sigma_{ji,j} + F_i = 0$$

The strain-displacement relation is given by:

$$\varepsilon_{i,j} = \frac{u_{i,j} + u_{j,i}}{2}$$

The constitutive relations describe the interaction of stress and strain. For an isotropic material:

$$\begin{bmatrix} \varepsilon_{xx} \\ \varepsilon_{yy} \\ \varepsilon_{zz} \\ 2 \cdot \varepsilon_{xy} \\ 2 \cdot \varepsilon_{xz} \\ 2 \cdot \varepsilon_{yz} \end{bmatrix} = \begin{bmatrix} 1/E & -\nu/E & -\nu/E & 0 & 0 & 0 \\ -\nu/E & 1/E & -\nu/E & 0 & 0 & 0 \\ -\nu/E & -\nu/E & 1/E & 0 & 0 & 0 \\ 0 & 0 & 0 & 1/G & 0 & 0 \\ 0 & 0 & 0 & 0 & 1/G & 0 \\ 0 & 0 & 0 & 0 & 0 & 1/G \end{bmatrix} \cdot \begin{bmatrix} \sigma_{xx} \\ \sigma_{yy} \\ \sigma_{zz} \\ \sigma_{xy} \\ \sigma_{xz} \\ \sigma_{yz} \end{bmatrix}$$

To calculate the element equations, the variational (weak) formulation of the governing differential equation is first developed. The weak form is the result of multiplying both sides of the equation by an arbitrary weight function and integrating by parts to "move" differentiation from the unknown function to the weight function. The solution is then assumed to have a pre-determined form. For instance, in a two dimensional problem the solution between the nodes may be assumed to be a straight line. Based on that pretense, the solution to the governing equation is determined solely by the values at the nodes. However, that simplified piece-wise solution will not satisfy the governing equation at every point, which is where the weight function comes into play. Using the Ritz method, the solution is made to satisfy the weak formulation at the nodes by manipulation of the weight function. The equations that result from imposing the nodal values are the algebraic element equations. (Alternatively, the element equations can be derived based on energy principles for structural problems.)

With the element equations in hand, the relationship between force and displacement can be written for every element in the domain. The local equations contain too many unknowns to be solved, so the equations are combined and rewritten in terms of global nodes. Boundary conditions (known nodal displacements) are then applied to the model and the equations are solved.

2.3 Prior Work

2.3.1 Bisphosphonate Studies

There have been a plethora of studies performed to measure the effectiveness and safety of bisphosphonate treatment. A 2009 review of bisphosphonates by Bilezikian stated that "trial extensions of up to 10 years with alendronate and 7 years with risedronate have shown that efficacy is maintained during long-term treatment" [37]. In a separate study, Pazianas et al. concluded that all approved bisphosphonates reduce the risk of both vertebral and non-vertebral fractures [38].

On the other hand, there is evidence to suggest that bisphosphonates may lose efficacy, or potentially even be unsafe with long-term use. Allen and Burr have done extensive research on the effect of alendronate treatment in canines. One of their more benign findings was that alendronate treatment did not continue to decrease trabecular stresses after 1 year of treatment [39]. More disconcerting is that, when adjusting for aBMD, 1 year of alendronate

treatment reduced bone's energy to failure in beagles [40]. However, it is unknown exactly how a decrease in tissue-level properties affects whole-bone strength [41].

Research on human subjects has also revealed some cause for concern regarding long-term use. In a press release on October 13th, 2010, the FDA announced that there may be an increased risk of atypical femur fractures after bisphosphonate use for more than 5 years [42]. Because bisphosphonates remain in the bone after treatment, they continue to provide some level of effect after patients discontinue use. Based that fact, and on suspicions of long-term detriment, several studies have suggested taking a "drug holiday" [43,44]. The start time and duration of the suggested holiday depend on patient specifics, but 5 years was a common recommendation for patients at a mild fracture risk. The presence of this somewhat arbitrary 5-year value in the literature is what dictated the division between short and long-term groups in the present research.

The role of microdamage in bone strength, and specifically in bisphosphonate patients, has been extensively studied. Yet, there is still no way to quantify the effect microcracks have on whole bone strength. Research has been done which quantifies the amount of microdamage and then determines bone strength by experiment, but there is no established technique to predict strength from microdamage information. It is difficult to isolate the contribution of microdamage to whole bone strength due to confounding variables like degree of mineralization and microarchitecture [45]. There is evidence that bisphosphonates do indeed lead to unrepaired microdamage accumulation in dogs [45,46]. As is to be expected there is evidence to the contrary as well. Chapurlat et al. have observed from transiliac biopsies in humans that long-term bisphosphonate use does not lead to increased microdamage [47]. Because of the difficulty of assessing the influence of microdamage on bone strength, and the impractical nature of measuring the three dimensional geometry of a crack, microdamage was not incorporated into the finite element model of this thesis.

2.3.2 The FEM in Medical Studies

As previously mentioned, the finite element method is not a new tool, and the medical field was not slow to adopt it. It has been used to study knee replacement, ear acoustics, car crash injuries, the mechanics of the heart, and cell dynamics. Concerning cancellous bone, current FEA-based research can be categorized by the resolution of the method used to generate the geometry.

In order to have a truly representative model of bone, the resolution must be small enough to capture the microarchitecture. The importance of architecture in the strength of cancellous bone is difficult to overstate. Improved microarchitecture leads to increased bone strength in rats [48], poor architecture has been seen in women with idiopathic osteoporosis [49], and low bone strength in turner syndrome patients has been linked to poor microarchitecture [50]. Without a small enough resolution, the input of trabecular connectivity, width, spacing, and orientation are all lost.

Those technologies with the ability to scan the largest areas, such as quantitative computed tomography (QCT) also have the lowest resolutions. As a result, they cannot model the microarchitecture of the cancellous bone. Instead, they treat cancellous bone like a solid and weigh the material properties of each voxel-element based on the average radiodensity at that location. Using QCT with a cubic voxel size of 1.5mm, Amin et al. found that "FE-derived estimates of proximal femur strength are comparable in determining the probability of prevalent overall and osteoporotic fractures to total hip aBMD or vBMD" [51]. At 7T field strength, μMRI can achieve a resolution of 137 x 137 x 410 μm^3, which is sufficient to capture some microarchitecture [52]. Though, it leaves a lot to be desired seeing as how trabeculae are often thicker than 137 μm.

All of the methods used to achieve finer resolutions sacrifice field of view to do so. The next step down in the continuum is high-resolution peripheral computed tomography (HR-pQCT). Like QCT and MRI, HR-pQCT can be used to measure in-vivo bone geometry, but it is limited to the extremities. It is capable of resolutions in the neighborhood of 80 μm. Despite some trabeculae being less than 80 μm in diameter, HR-pQCT has produced many promising results. Boutroy et al. performed a finite element analysis on the distal radius of postmenopausal women and found that FEA may offer information about fracture risk not provided by BMD or architectural parameters [53]. Pistoia et al concluded that microFE is a better predictor of bone failure than DXA measurements and structural parameters combined [54]. Since HR-pQCT has been established as a respectable method for mechanical analysis of bone, it has been used to study osteoporosis, bisphosphonates, and other osteoporosis treatments. However, few, if any, have focused on the long-term effects of bisphosphonates.

To obtain better resolution than HR-pQCT can offer, it is necessary to switch to a microCT specimen scanner. The resolution acquired by a specimen scanner depends on the size of the

object being scanned. In the case of the SCANCO microCT 40, the best resolution is around 8 µm (10% MTF) at a sample diameter less than 12.3mm. The SkyScan2011 has a resolution of 0.4 µm (10% MTF), but the sample diameter must be less than 1mm. Of course, since all specimen scanners require human tissue to be ex-vivo, the relevance of FEA is slightly diminished. The bone could simply be physically tested to obtain true force-displacement curves. FEA is still of some benefit because physical testing can only be completed to failure once, whereas FEA can run as many simulated loading cases as desired. Obtaining a large, i.e. representative, sample of bone for analysis typically requires using animals or cadavers, both of which have their disadvantages. Dead bone cannot be labeled with tetracycline to determine bone turnover parameters, and any animal study cannot be directly applied to humans. To fix both of those problems, at the cost of total bone volume, human bone biopsies can be studied. However, relatively few finite element studies use biopsies as their main object of study, and even fewer are focused on bisphosphonate duration. This is unfortunate, because Harrison et al. have observed excellent correlations between microCT-derived FEA and experimental results when studying ovine trabecular bone [55].

To summarize, the finite element method is a firmly established weapon in the medical research arsenal. The type of finite element model developed depends on the resolution of the scan, and all else equal, higher fidelity results are obtained at higher resolutions. The finite element method has been applied to the study of bone before, but little work has been done regarding the FE analysis of ex-vivo bone biopsies from long-term bisphosphonate patients.

3 Methodology

3.1 Selection Criteria

Of the roughly 700 osteoporotic biopsies eligible for participation in the study, hundreds had to be rejected based on the controlled variables (and/or lack of necessary metadata). Restricting the study to post-menopausal patients reduced the candidate pool by 223. Applying the constraint of non-diabetic patients further lowered the number of eligible biopsies by 194. An additional 20 patients were rejected due to a history of smoking, and eight were removed due to use of Forteo. After applying all of the filters, only 87 patients with low-turnover osteoporosis were available. Of those 87 patients, 16 had no history of bisphosphonate use, 29 had between one and five years of bisphosphonate use, and 22 had more than five years of bisphosphonate use. (The balance lacked information or had less than 1 year of use.) Lastly, the three experimental groups were selected such that there was no statistically significant difference in patient age.

The controlled variables were maintained, at the sacrifice of sample size, because they all have an effect on bone strength [56], and potentially on the efficacy of bisphosphonates. By reducing as many of the confounding factors as possible, it was hoped that the small sample size could yield useful results. Inconveniently, the sample sizes were further reduced by the fact that not all of the biopsies were suitable for structural analysis. The ideal biopsy was a right circular cylinder, comprised primarily of cancellous bone, similar to that shown Figure 3-1. Deviations from the ideal included presence of excessive cortical bone (Figure 3-2), tapered geometry, curved geometry, and fragmented pieces.

Figure 3-1: Candidate for Analysis

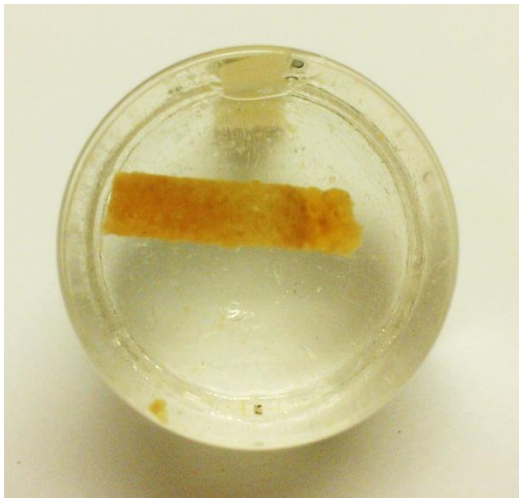

Figure 3-2: Poor Quality Biopsy

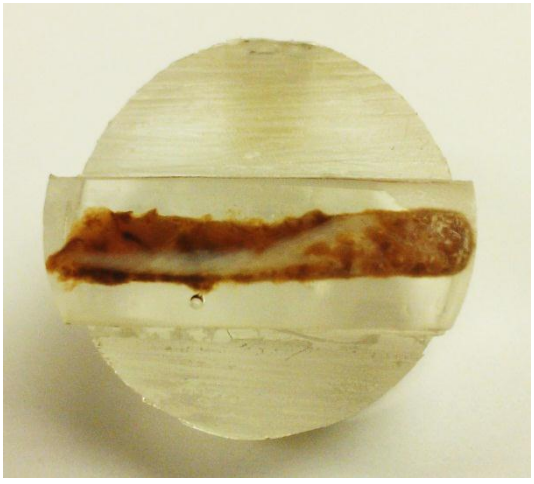

Having removed all of the ineligible biopsies, and matching as closely as possible for age, the final result was three groups of 10 biopsies. A summary is presented in Table 3-1, and the complete set of biopsy metadata can be found in **Appendix F**.

Table 3-1: Experimental Groups

	Age (Years)		Duration (Years)	
Group	Mean	SD	Mean	SD
Control	57.1	11.03	0	0
Short Term	58.2	2.62	2.38	1.08
Long Term	60.6	4.60	7.75	2.82

To summarize, the controlled variables were: gender, menopause, history of smoking, Forteo use, turnover (low), and age. As a result of these restrictions, ethnicity (Caucasian) happened to be constant across the experimental groups. The uncontrolled variables of interest were: exercise frequency, bisphosphonate dosage, calcium intake, ethanol abuse, fracture history, use of hormone replacement therapy, use of proton-pump inhibitors, presence of mineralization defect, and oophorectomy status.

3.2 Biopsy Preparation

The biopsies were not collected specifically for this study. As previously stated, they were a pre-existing resource. Nonetheless, it is necessary to know how they were collected in order to grasp the context of the results. All biopsies were taken from the ilium (Figure 3-3). Most were vertical biopsies extracted from the iliac crest, but a minority was transiliac.

Figure 3-3: Pelvic Girdle[3]

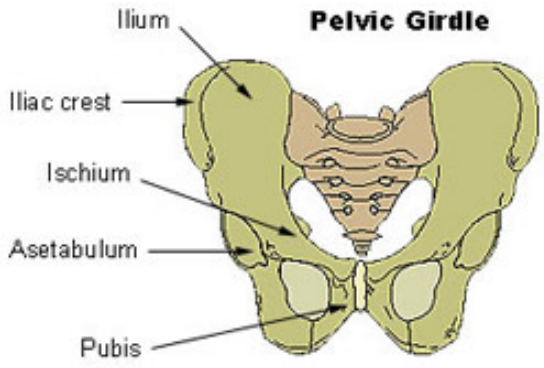

[3] Public Domain: http://training.seer.cancer.gov/anatomy/skeletal/divisions/appendicular.html

After being extracted, the "bone samples were fixed with ethanol at room temperature, dehydrated, and embedded in methylmethacrylate" (Malluche et al., 2012). Polymethylmethacrylate (PMMA) is more commonly known as acrylic, but also goes by the trade names Plexiglas, Perspex, and Lucite.

Note that some of the biopsies were cut roughly in half in order to perform histological analysis (Figure 1-3). The reduction in usable volume is a hindrance to the finite element analysis, but it was unavoidable. In the future, microCT scans should be performed prior to preparing the biopsy for histology.

3.3 MicroCT Scan

3.3.1 Overview

Once the biopsies were embedded in acrylic, they were processed using a SCANCO microCT 40. The machine itself is a desktop device, weighing approximately 150 kg. For a sense of scale, refer to Figure 3-4.

Figure 3-4: MicroCT Instrumentation

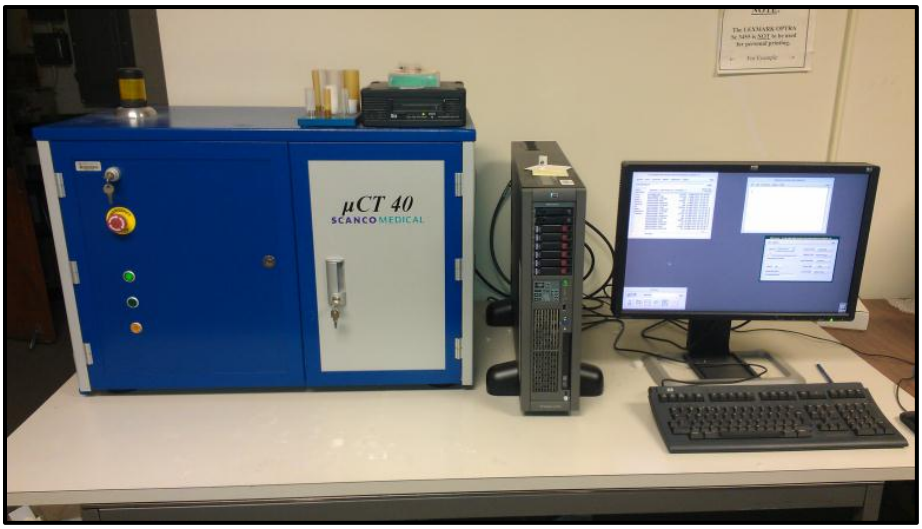

The three-dimensional representation of the biopsy is created by first passing a small-angle cone-beam of x-rays through the sample. As the x-rays travel through the biopsy, the bone mineral absorbs the radiation at a higher rate than the acrylic around it. After finishing their journey through the specimen, any remaining x-rays arrive at a scintillator, which converts the x-rays into visible light. The visible light is then converted into an electronic image using the now-

commonplace charge coupled device. From any one perspective, the resulting projection would not be particularly useful. So, the biopsy is rotated 360 degrees as many images are taken. For each slice location, this collection of images is compiled into a sinogram, which is a physical analog for the Radon transform of the slice. (Mathematically, an infinite number of projections are required, but a reasonable degree of accuracy is obtained from a finite number of scans.) Figure 3-5 depicts a sinogram from one of the biopsies in the study.

Figure 3-5: Sinogram of B02 (Slice 50)

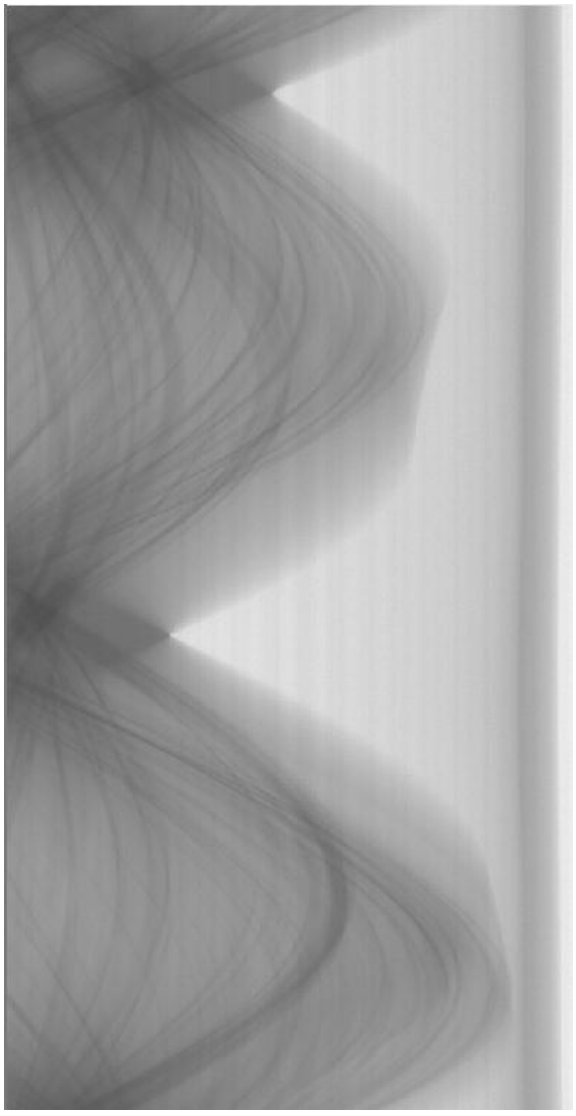

In order to reconstruct the geometry of the cross-section, the inverse Radon transform is performed on the sinogram. Each pixel in the resulting cross-sectional image is a measure of the radiodensity of that portion of the sample. The entire image generating process is repeated for

each desired layer, resulting in a large collection of 2-D information. Since the layers are spaced close together in relation to the resolution of the images, it is feasible to render the 3-D bone volume. The process of converting the slices into a volume can be accomplished by a variety of techniques, the details of which are beyond the scope of this thesis.

3.3.2 Detailed Procedure

In order to perform the scan, first an appropriate sample holder had to be selected for the potted biopsy. SCANCO provides sample holders in both PMMA and PEI materials, with the latter offering better chemical resistance and a wider temperature range than the former. Since the biopsies in this study were a room temperature solid, either material was permissible. The holders also come in an array of diameters, from 12.3mm to 36.9mm. The acrylic block had an outer diameter of roughly 16mm, so the 20.5mm sample holder was selected. In Figure 3-6, the sample holder, complete with biopsy, has been loaded into the microCT.

Figure 3-6: Sample Loaded into µCT Scanner

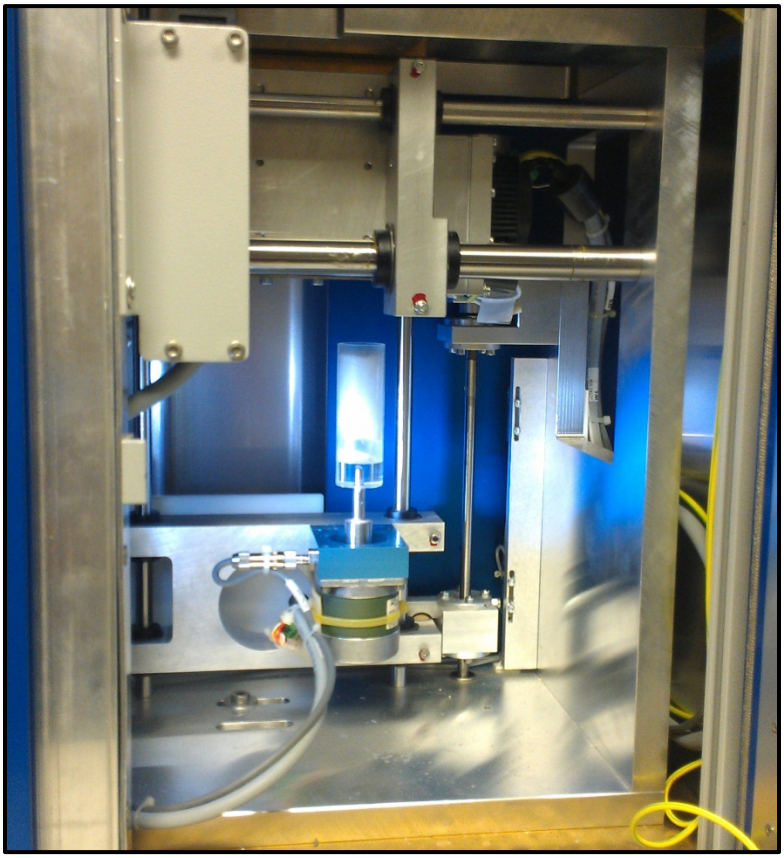

It is important to fully constrain any motion between the sample and the sample holder. The sample holder spins as x-ray projections are gathered, and during the computed tomography it is assumed that the specimen rotates with the holder. In order to fix the biopsy to the holder, a piece of foam was inserted into the sample holder. The foam was oversized for the diameter of the tube, and the friction from the resulting interference fit was sufficient to apply a compressive force onto the top of the biopsy.

Once loaded into the microCT, a quick scout view was performed to define the portion of the sample holder which should be scanned. The thinner the scout view region, the faster the subsequent full-resolution scan will be completed. Figure 3-7 shows a representative scout view with the biopsy, acrylic, and sample holder visible.

Figure 3-7: Scout View of Biopsy B22

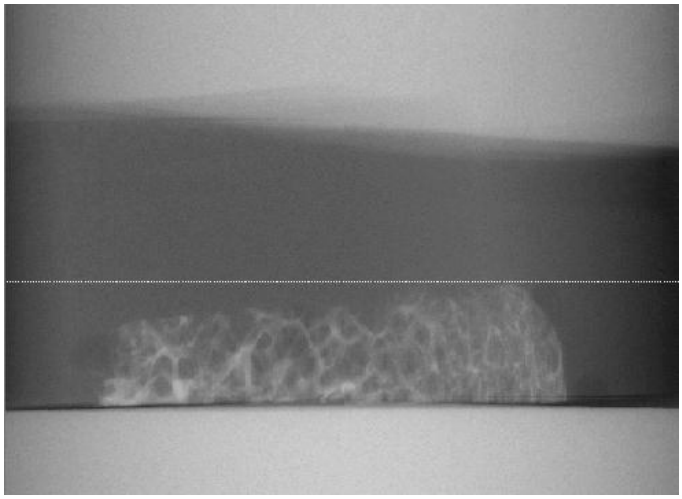

Before starting the scan, a control file must be defined and selected. Figure 3-8 shows the input window for control file creation. The first section dictates the scout view settings, which are predominantly a matter of convenience. The settings do not affect the final scan geometry. The central section contains the most critical settings, chiefly the field of view (FOV) and the resolution. The FOV must not be less than the diameter of the sample holder, or else the instrumentation will collide with the object under study. For this study, the FOV was set at 30.7 mm, and the resolution at 1024x1024 pixels. The resulting voxel size is 30 microns. A higher resolution could have been obtained, but was not used on the recommendation of fellow microCT users. Naturally, the higher resolution scans take more time, and so do all of the

secondary operations. They also require vastly larger amounts of memory. The final section of the input control file is reserved for calibration and evaluation. Calibrations were performed as regularly scheduled, independent of this research, and the evaluation was selected at a later stage.

Figure 3-8: Control File Settings

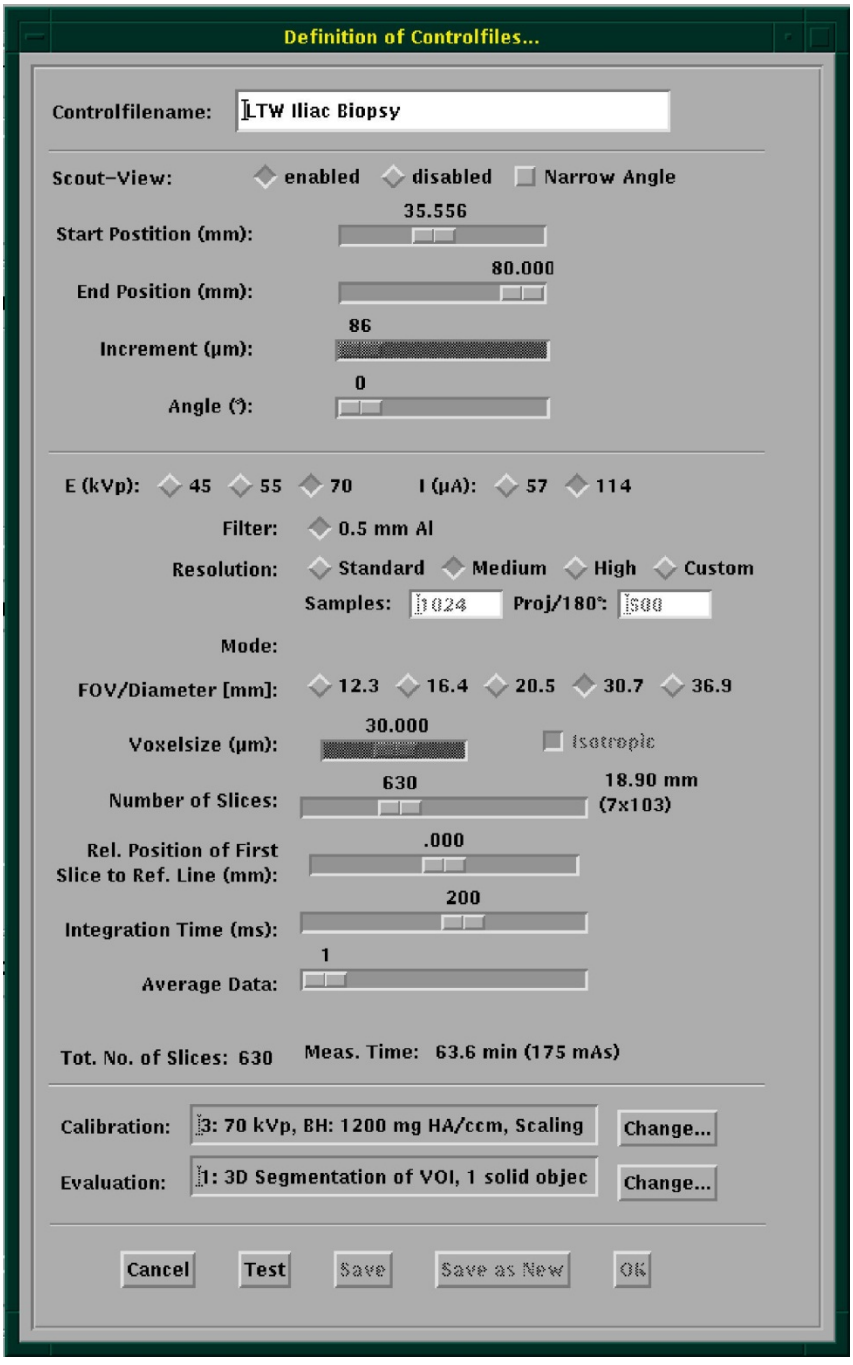

For the settings described, a typical biopsy (3mm, 100 slices) required approximately 15 minutes to scan. Having completed the scan, the individual slices are displayed from SCANCO's evaluation window.

Figure 3-9: Evaluation Window

From this window, two major objectives are accomplished. First, the region of interest (ROI) is defined. Secondly, the threshold between bone and acrylic is established. To demarcate the region of interest, lines were hand-drawn around the biopsy. Thankfully, this is only necessary on a subset of slides. Provided the cross section does not change too drastically, the SCANCO software can morph the ROI from non-consecutive slices onto the set of bounded slices. For STL file creation there was no effort made to contour the biopsies. As long as the ROI contained the entire biopsy the STL would also contain all of the geometric information. However, for calculation of structural indices, an overly large ROI would not be acceptable. For instance, it

would greatly reduce BV/TV. To calculate structural indices, the ROI encompassed only the trabecular bone. Figure 3-10 shows the cancellous ROI defined on a specific slice.

Figure 3-10: Region of Interest, Slice 48

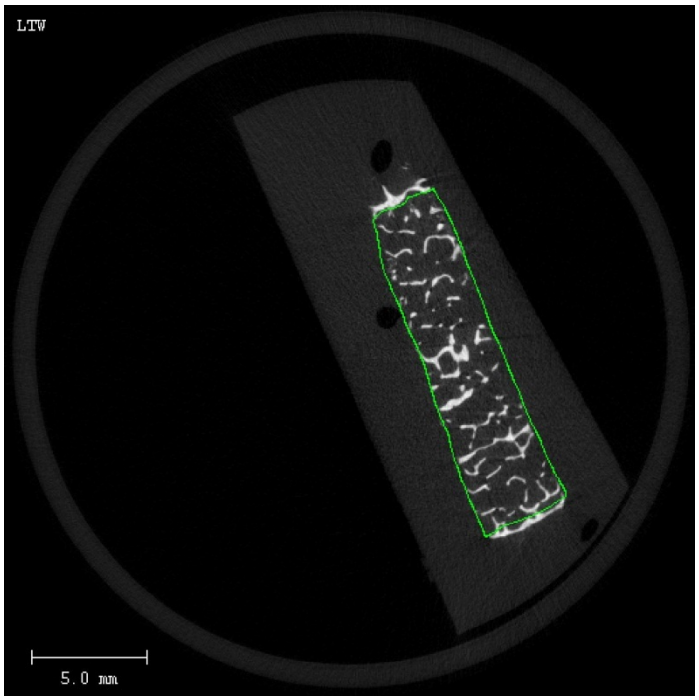

With the ROI set, a threshold must be dictated between what is, and what is not, bone tissue. For this study, a constant value of 184 mg HA/cm^3 was selected as the threshold. The value was based the recommendation of University of Kentucky graduate students experienced with scanning bone tissue. It is worth future study to determine what threshold criteria yields the highest fidelity geometry. For example, tailoring the threshold value based on the absorptivity histogram may lead to improved results. That being said, the method utilized in this study produced satisfactory results as evidenced by Figure 3-11. The radiodensity composition of the entire cross section is shown in Figure 3-12, with the structural bone tissue in white and all other material in black.

Figure 3-11: Greyscale (Left) and Thresholded (Right) Slices

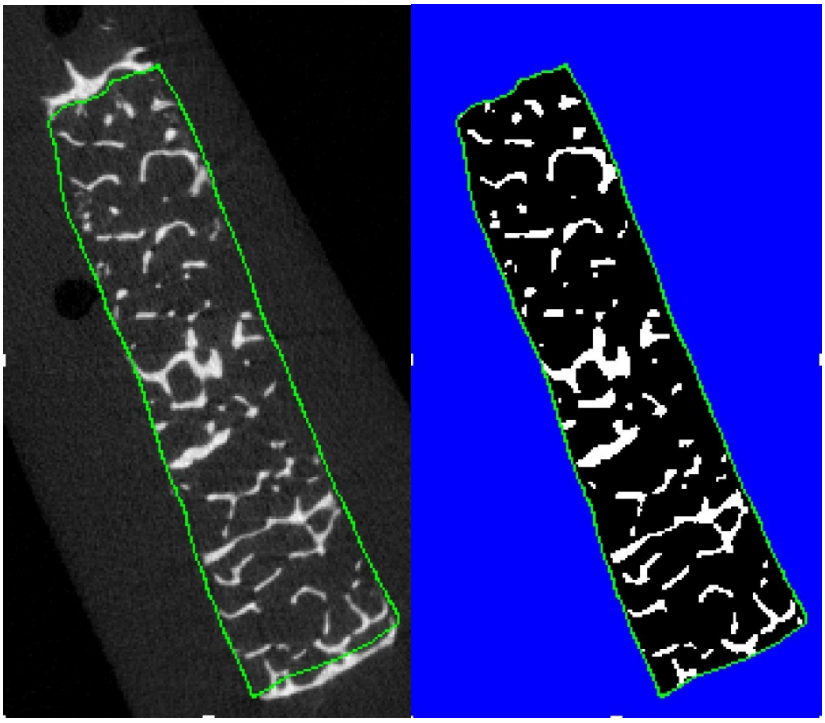

Figure 3-12: Histogram of X-ray Density in Slice 48

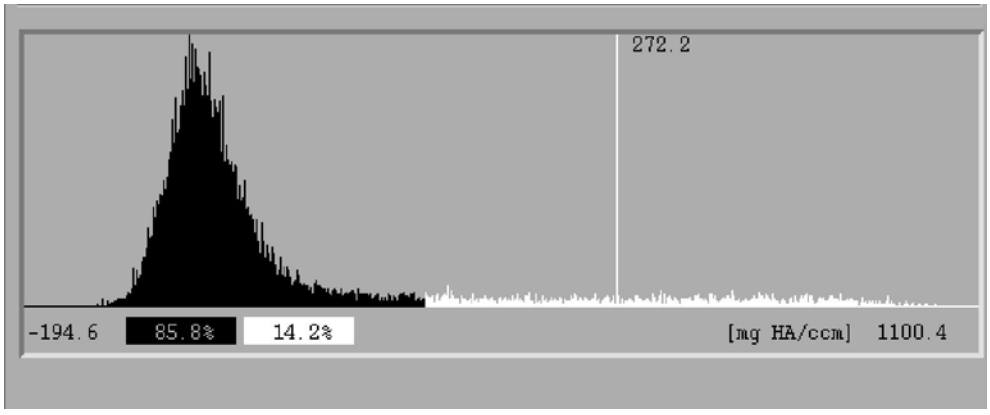

Following the designation of the ROI and threshold value, an entire suite of analyses may be executed. Histomorphometric analyses can be performed in 2D and 3D, DICOM files can be created, and the geometry can be exported as an STL file. Most of the analyses are computationally intensive; consequently, the proprietary SCANCO software does not run on a typical desktop computer. Rather, it utilizes an HP integrity server running the OpenVMS operating system. To create the STL file, the "3D segmentation of VOI" procedure was run from

the evaluation window. The segmentation evaluation generates a file with a *seg_aim* extension, used as the input for the STL generation. The STL file is created using SCANCO's Image Process Language (IPL). Figure 3-13 shows a sample of the command window used to interface with IPL.

Figure 3-13: SCANCO IPL User Interface

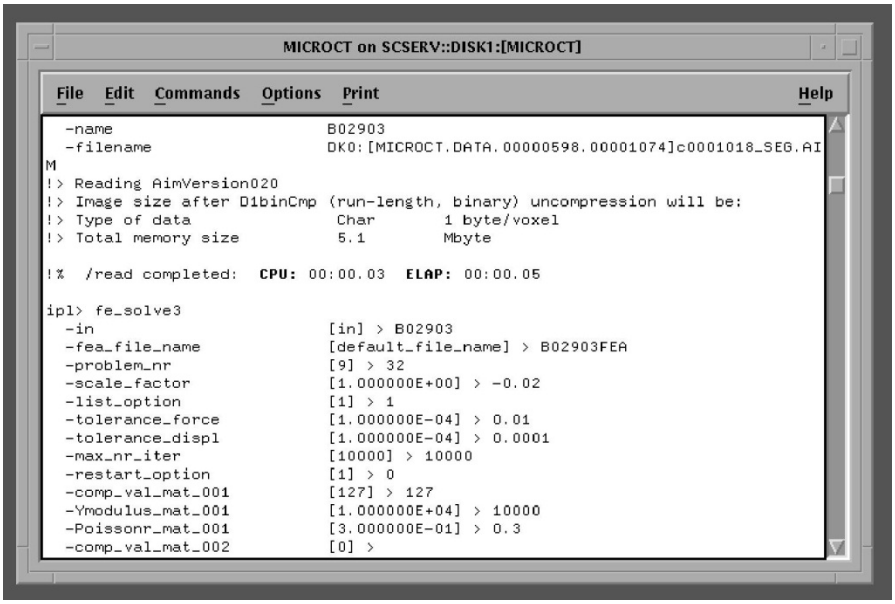

The STL file format has its roots in rapid prototyping, specifically additive manufacturing via stereolithography. The file itself encodes the geometric information by defining a large number of triangles. Each triangle is assigned an outward normal vector, and the points forming the triangle are defined by three Cartesian coordinates. In light of that, it is easy to see why STL is an acronym for Standard Tessellation Language [57]. The individual triangles do not have to possess any structure—such as connectivity or watertightness—they are completely raw. While that makes STL files very flexible, it is not helpful when conducting a finite element analysis. The surface geometry can suffer from holes, duplicate vertices, duplicate faces, zero area faces, and a litany of other problems. These issues must be resolved prior to any attempt to create a mesh.

3.4 Mesh Geometry Refinement

MeshLab is an open source program widely used to process unstructured triangular meshes, which was produced with the support of the 3D-CoForm project. It accepts the majority of common file formats, including STL. The software was created specifically with large files from 3-

D scanning in mind [58]. Due to that focus, MeshLab includes numerous automatic cleaning and repairing tools.

Importing the biopsy STL file into MeshLab v1.3.1 is as simple as selecting '*File>Import Mesh*' from the menu bar. MeshLab automatically unifies duplicate vertices and scales the geometry to fit within the viewing area. Typically, there are many free-floating pieces in the freshly-imported STL mesh. The finite element analysis requires one single body (with appropriate boundary conditions) in order to avoid rigid body motion. To eliminate the extraneous pieces, the command '*Filters>cleaning and repairing>remove isolated pieces (wrt diameter)*' was issued. For all of the biopsies in this study, a diameter of 4 mm was used. The biopsy length always exceeded that value, and any unwanted portions of the geometry larger than 4 mm were easily removed by manual selection. Figure 3-14 shows biopsy B01 prior to applying the filter, with a few of the free-floating pieces circled in red. Notice that one piece is quite small; removing all the fragments this size manually would be prohibitively difficult. After applying the filter, as shown in Figure 3-15, the unwanted volumes are no longer present.

Figure 3-14: STL Geometry Prior to Size Filter

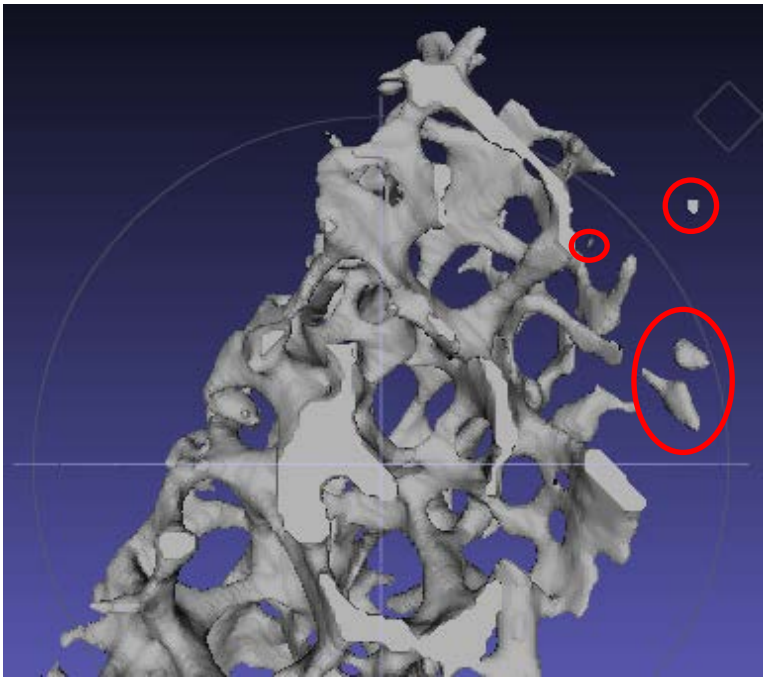

Figure 3-15: STL Geometry after Size Filter

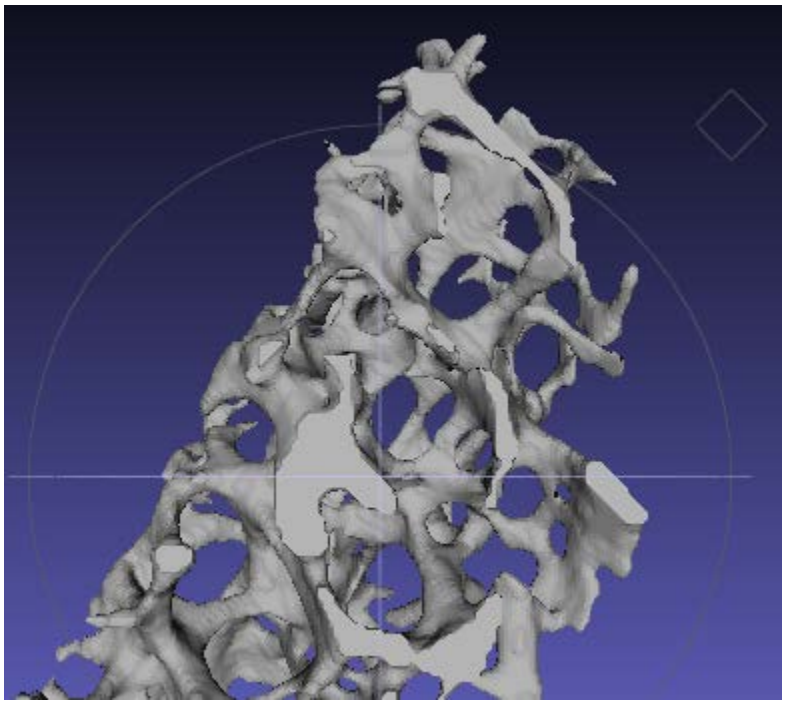

After removing separate bodies, the biopsies must be aligned for the simulated compression test in ANSYS. This alignment could have been performed by placing the biopsies in the SCANCO sample holder at a consistent angle. However, that would only partially solve the problem. Some biopsies were embedded into the acrylic at an angle to the bottom surface; i.e. they did not lie flat on the bottom of the block. Without a digital realignment, either the block would have to be machined, or the biopsy would have to be re-embedded. As for digital alignment, there were multiple avenues considered. The first attempt involved creating a new coordinate system in ANSYS, which would have had to have been done for each biopsy individually. So as to generate consistent ANSYS input, the alignment was done within MeshLab. Rather than manually altering the angle and using human judgment to decide when the biopsy was satisfactorily aligned, each biopsy was aligned with its principal axis. The command to do so is '*Filters>Normals, Curvatures and Orientation>Transform: Align to Principal Axis*'.

Figure 3-16: B019-09 Biopsy Alignment

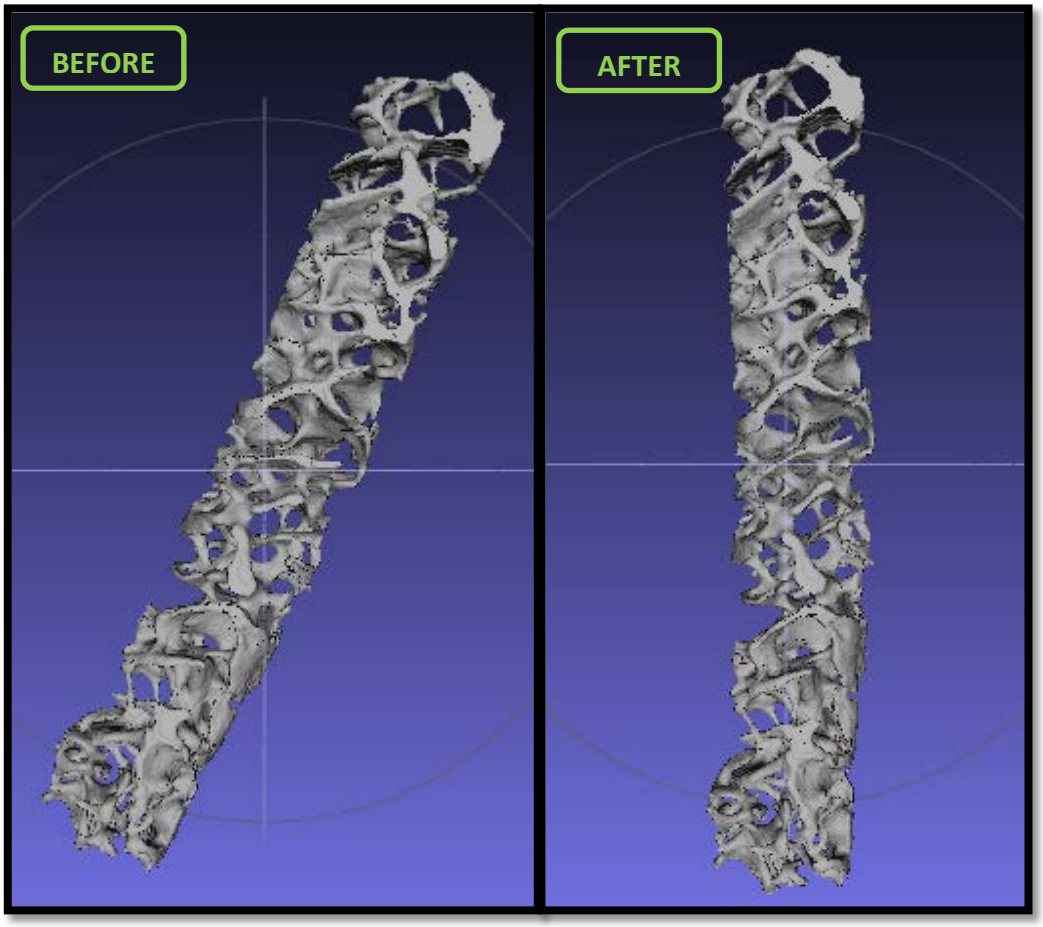

Occasionally the transformation would align the biopsy with the horizontal, rather than the vertical axis. In those cases, a 90 degree transformation was applied with '*Filters>Normals, Curvatures and Orientation>Transform: Rotate*'. The method of aligning to the principal axis worked best on biopsies with large aspect ratios. At small aspect ratios, the principal axis is dictated by the microarchitecture of the cancellous bone, and not by the axis of the core drill used to harvest the biopsy. Furthermore, a large amount of unevenly distributed cortical bone can visibly skew the alignment. In those cases, the cortical bone was removed using Netfabb Studio Basic, and then realigned with MeshLab.

Netfabb is another common tool for editing STL files, but unlike MeshLab it is not open source. The full version of the software, Netfabb Studio Professional is only freely available as a 30-day trial. However, the basic version of the software is freely distributed without a time restriction.

Serendipitously, both versions allow an STL file to be cut. Figure 3-17 shows a biopsy with its cortical bone still intact, and Figure 3-18 displays the biopsy after being cut with Netfabb v4.9.2.

Figure 3-17: Biopsy B07 Prior to Netfabb Cut

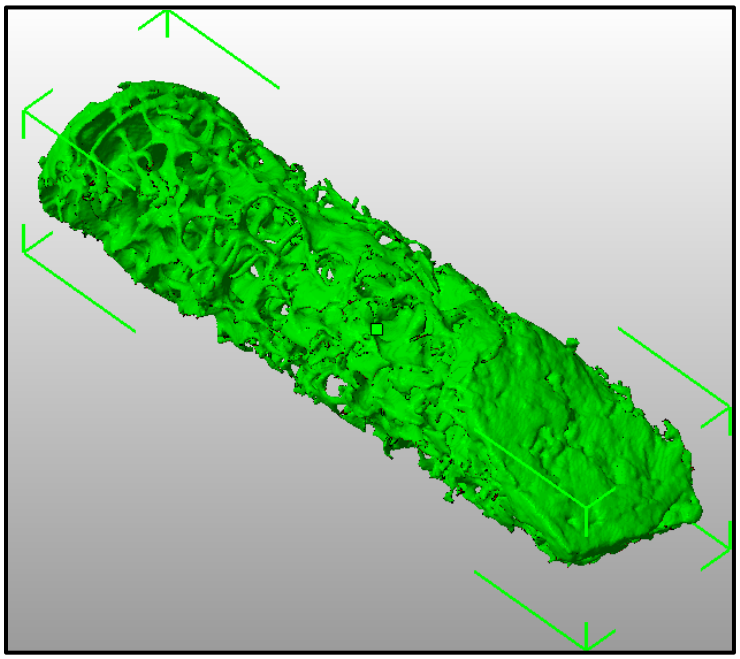

Figure 3-18: Biopsy B07 after Netfabb Cut

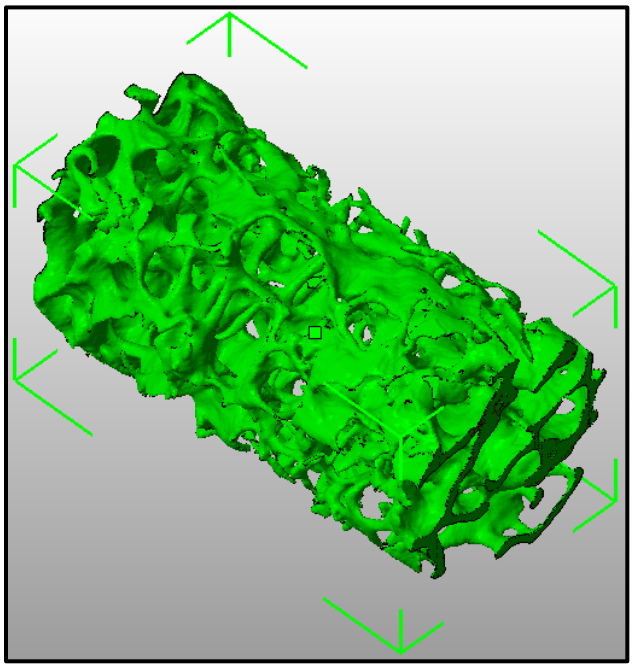

Biopsy B07 has two distinct regions of cortical bone, but even so, it was difficult to define exactly where cortical bone ended and cancellous bone began. Throughout this project, there was no consistent method to determine the border between the two types of bone; it had to be reevaluated on each biopsy. Some biopsies did not display any clear distinction between cortical and cancellous bone. Those biopsies were still cut at both ends for the following reasons: 1) A flat surface is convenient for the application of boundary conditions in the FE analysis, 2) The ends frequently tapered off or kinked, and 3) It allowed for a more consistent treatment of all the biopsies. After making the cuts, a piece of previously-connected bone would occasionally become separated from the main body. In this event, the STL was transferred back to MeshLab for clean-up. (Note that MeshLab processing must precede the cutting because Netfabb only cuts along the three orthogonal coordinate planes.)

Netfabb was also useful in repairing holes in the STL geometry. The problem with holes only manifests itself when attempting to create a solid mesh from the STL shell, so only those biopsies which could not initially be meshed were repaired in Netfabb. No modification from the default repair was necessary. Upon saving the repaired file, it was sometimes necessary to split manifold edges. A repair tolerance of 2 microns was accepted because, at 1/15th the scan resolution, it was unlikely to appreciably alter the geometry.

Figure 3-19: Netfabb Default Repair

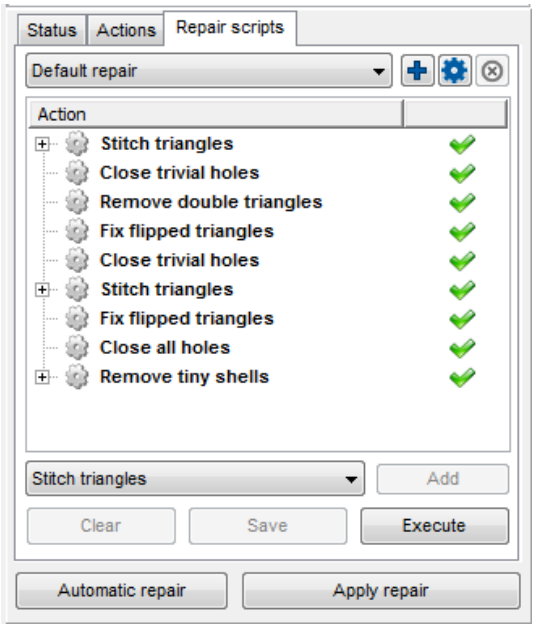

Figure 3-20: Two Micron Repair Tolerance

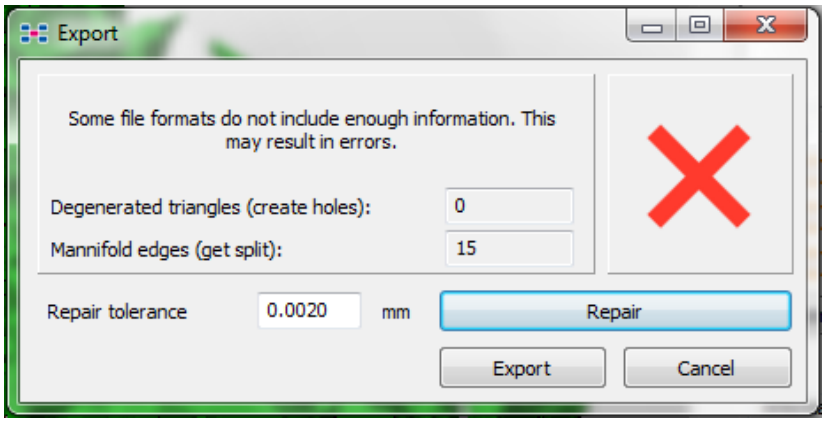

3.5 Mesh Generation

The STL mesh is just a shell representing the exterior surface of the bone. In order to perform a structural analysis, the mesh must represent the entire bone volume. Many commercial software packages are available which can mesh volumes enclosed by STL files, such as Rhinoceros, Mimics, ANSYS ICEM, Tgrid, and Hypermesh. ANSYS ICEM v14.0 was the tool of choice during this research for its intuitive user interface and widespread availability on site at the University of Kentucky.

After having filtered, aligned, and cropped the STL file, it was imported into ICEM with the command '*File>Import Geometry>STL*'. Typically, the geometry was not displayed on screen because of the large number of facets. (If desired, the imported surface can be forced to appear from the menu tree.) Next, the meshing parameters were defined. The final parameters chosen were the result of extensive thought and study, the specifics of which can be found in the **Mesh Convergence Study** section of this document.

The parameters defined for the volume mesh are divided into three menus: the global mesh parameters, the volume mesh parameters, and the mesh computation parameters. The global mesh parameters used in this study are shown in Figure 3-21.

Figure 3-21: Global Mesh Settings

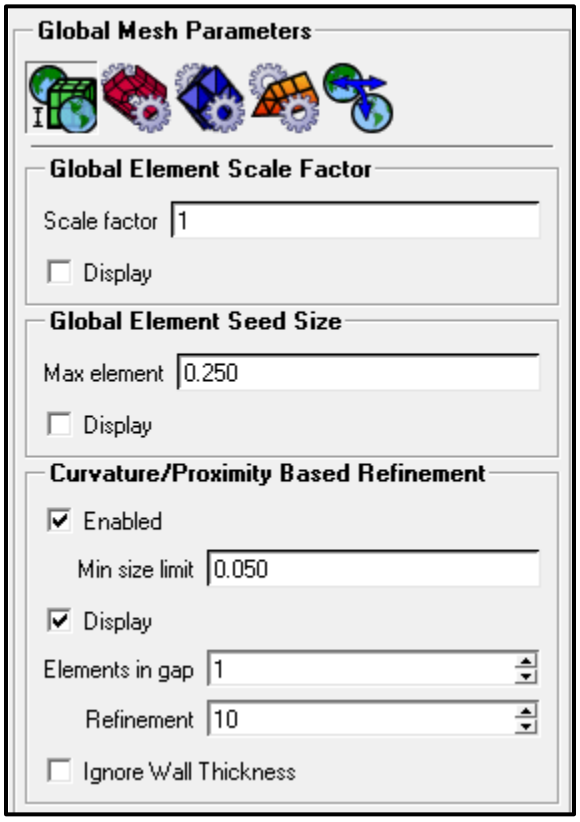

The global scale factor was left at the default setting of 1 because the STL output from the microCT is automatically provided in the actual-size of the specimen. The maximum element size was set to 250 microns. Most elements in the final mesh were below the maximum element size because proximity based refinement was enabled. The benefit of using this method is that it reduces the total number of elements in the model. If the max element size were selected to give a good representation of the geometry, it would result a mesh with too many elements. By using larger elements where there were thick regions of material, and smaller elements in the thin trabeculae, the total element count was reduced while conserving model fidelity. In addition to the global settings, there were also specific settings for the volume mesh (Figure 3-22).

Figure 3-22: Volume Mesh Settings

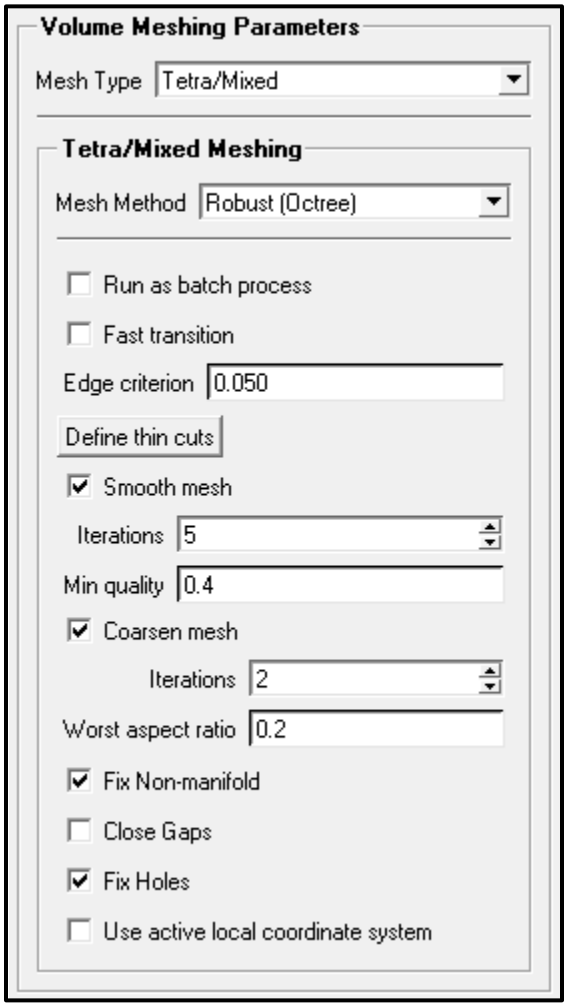

The mesh type can be tetra/mixed, hexa-dominant, or Cartesian. Within the category of tetra meshing, the methods available in ICEM are Octree, Delaunay, and advancing front. The hexa-dominant method produces a layer of hexa elements at the surface of the volume, and fills the core with tetrahedral elements. The Cartesian method can be implemented with a body-fitted approach, with a global method, or with a hexa-core. The Octree method was selected because it permits more flexibility for local refinement within ICEM than any of the other options. The Octree method works by first encompassing the entire geometry with relatively large tetrahedral elements. Then, the elements are subdivided into smaller and smaller volumes until all of the constraints are satisfied. For example, it may stop when the minimum element size is reached, or when the local refinement parameters are met. After subdivision, ICEM makes the

mesh conformal, and moves the nodes which are near the exterior of the volume to the surface. Lastly, it removes all of the elements not enclosed by the volume, and smooths the mesh.

Picking the edge criterion is a tradeoff between the geometric accuracy of the mesh and the number of elements. As shown in Figure 3-22, 50 microns was selected. (The fact that the minimum element size is also 50 microns is merely coincidence.) For more details on how this value was selected, refer to the **Mesh Convergence Study**. The "Smooth Mesh" option is on by default, and was not altered. The "Coarsen mesh" option is not on by default, but it was activated in an effort to further reduce element number. Coarsening allows the mesh to be created with smaller elements which capture the geometry well. Then, unnecessary refinement is removed to lower the element count.

Finally, after defining all of the mesh settings, creating the mesh is as simple as pressing the "Compute Mesh" button. Though, the mesh does require some additional scrutiny before it can be deemed acceptable. Most importantly, excess materials need to be deleted prior to export. A created material (Figure 3-23) represents a free-floating volume that was not removed from the STL file, or a region of bone tissue that could not be connected by the elements. For example, if two trabeculae were joined by a connection less than 50 microns thick, the meshing algorithm would be forced to create two separate parts. Losing that connection may seem like a serious loss of fidelity, but it is not for two reasons. First, the links never occurred between two large sections of the biopsy. In all cases, the lost material was in an exterior region which would not have carried much (if any) load in the compression test. Secondly, even if a more crucial connection were lost, it could not possibly have supported much load in comparison to the thicker trabeculae. Figure 3-24 shows what the excess materials look like when the main body of the biopsy is hidden.

Figure 3-23: ANSYS ICEM Materials

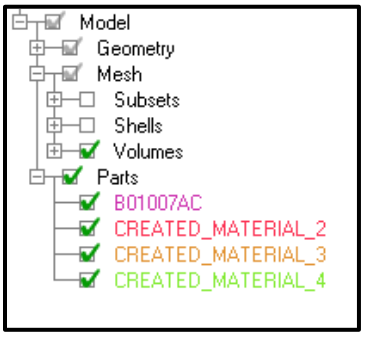

Figure 3-24: B02 Unattached Volumes in ICEM

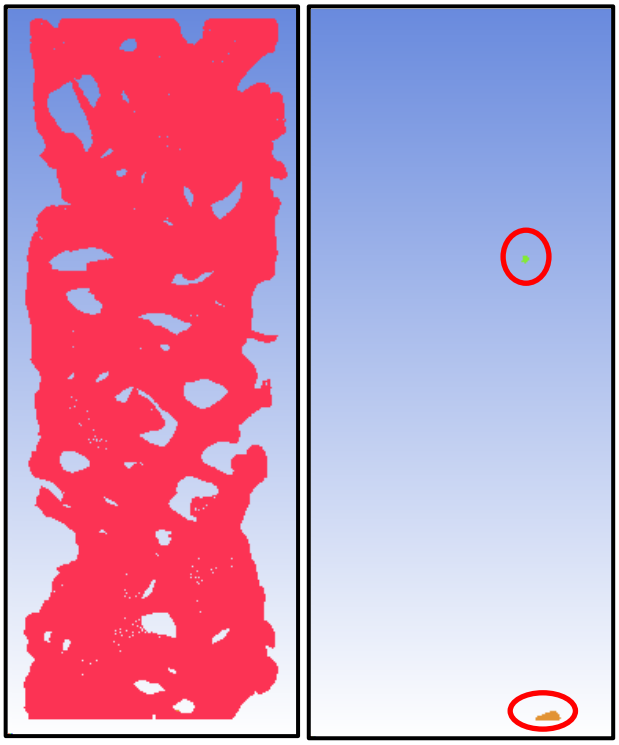

ANSYS ICEM can perform a surfeit of mesh quality checks, but no check was performed on each individual biopsy. A cursory visual inspection was completed, and if no problems were encountered during the analysis, it was assumed that the mesh quality was acceptable. For reference, Figure 3-25 shows a mesh quality check from biopsy B02.

Figure 3-25: Biopsy B02 Mesh Quality

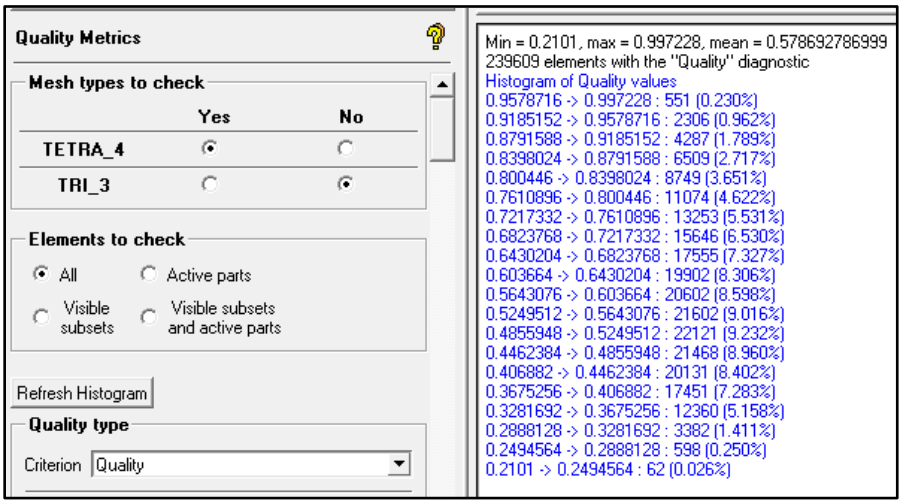

Having verified its quality, the mesh must be exported to ANSYS APDL in order to run the finite element analysis. The command for doing so is '*File>Export Mesh>To Ansys*', which brings up the Solver window as shown in Figure 3-26. Notice that no shell or bar elements are selected. If they are included, as they are by default, the code in **Appendix C** will not run properly.

Figure 3-26: ICEM Export Settings

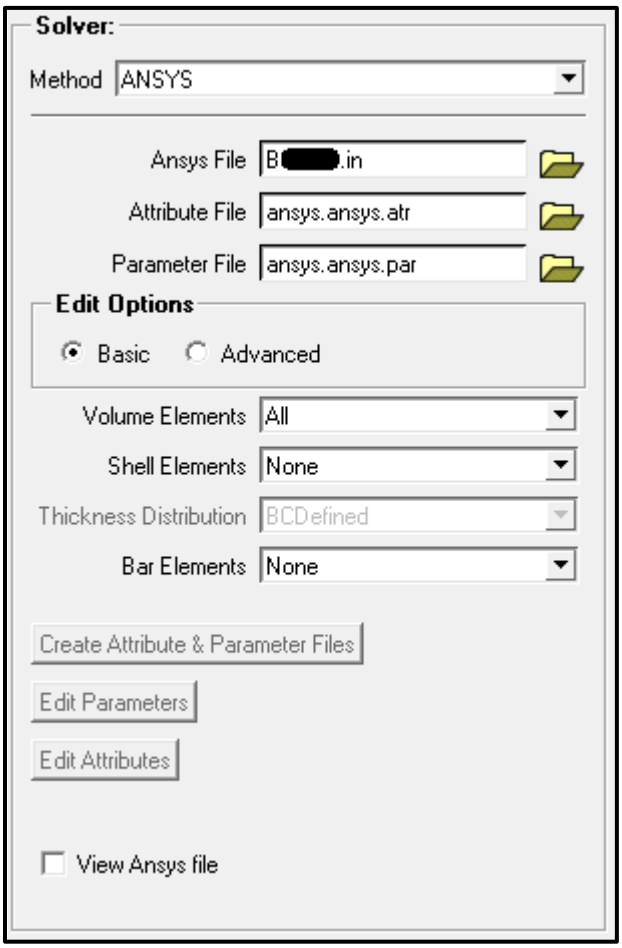

3.6 ANSYS Compression Test

3.6.1 Software Selection

Before describing the methodology used to perform analyses in ANSYS, it is worth discussing why the SCANCO FEA package was not selected. The SCANCO software does possess a number of advantages: seamless integration with the scanned geometry, fast run times, use in numerous publications [59,60,61], and one-time pricing. But, it is not nearly as convenient or versatile as ANSYS. The SCANCO software is an addition to the company's proprietary image

processing language. A user performs the analysis by entering information into a command prompt. (FEA commands are on-screen in Figure 3-13.) For anyone accustomed to the Windows environment, the software is unpleasant to use. More importantly, it has severe technical limitations. The software can only analyze linear-elastic brick elements. ANSYS, to the contrary, is a worldwide leader in finite element simulation. ANSYS can handle, among other problems, material and geometric nonlinearities, stochastic analyses, multi-physics simulation, optimization, contact, composite materials, buckling, vibration, dynamic forces, and element death. Secondarily, it has a vastly superior user interface. The model manipulation and editing tools within ANSYS are easier to use, faster, and more capable than those in the SCANCO software. As a final point, the ANSYS software has a wider user base, which makes learning the procedures and troubleshooting problems relatively easy.

3.6.2 Analysis Overview and Assumptions

To evaluate the mechanical properties of the cancellous bone biopsies, they were put through a simulated 1% strain compression test. This value is consistent with other compression tests found in the literature [62], although there is some variation. Karim and Vashishth used 0.6% and 1.1% apparent-level strain for pre-yield and post-yield tests, respectively [63]. The values were chosen based on a yield point of ~0.8% for cancellous bone [64]. Since a linear elastic model was used in this research, the exact level of applied strain is not crucial. The results can be scaled to any reasonable level of strain [65].

The linear elastic model has been used in engineering analysis for decades [66], and pre-dates the finite element method [67]. The widely-used Euler-Bernoulli beam theory, which is responsible for many classic engineering equations, is based on a simplification of linear elasticity. In order to apply the model to bone tissue, it is crucial that it satisfies the assumptions built into the model. Those assumptions are that: 1) the material is linear, 2) no yielding occurs, and 3) strains remain small.

To maintain material linearity the strain must be directly proportional to the applied stress. Most metallic materials are linear up to the yield point, after which they enter a region of nonlinear plastic behavior. (Technically, there is a small nonlinear elastic region between the proportional limit and the yield point.) Certain materials, such as elastomers, concrete, and cast iron exhibit no linear behavior, even in the elastic region. Multiple studies support the use a linear material model in human bone [68]. However, it should be kept in mind that fracture is a

post-yield event. The linear model may be valid for calculating apparent-level young's modulus, but the determination of fracture is complicated by nonlinear phenomenon. For instance, bovine cortical bone exhibits non-linear material properties under dynamic loading [69].

The requirement to avoid yielding is closely related to the linearity requirement, since the stress-strain curve is no longer a straight line after the yield point. But unlike the linear assumption, which is primarily a matter of material property, satisfying the pre-yield assumption is a function of the geometry and the applied load. Due do that fact, the assumption is violated for small portions of any given biopsy. Thin trabeculae, in particular, are prone to exceeding the yield stress. In a non-linear analysis is would be possible to remove the offending elements and iterate until there were no overly-stressed regions. Since this is a linear analysis, the highly stressed elements were dealt with by using an accumulated-damage failure criterion.

The third and final requirement is that strains remain small. This is necessary because the small angle assumption was used in the derivation of the governing equations. Most materials have small strain at yield, and bone is no exception. Of all the linear elastic assumptions, this one is the most justifiable in regards to the present application.

Isotropic material properties were used in the analysis, despite the fact that bone is known to be anisotropic [70,71,72]. Pistoia et al., using isotropic properties, achieved an R^2=0.66 between FEA failure load and experimentally obtained failure load [65]. Finite element analysis has been performed on bone using anisotropic properties [73], but the application of directionally dependent properties would have been difficult given the geometric complexity of cancellous bone.

3.6.3 Detailed Procedure

Now that the background assumptions are clear, the minutiae of the procedure itself will be specified. Any finite element analysis can be divided into three fundamental steps: preprocessing, processing, and post-processing. Preprocessing encompasses all the tasks necessary to set up the matrix equations. Processing is the act of solving the set of algebraic equations. Post-processing involves extracting desired information from the solution. In this application, post-processing entails calculating stress and strain from the displacement field.

3.6.3.1 Preprocessing

In an engineering analysis, the classic preprocessing steps are: 1) Geometry definition, 2) Mesh generation, 3) Application of material properties, and 4) Setting loads and boundary conditions. The first two steps are complete by the time ANSYS APDL is put into use. The geometry is taken from the STL file obtained using microCT. The meshing is done in ANSYS ICEM, and can be imported directly into APDL using the command '*File>Read Input from*'. The default tetrahedral element type in ICEM is SOLID185, and that was not modified for this analysis. SOLID 185 is an 8-node element with 3 DOFS at each node. The tetrahedral version is a degenerate element with 4 shared nodes at one vertex, and two shared nodes at a second vertex [74]. Generally, it is not recommended to have more than 10% tetrahedral elements in a model, but this rule was violated because tetrahedral elements excel at capturing the geometry of irregular surfaces. Any shortfall of the element was remedied by using a finer mesh. The convergence study ensured that enough elements were used to obtain valid results. Other tetrahedral elements were considered, such as the 10-node SOLID187, but were not selected due to the additional degrees of freedom required.

After importing the mesh, material properties were defined. The Young's modulus of the bone tissue was set to 10 GPa, which is within the range of published values for cancellous bone [75]. The poison's ratio was set to 0.3. Because a simple isotropic material model was used, no additional parameters had to be defined. (Recall that of the shear modulus, Young's modulus, and Poisson's ratio, only two are independent.) The left image in Figure 3-27 is biopsy B02 directly after importing the '.in' file created by ICEM.

Figure 3-27: Biopsy B02 Elements in ANSYS

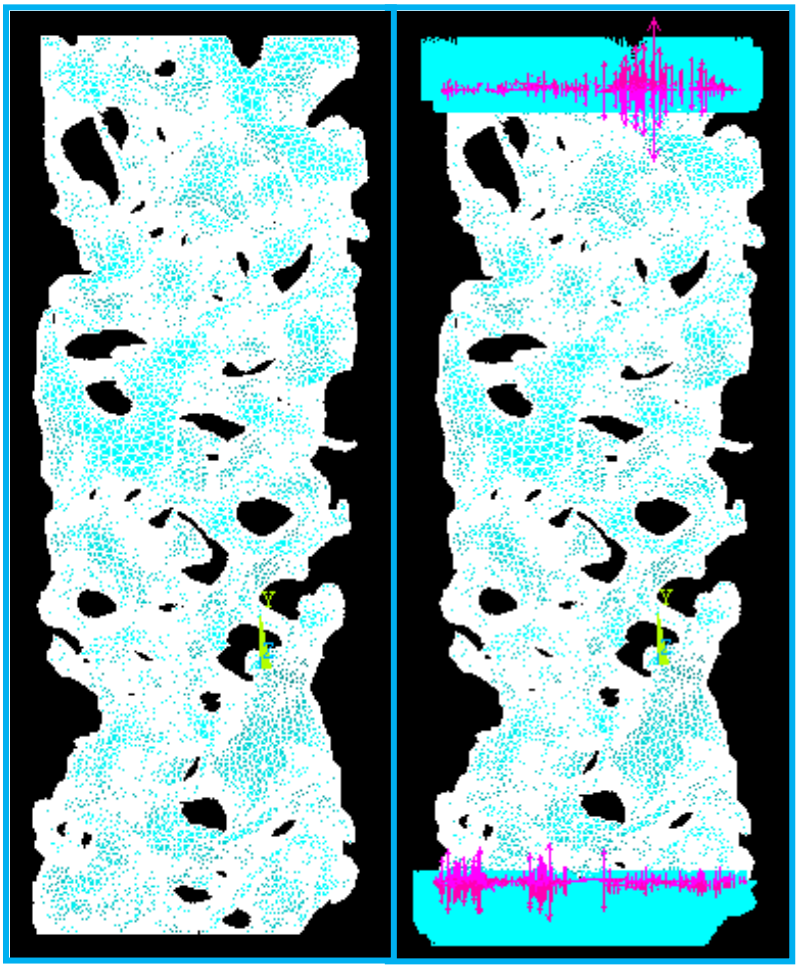

The boundary conditions were selected to simulate a 1% strain compression test. In order to prevent rigid body motion, the nodes in the bottom 5% of the biopsy were fixed to zero displacement in all three directions. To simulate the compression, the nodes in the top 5% of the biopsy were displaced until a 1% strain was achieved. The right image of Figure 3-27 shows the applied boundary conditions, as well as the resulting reaction force. The 1% value was calculated from the portion of the biopsy without any applied boundary conditions. For example, if a hypothetical biopsy was 10 mm long, the nodes in the top 0.5 mm would have been given a downward displacement of 0.09 mm. Keep in mind, though, that the exact value of the displacement is not critical. Because this is a linear analysis, the solution can be scaled to any value of applied compression. If a 2% displacement were applied, then the stress at any point in the biopsy would be twice the value obtained from a 1% displacement analysis.

Admittedly, the applied boundary conditions are not particularly elegant. The resulting stresses and strains in the top and bottom 5% of the biopsy are zero, so no useful information is extracted from those regions. The methodology was implemented to accommodate biopsies with rough ends, and was never altered because—while crude—it is a valid compression test.

3.6.3.2 Processing

Selecting a solver is an often-overlooked part of the FEA process. The majority of the time, the ANSYS default sparse solver works well. When that is the case, solving requires no more effort than clicking a button. However, as the total degrees of freedom increase, some consideration of the solver is justified. Above 500,000 DOF, the Preconditioned Conjugate Gradient (PCG) solver becomes the more attractive option [76]. The PCG solver is iterative, and less robust than the sparse solver. Nevertheless, it worked well in this application.

3.6.3.3 Post-processing

The direct output of any finite element model is simply a value for each degree of freedom at each node. For SOLID185, the only degrees of freedom are displacements in the coordinate directions. Using those nodal displacements combined with the interpolation functions, the result is a piecewise function describing the displacement at every point in the domain. Using equations of linear elasticity on the function, stress and strain can be determined at any point. Specifically, the information extracted from each model included the reaction force, the energy equivalent strain, and the maximum von Mises stress.

Figure 3-28 shows the displacement of B02 in two ways. The left image is an exaggerated display of the displacement, with the original shape outlined in white. The image to the right is a counter plot based on the vector sum of displacement. Unsurprisingly, the displacement is greatest at the top, and least at the bottom. More interestingly, the displacement shows a clear relationship with the plates in the biopsy. The von Misses stress is plotted in Figure 3-29, and it shows that the majority of the biopsy is lightly stressed. A close-up on the right revels that small portions of the trabeculae are responsible for the high stresses. So, much of the structure is under-utilized, at least for this one loading condition. The finite element method can produce some exquisite-looking figures, but caution should be used in interpreting them. Just because the results look good does not mean that they are accurate or pertinent. The color contour plot, in particular, is subject to manipulation by altering the scale. All of the plots presented here use

the ANSYS default scale, but readers should still be hesitant to make any conclusions based solely on the figures.

Figure 3-28: Displacement

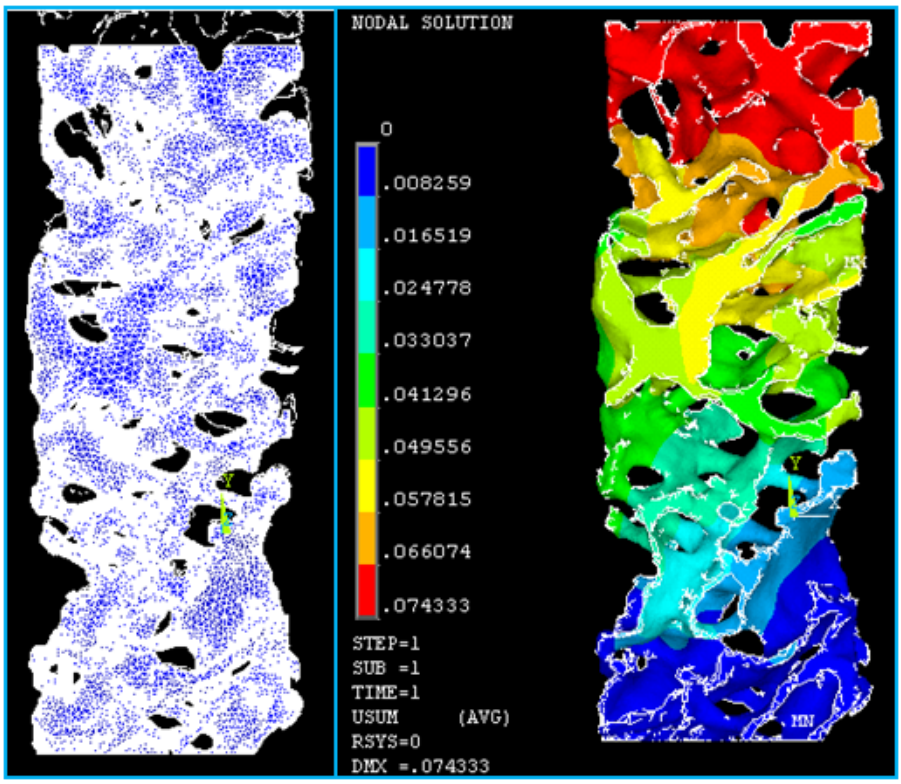

Figure 3-29: Von Mises Stress

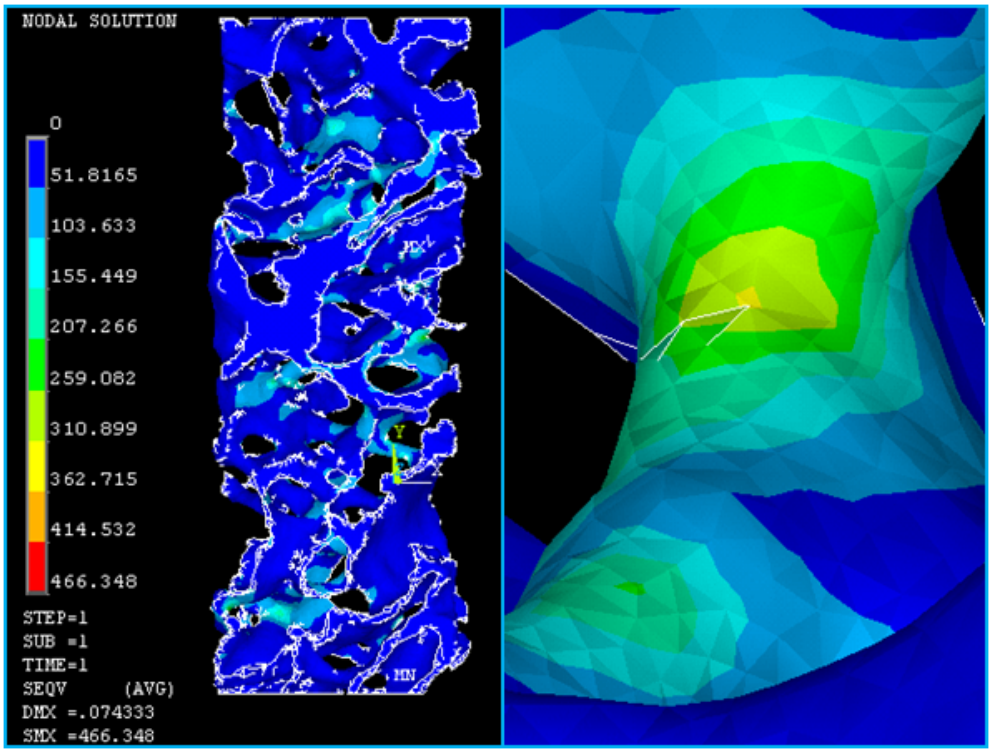

Rather than performing all of the pre/post-processing steps manually within the GUI, APDL code was written to automatically perform the analysis on each biopsy. The full APDL code is in **Appendix C**. The code was derived from prior work by Vijayalakshmi Krishnaswamy and Dr. Rouch. Three major upgrades were made to the original code. First, there are no spring elements in the new code. The old version required all of the elements to be connected by weak springs in order to prevent rigid body motion of rouge pieces unattached to the rest of model. The extra elements were a detriment to solve times and memory requirements. Secondly, the updated code can process a list of '.in' files without operator intervention. Thirdly, a cumulative strain-based failure criterion was added to the code.

The code outputs the total y-direction reaction force, the maximum von Mises stress, the bone volume, the number of elements, the biopsy length, and the estimated failure load. The bone volume and the biopsy length could have been determined in Netfabb from the STL geometry, but it was more convenient to obtain the values from the FEM. The estimated failure load was based on the accumulated-strain criteria developed by Pistoia et al. [54]. In his experiments, the

force required for 2% of the bone volume to exceed an energy equivalent strain of 0.007 showed the best correlation (R^2=0.75) with experimentally measured fracture forces.

To determine the failure load in this experiment, a table was created with element volumes and their corresponding strain. The table was then sorted by strain. Starting with the highest strain, the element volumes were added together one-by-one until the volume equaled 2% of the stressed volume. (Due to the boundary conditions, 1.8% of the total volume was used in lieu of 2% of the stressed volume.) The single element which caused the summed volume to exceed the 2% mark was selected, and its strain value was scaled to 0.007. Reaction force was scaled by the same factor to arrive at the failure load. For example, if the 2% element had a strain of 0.0035, the failure load was twice the reaction force.

3.7 Area Determination

To ascertain the total biopsy volume and the unit failure load, the cross sectional area of the biopsies had to be measured. If the same core drill had been used to extract the all of the biopsies, it would be reasonable to take the inner diameter of the drill as the cross sectional area. As can be seen in **Appendix E**, the biopsies have a wide range of diameters. There is no way to verify a drill size for each biopsy with certainty. Further complicating matters, several biopsies were sliced approximately in half for previous studies requiring histological analysis.

To determine the unique area of an individual biopsy, the nodal coordinates were exported to a text file from ANSYS APDL. After plotting the points in 2 dimensions on the XZ plane, an intuitively clear picture of the biopsy cross section emerges.

If only a handful of biopsies were being measured, it would be straightforward to manually connect the nodes around the perimeter and calculate an area. In the interest of saving time, and eliminating any potential human bias, an automated method was employed. As it turns out, the problem of encompassing a set of points with a polygon has already been studied extensively by mathematicians [77]. Or, more accurately, the smallest possible convex set containing given points has been studied. A convex set is any set for which a line joining two points in the set lies entirely within the set (see Figure 3-30).

Figure 3-30: Convex Set

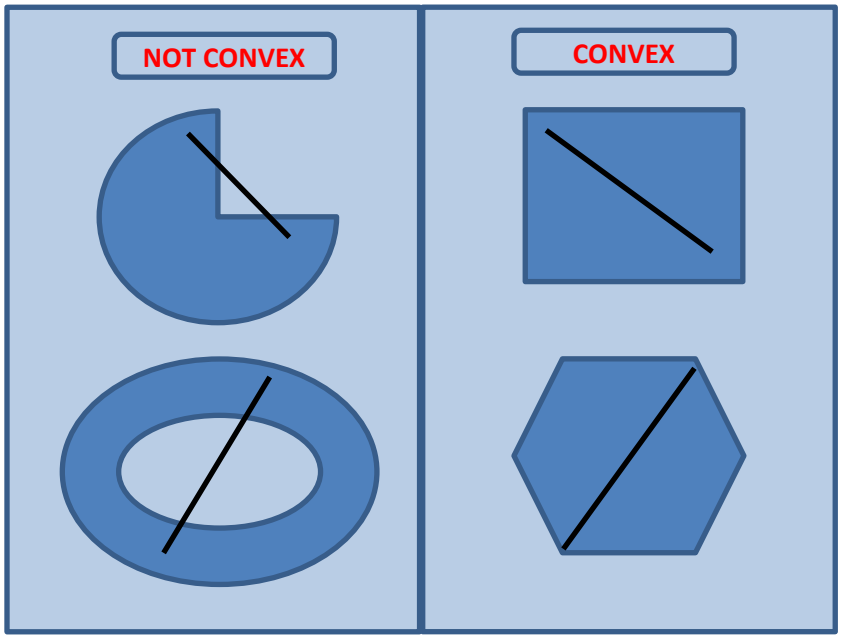

The convex hull method will overestimate the existing cross section of the biopsies whenever there is reentrant geometry present. However, the two nominal shapes which the biopsies should conform to, cylinders and half-cylinders, both have convex cross sections. In fact, since the biopsies are extracted with a cylindrical drill, any reentrant portions of a biopsy should signify regions devoid of bone in the patient. As such, the entire cross section, not just the portion containing bone, should be used when calculating total bone volume.

Implementing the convex hull algorithm was done within MATLAB R2012a. What minimal code was necessary was developed in cooperation with Jonathan Ward, and can be found in **Appendix D**. As with the ANSYS APDL code, the biopsies were run in a batch mode. The nodal points and convex hull outline are shown in Figure 3-31.

Figure 3-31: Biopsy B04 Outline

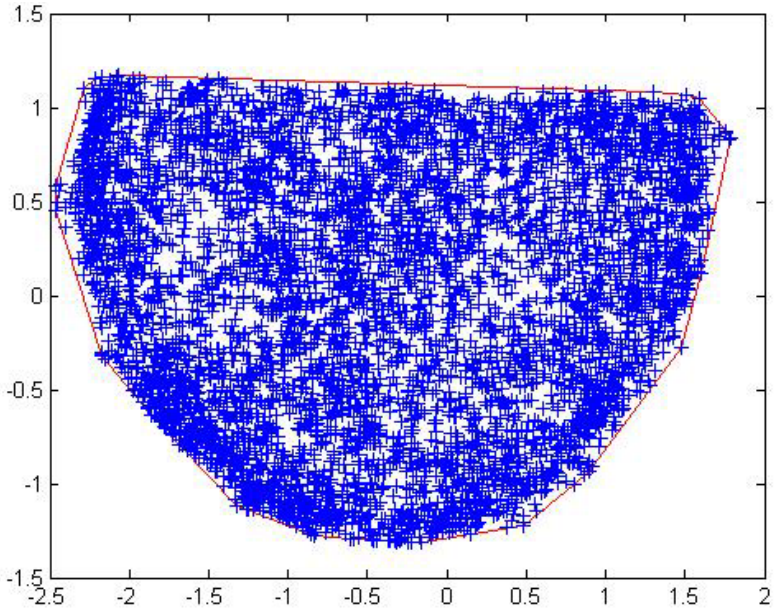

Admittedly, the method described above does not always produce a perfect cross section. Occasionally the cut plane in the biopsy is not well aligned with the axis of the original cylindrical biopsy, in which case the resulting shape is not prismatic. Any misalignment of the biopsy will skew the cross section, as will any misshapen portion jutting out from the main body. In these cases, the convex hull algorithm will slightly overestimate the cross sectional area. However, these are primarily issues of biopsy quality, and they do not reflect on the area measurement method. With diligent biopsy preparation, the potential for error is small.

3.8 Calculated Properties

No direct comparison can be made between biopsies after the finite element analysis because stiffness varies as a function of cross sectional area. Similarly, the reaction force must be converted into an equivalent stress before any comparison is meaningful. The equations in this section describe precisely how the values in the results section are calculated. The overall philosophy of the calculations is to treat the bone biopsy as a single homogeneous material. With that assumption, material properties for the total bone are derived.

The stiffness of bone is correlated to fracture [78], so it may show a correlation with long term bisphosphonate use.

$$E = \frac{\sigma}{\epsilon} = \frac{F_r/A}{0.01}\ [N/mm^2]$$
$$F_r = FEA\ reaction\ force$$
$$A = Area$$

The apparent modulus as calculated above makes no correction for the amount of cancellous bone tissue in the biopsy. Looking only at the Young's modulus there is no way to determine what portion is due to good microarchitecture, and what portion is due simply to a large amount of trabecular tissue. If two biopsies were to have the same modulus, yet one biopsy achieved the value at a lower BV/TV ratio, then it must have superior architecture.

$$E_{eff} = E * \frac{TV}{BV}\ [N/mm^2]$$
$$TV = total\ volume$$
$$BV = bone\ volume$$

While stiffness is of some value, it does not predict failure. Many failure criteria exist, even when considering only isotropic materials. When analyzing metallic structures, failure is commonly defined based on the von Mises stress. Since it condenses the full three dimensional stress state of the material into a single value, the von Mises stress is also an incredibly convenient criterion. Nonetheless, it still requires modification before biopsies can be compared. The von Mises stress resulting from the compression test is misleading because the reaction force required to achieve the 1% strain is not consistent. So, a stress amplification ratio (SAR) was calculated.

$$SAR = \frac{\sigma_{max}}{\sigma_r} = \frac{\sigma_{max}}{F_r/A}$$
$$\sigma_r = reaction\ stress$$
$$\sigma_{max} = maximum\ von\ Mises\ stress$$

The von Mises failure criterion assumes that the entire structure fails when any portion of the structure—however small—exceeds the material allowable stress. In order to allow for accumulated local damage prior to global failure, a strain-based method was utilized.

$$\sigma_{fg} = \frac{f_{fg}}{A}$$

The failure load originating from the finite element analysis was simply divided by the cross sectional area for fair comparison. The result, on the apparent level, is a failure stress.

4 Results

4.1 Coarse Mesh Output

All 30 biopsies were initially modeled with a relatively low number of elements. The meshes were created using the auto-sizing option in ANSYS ICEM, which selects a seed element size of 0.025 times the bounding box diagonal of the geometry. The edge criterion was modified to 0.01 mm. All other ICEM settings were left on their default values. This method created meshes ranging from 25,258 (B04) to 133,190 elements (B11). The large range in the number of elements is chiefly attributable to the variation in bone volume, which spanned from 1.7 mm^3 (B19) to 48.8 mm^3 (B24). The biopsies with the extreme volumes did not correspond to those with the extreme number of elements due to differences in microarchitecture.

The auto-sized mesh resulted in elements which were too large to represent the detailed geometry of the biopsies. The seed element size was for B02 was 0.2 mm. Since the trabeculae were typically around 0.150 mm, and sometimes as small as 0.050 mm, the seed element size was too large to capture the geometry accurately. For reference, the zoomed-in portion of the biopsy in Figure 4-1 is about 70 microns in diameter. Evidently, some elements are created below the seed size, but not enough to give good results.

Figure 4-1: Biopsy B02 Coarse Mesh

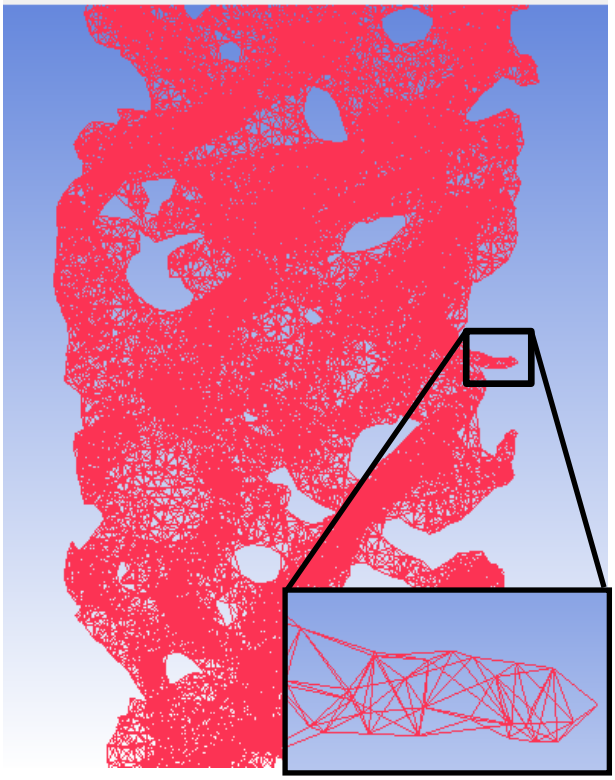

Despite the known fact that the coarse mesh did not represent the bone geometry well, it still presented a number of advantages. Principally, the ANSYS license available at the University of Kentucky prior to July 2012—the academic teaching license—is only valid for processing models under 250,000 elements. The lower density models served as an interim object of study until higher fidelity meshes could be analyzed. Secondarily, the smaller models had much faster solve times. The entire process of generating the matrix, solving, and calculating element results took less than a single minute per biopsy. Without the burden of lengthy run times, many iterations of the APDL code could be tested. After developing working code on the coarse meshes, applying it to the fine meshes was effortless. But, the coarse mesh was not just a tool to troubleshoot code and get around an element number limitation.

Studies done by a prior student, Vijayalakshmi Krishnaswamy, showed that significant results could be acquired with a coarse mesh. P-values less than 0.05 were obtained between groups (n=10) of low-turnover stage five CKD patients and normal-turnover patients without CKD. The result was expected based on how drastically different the two groups were.

Unfortunately, unlike in the CKD study, no statistically significant results were found between the three experimental groups in this research. For each of the calculated properties, a one-way ANOVA was used to gauge significance. For reference only, the ANOVA was followed up with an unpaired two-tailed Welch-corrected t-test on each set of experimental groups. (For more details on why this test was chosen, refer to the **Statistical Analysis**.)

Table 4-1: Coarse Mesh Results Summary

Mean ± SD	Control	Short Term	Long Term
E [MPa]	320±352	617±898	244±218
E_{eff} [MPa]	1890±1566	2076±1871	1437±691
SAR	503±371	634±1144	647±752
σ_{ult} [MPa]	1.84±1.54	3.11±3.76	1.63±1.07

Table 4-2: Coarse Mesh P-Values

	ANOVA	Control vs. Short	Control vs. Long	Short vs. Long
E [MPa]	0.3204	0.3519	0.5712	0.2315
E_{eff} [MPa]	0.6103	0.8123	0.4197	0.3332
SAR	0.9104	0.7381	0.5971	0.9765
σ_{ult} [MPa]	0.3479	0.3418	0.7296	0.2575

Since no significance was found, there was substantial motivation to increase the mesh density. Decreasing element size simultaneously improves the geometrical representation of the biopsies, and refines the solution of the governing differential equations. It was hoped that the increased precision of the finite element model would decrease the standard deviation of the groups, allowing for more statistical power.

4.2 Mesh Convergence Study

Since it was concluded that the coarse mesh could not accurately model the geometry of the biopsies, the mesh density was increased. Increasing the element number increases the

computational requirements, so the ICEM mesh settings were studied to find the optimal parameters.

4.2.1 Global Element Size

The first variable examined was the global maximum element size, which also serves as the seed element size. Values ranging from 65 µm to 250 µm were tested; the results are reported in Table 4-3. As only one biopsy (B09) was used to create all of the meshes, it was not necessary to account for the cross sectional area. The reaction force, Fy, was reduced by 4.75% going from a seed size of 75 µm to 65 µm. That level of change is undesirable, but the element number could not be increased further due to computational limitations. In an attempt to achieve tighter convergence at a lower element number, local refinement was enabled.

Table 4-3: Effect of Global Max Element Size

Size [µm]	F_y [N]	σ_{max} [MPa]	BV [mm^3]	Elem #
65	5.21	2691.3	8.08	718310
75	5.47	1619.7	8.04	521680
100	6.07	2107.1	7.96	277940
125	6.48	1502.0	7.87	171430
150	6.91	935.5	7.78	118450
250 (auto)	7.79	438.6	7.58	47872

4.2.2 Local Refinement: Minimum Element Size

Local refinement allows the element size to be smaller where the geometry dictates the need for it, and larger in less complex regions. When using this method, the global element size was left at 250 µm, which is the size chosen by ICEM if running with auto-sizing enabled. The refinement parameters: elements in gap, and curvature refinement, were held constant at 1 and 10, respectively, throughout the analysis. The only variable altered between each run was the minimum element size. As in the global element test, the smallest size attempted was 65 µm. In the transition from a 75 micron limit to a 65 micron limit, the reaction force fell by 3.56%, while the element number increased 25.9%. Compared to decreasing global max element size, local refinement achieves a tighter convergence at a lower element number. At the 65 µm level, the uniform-element mesh had 21.3% more elements than the locally-adjusted mesh. Despite

the clear improvement, other mesh settings were investigated to achieve a more efficient model.

Table 4-4: Reducing Minimum Element Size

Size [µm]	F_y [N]	σ_{max} [MPa]	BV [mm^3]	Elem #
65	5.48	2528.0	8.07	592240
75	5.61	2031.6	8.04	470290
100	6.05	1039.9	7.95	271260
125	6.49	991.4	7.87	170280
150	6.91	935.5	7.78	118450

4.2.3 Setting Edge Criterion to 200 Microns

The previous two studies used an edge criterion (EC) of 0.01 mm. The edge criterion defaults to a value of 0.2 mm, but it was changed at the onset of this research to 10 microns. The value was chosen with the SCANCO voxel size of 30 microns in mind. Concerned that an edge criterion of 0.01 mm may be too severe, the local refinement study was performed again, with the criterion increased back to its default setting. Notice that, for the same level of refinement, the reaction force from the strict EC is nearly identical to that from the relaxed EC. At 65 µm, the difference is only 0.36%. However, the relaxed EC offers a significant advantage in element number. In the range from 100 µm down to 65 µm, increasing the EC decreased the element number by an average of 50.1%.

Table 4-5: Edge Criterion = 0.2mm

Size [µm]	F_y [N]	σ_{max} [MPa]	BV [mm^3]	Elem #
40	5.32	1559.4	8.09	649420
50	5.36	1139.2	8.07	523390
65	5.50	1393.5	8.01	331620
75	5.56	579.5	7.96	242550
100	6.06	469.6	7.84	113930
125	6.77	479.8	7.73	61847
150	7.41	421.5	7.62	39847

4.2.4 Edge Criterion as the Independent Variable

Not satisfied with simply resorting back to the default edge criterion, an additional study was performed to determine if the edge criterion could be decreased below 0.2 mm without adversely increasing element number. Using a local element size limit of 65 µm, the EC was varied from 10 to 200 microns. As shown in Table 4-6, there is no consistent trend between the edge criterion and the reaction force. But, biopsy volume trends higher as the EC decreases, which is a sign that the geometry of the STL is being captured in more detail. As a compromise between geometric accuracy and element number, 50 microns was selected for the final mesh.

Table 4-6: Altering Edge Criterion

EC [µm]	F_y [N]	σ_{max} [MPa]	BV [mm^3]	Elem #
10	5.48	2528.0	8.07	592240
25	5.46	2275.9	8.05	472940
50	5.47	2103.0	8.04	382280
100	5.50	1703.3	8.02	344630
150	5.48	1293.2	8.01	334590
200	5.50	1393.5	8.01	331620

4.2.5 Mesh Coarsening

Before arriving at the final settings to create the detailed mesh, mesh coarsening was investigated. Mesh coarsening works by first meshing with small elements to capture the

geometry, and then remeshing the interior with larger elements. In order to compare the results to the minimum element size study, the EC was set to 0.01 mm and a maximum element size of 0.25 mm was used. Two iterations of mesh coarsening were performed, with the worst allowable aspect ratio equal to 0.2. As before, minimum element size was the independent variable. For a minimum size of 65 µm, the coarsening algorithm only reduced the number of elements by 3.4%.

Table 4-7: Mesh Coarsening

Size [µm]	F_y [N]	σ_{max} [MPa]	BV [mm^3]	Elem #
50	5.44	1543.9	8.11	776480
65	5.52	2526.0	8.07	572000
75	5.63	2029.6	8.04	461430
100	6.05	1047.4	7.95	269150
125	6.49	990.3	7.87	169940
150	6.92	939.8	7.78	118270

4.2.6 Combined Settings

Local refinement, a relaxed edge criterion, and mesh coarsening all decreased element number while preserving model fidelity. In order to minimize the element number further still, all three techniques were applied simultaneously. An edge criterion of 50 microns was used. The mesh coarsening parameters were unchanged from those described previously, and the minimum element size was used as the independent variable. Combining all of the mesh refinement methods resulted in a faster convergence than any individual technique, at the lowest element number. Decreasing the minimum size to 40 microns only altered the reaction force by 0.38%, but increased the number of elements by 21.9%. Because the 40 micron minimum provided little benefit, a minimum size of 50 microns was used to mesh the remaining 30 biopsies.

Table 4-8: Combined Settings

Size [µm]	F_y [N]	σ_{max} [MPa]	BV [mm^3]	Elem #	F_{ult}
40	5.52	1563.1	8.10	493420	5.720
50	5.54	869.1	8.09	404590	5.711
65	5.73	1561.2	8.04	288770	5.805
75	5.81	1715.4	7.99	234100	5.859
100	6.14	1315.0	7.89	142520	6.019
125	6.59	1201.1	7.81	92320	6.201
150	7.10	780.7	7.74	66809	6.447

4.2.7 Comparison of all Meshing Methods

The various meshing methods do not appear to converge to a single value, but they all level out around 5.5 newtons. Because of the large variation between the biopsies, the small difference between the methods is not expected to be a concern. The difference between the two most divergent methods at approximately 750,000 elements is only 4.3%.

Figure 4-2: Reaction Force Response to Meshing Method

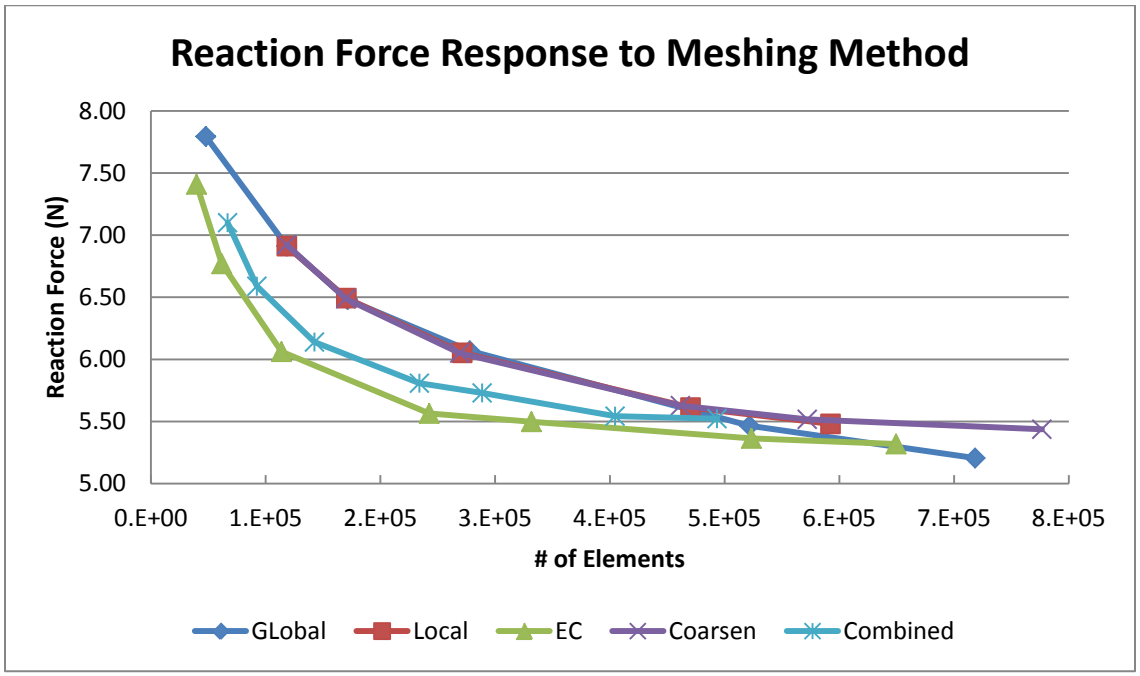

If the geometry were not affected by the meshing method, then one would expect to see the maximum von misses stress converge to a single value. For example, if a simple rectangular beam were being analyzed, the geometry could be captured perfectly with very few elements. In such a simplified case, mesh refinement would alter the solution, but not the geometry. The geometry of the cancellous bone biopsy is comparatively complex, and the geometry changes slightly in response to the mesh density. (Since the tetrahedral elements used have straight sides, they will never capture the true curvature of the domain.) Consequently, the maximum von Mises stress did not converge as reaction force did. The trend is generally upwards, but there are numerous counterexamples in Figure 4-3. The upward trend is likely caused by stress concentrations in the biopsy geometry. With a high stress gradient, smaller elements are less likely to span a region of both high and low stress. Instead, they lie entirely within a highly stressed region.

Figure 4-3: Maximum Von Mises Stress vs. Element #

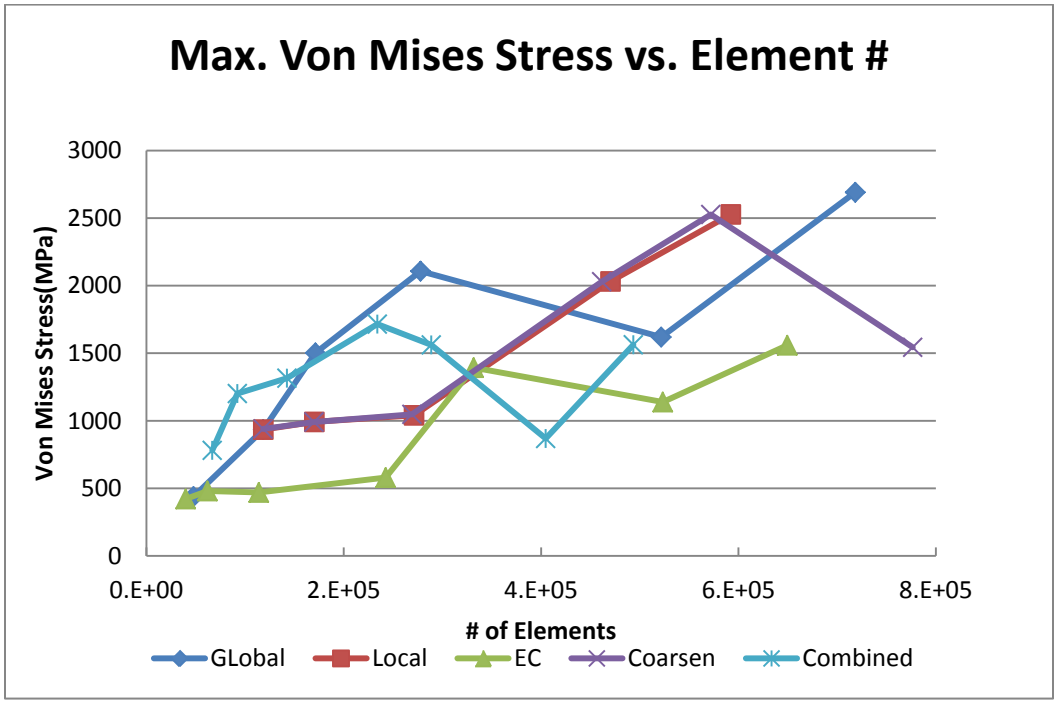

In all cases, increasing the element number increased the bone volume represented in the mesh. The combined methodology arrives at roughly the same volume (8.10 mm^3) as the other methods, but at a much lower number of elements.

Figure 4-4: Bone Volume vs. Element #

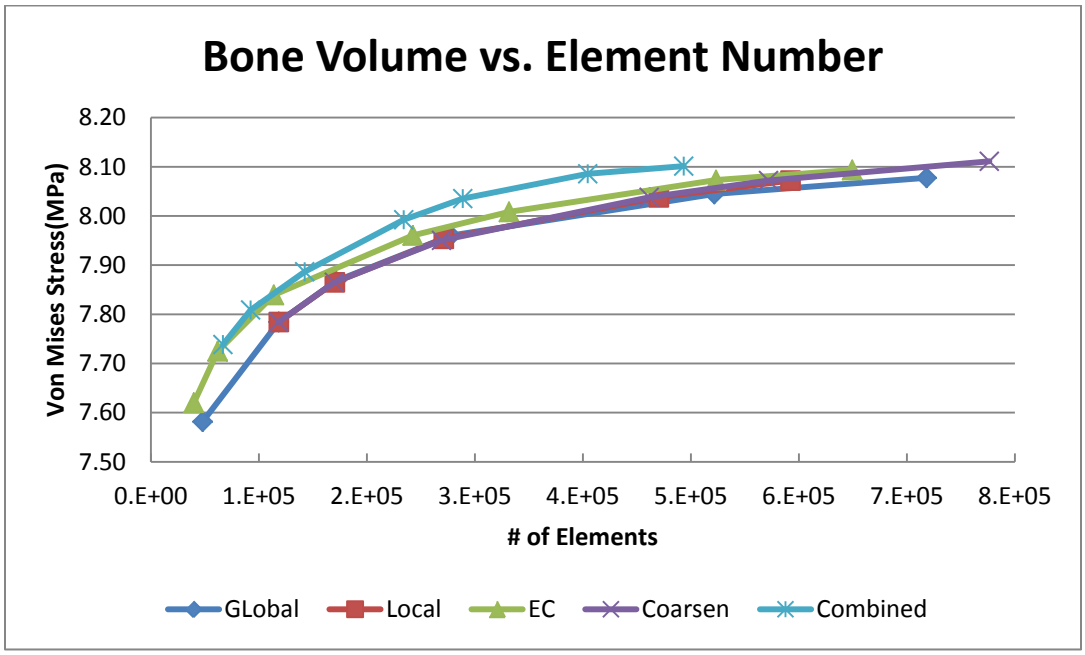

On account of the fact that the von Mises stress had poor convergence, a more reliable failure criterion was needed. Using the combined mesh settings, the accumulated strain based failure method was investigated. The results in Table 4-8 show much better convergence than the von Mises stress. This is logical, because the accumulated damage model is not sensitive to peak values of stress or strain. The steep stress gradients alter peak element values of stress, but they do not change the volume of highly stressed elements. The slight upturn, apparent in Figure 4-5, was unexpected but it is not disconcerting.

Figure 4-5: Strain-Based Failure Load vs. Element #

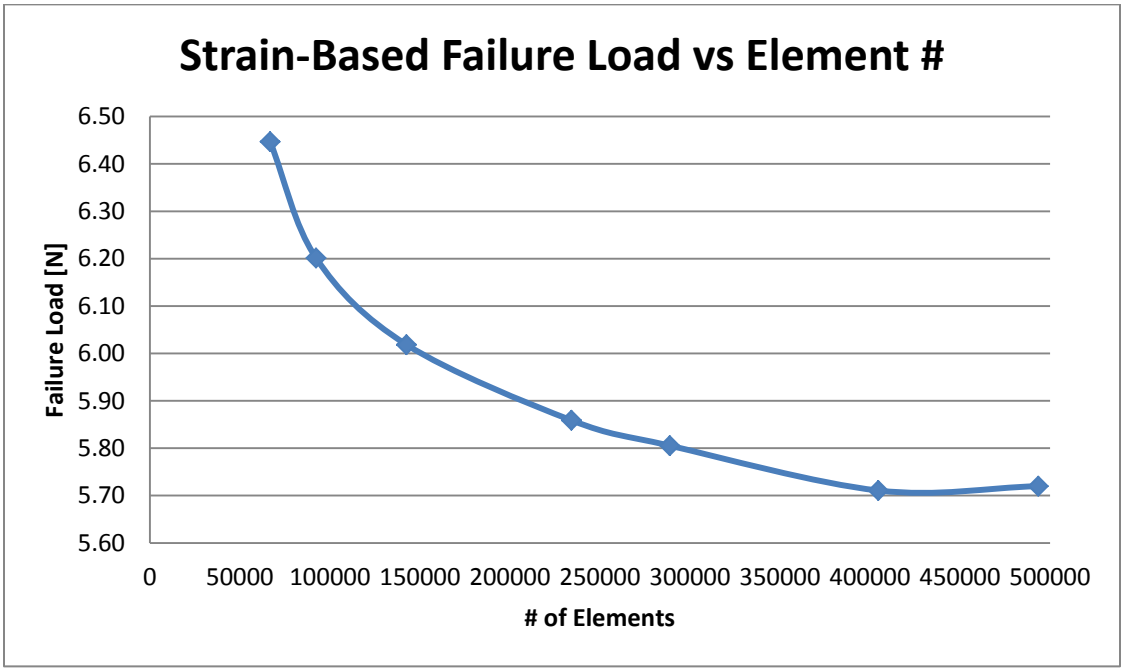

The fine mesh is visibly superior to the coarse mesh. Figure 4-6 shows the old coarse mesh on the left, and the fine mesh on the right. It is clear that the fine mesh better represents the magnified region, but there is still room for improvement. Nevertheless, convergence was achieved for reaction force, so additional detail in regions that small must not appreciably affect the results. Using smaller elements in future studies could give better convergence of the von Mises stress.

Figure 4-6: Coarse-Fine Mesh Comparison

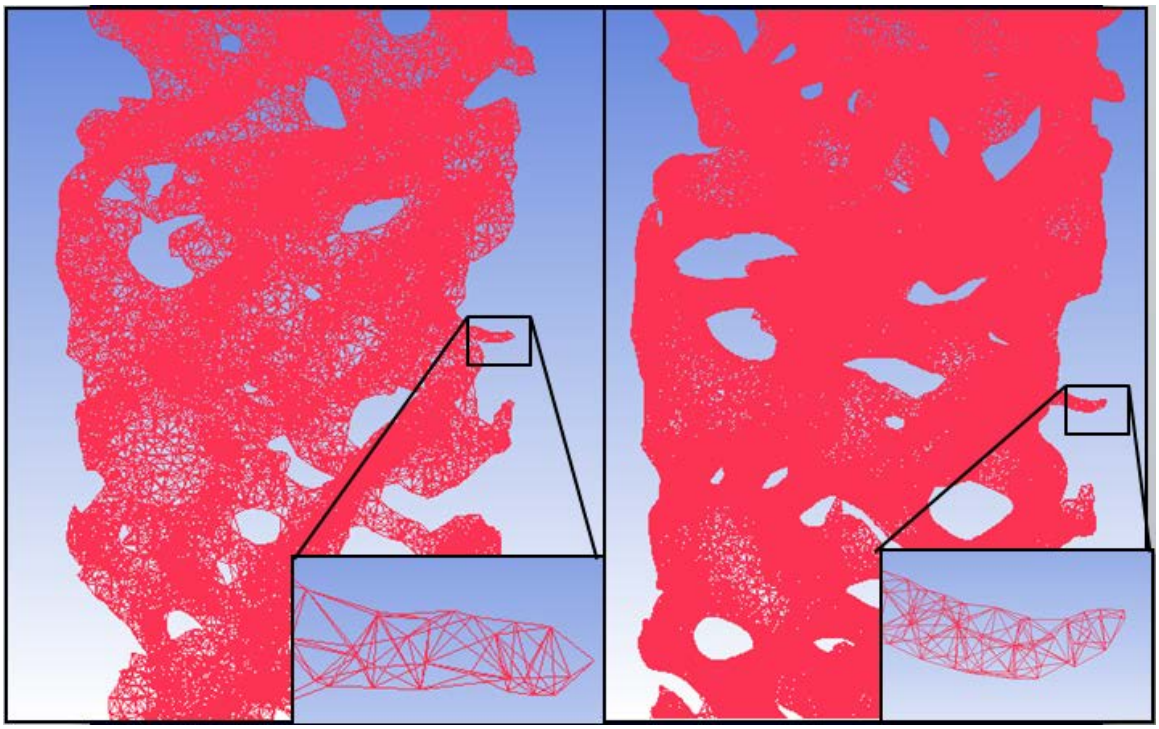

4.3 Fine Mesh Result

Switching from the coarse mesh to the fine mesh, element number increased, on average, by a factor of 10.57. The two largest biopsies by volume, B14 and B24, used slightly different mesh parameters in order to stay within computational limits. The maximum element size used was 0.35 mm, the minimum element size was 0.06 mm, and the edge criterion was 0.1 mm. The smallest model (B055-07) contained 130,930 elements, and the largest (B060-03) was comprised of just over 1.14 million elements. As expected from the convergence study, most of the biopsies had a lower reaction force when analyzed with a higher element density. Two biopsies did buck the trend, however, as Figure 4-7 illuminates. The reduction in reaction force never exceeded 17%. Other properties, such as the modulus of elasticity, had a larger response to element number.

Figure 4-7: Failure Load Response to Mesh Density

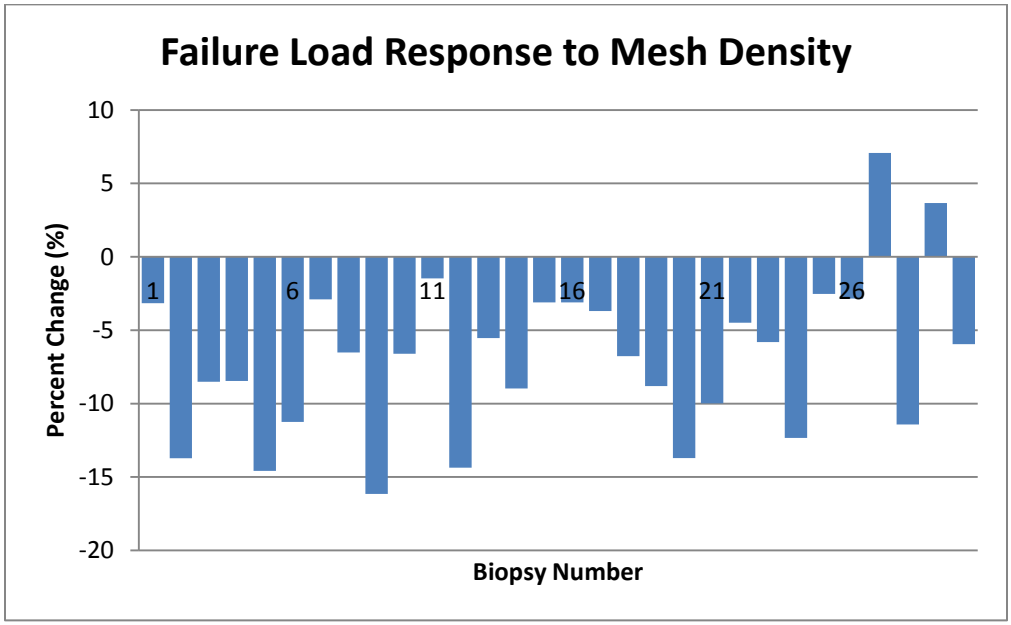

Figure 4-8: Modulus Response to Mesh Density

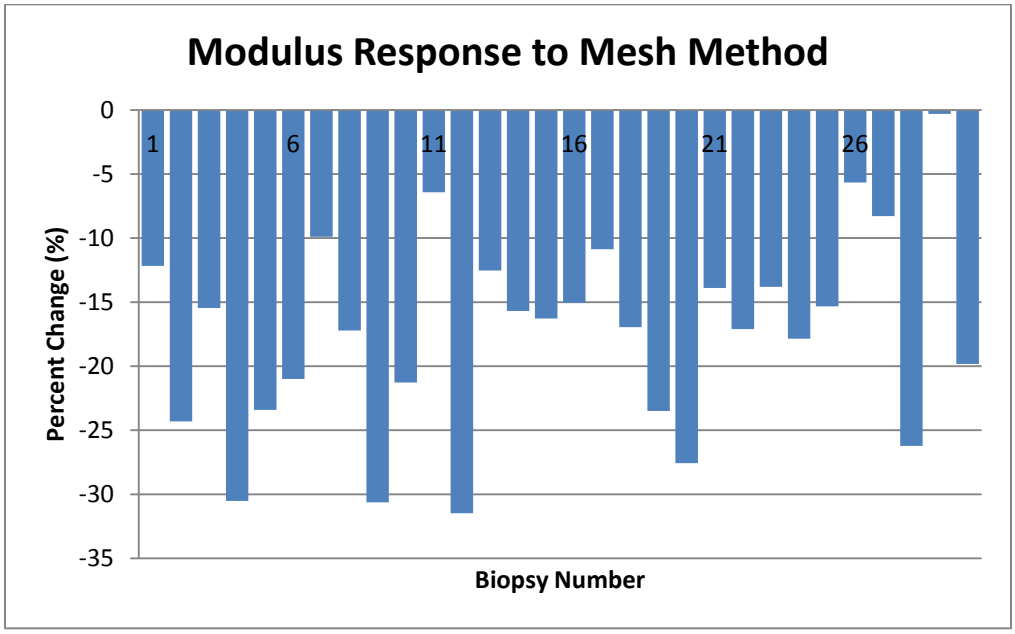

The fine mesh did not have the desired effect of decreasing the standard deviation. The raw data in the form mean±SD is reported in Table 4-9, and coefficient of variation (CV) is compared to the coarse mesh in Table 4-10. For all but the stress amplification ratio, the CV of the fine mesh either increased or was nearly stagnant.

Table 4-9: Fine Mesh Data

Mean ± SD	Control	Short Term	Long Term
E [MPa]	284.8±324.4	517.0±769.0	200.1±184.5
E_{eff} [MPa]	1574.9±1448.8	1663.6±1596.3	1099.0±599.0
SAR	914.1±834.6	1092.3±1823.3	1159.5±1061.7
σ_{ult} [MPa]	1.75±1.46	2.81±3.35	1.48±0.96

Table 4-10: CV for Coarse and Fine Mesh

Coefficient of Variation				
E [MPa]	Coarse	1.100	1.457	0.894
	Fine	1.139	1.487	0.922
E_{eff} [MPa]	Coarse	0.829	0.901	0.481
	Fine	0.920	0.960	0.545
SAR	Coarse	0.738	1.805	1.163
	Fine	0.913	1.669	0.916
σ_{ult} [MPa]	Coarse	0.836	1.207	0.656
	Fine	0.832	1.191	0.645

Table 4-11: Fine Mesh P-Values

	ANOVA	Control vs. Short	Control vs. Long	Short Vs. Long
E [MPa]	0.3454	0.3962	0.4846	0.2337
E_{eff} [MPa]	0.5819	0.898	0.3577	0.3175
SAR	0.9109	0.7835	0.5732	0.9212
σ_{ult} [MPa]	0.3665	0.3763	0.6312	0.2548

Despite the fact that the refined meshing procedure altered the biopsy properties by a substantial amount, it was not enough to improve the statistical significance between the experimental groups. A look back at Table 4-2 proves that the p-values are scarcely different.

4.3.1 Regression Analysis

In addition to calculating p-values to test for significance between groups, the results were analyzed directly against bisphosphonate duration. The separation between short and long term use was admittedly somewhat arbitrary, and it is possible that the decision obscured the true effect of the drug. Unfortunately, the outcome was still not statistically significant. The highest R^2 value, occurring between the effective modulus and treatment duration, was an abysmal 0.0163.

Figure 4-9: Modulus vs. Bis. Duration

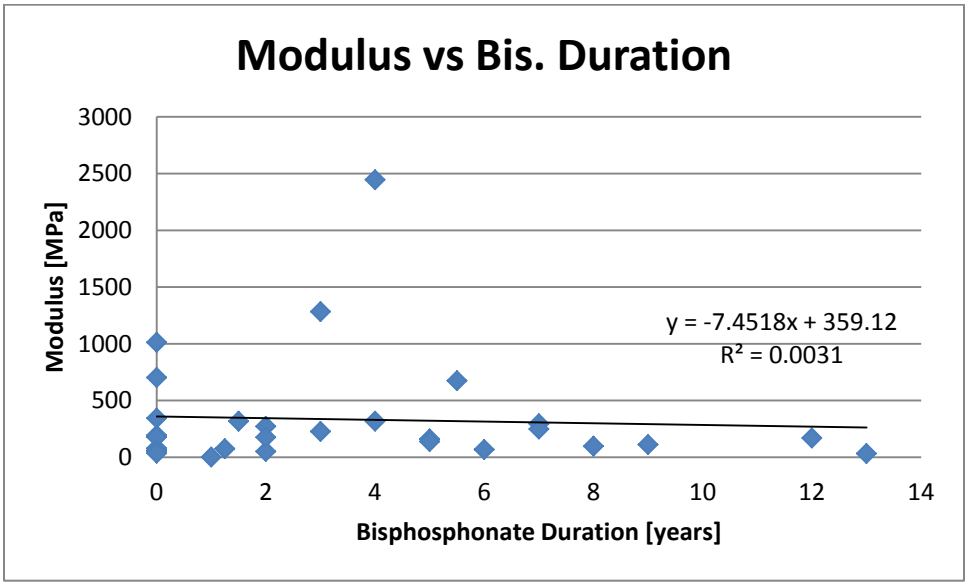

Figure 4-10: Effective Modulus vs. Bis. Duration

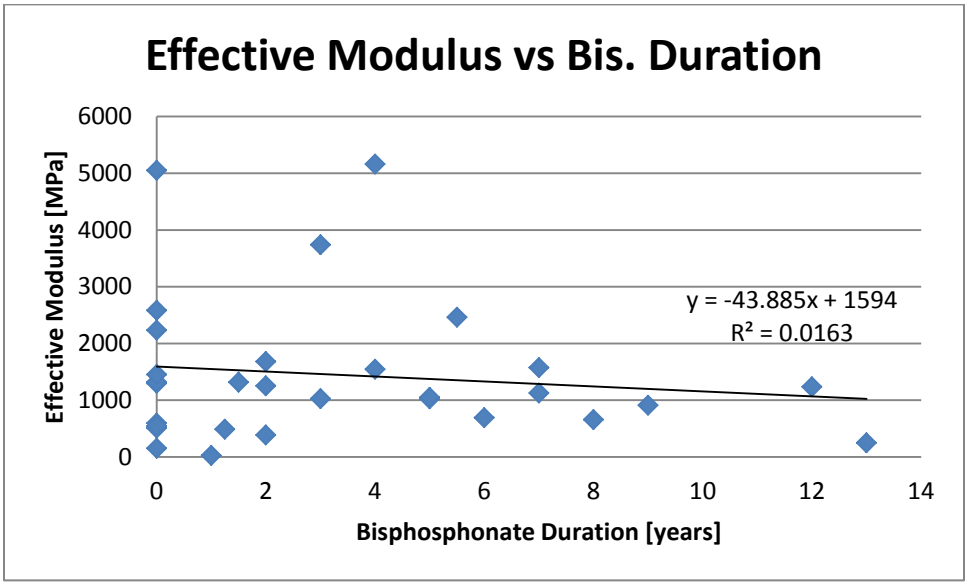

The largest modulus occurred in B21, which had the highest BV/TV ratio (0.47) in the study. It also had the highest effective modulus, but B26 came close by virtue of its lower BV/TV ratio (0.20).

Figure 4-11: Failure Stress vs. Bis. Duration

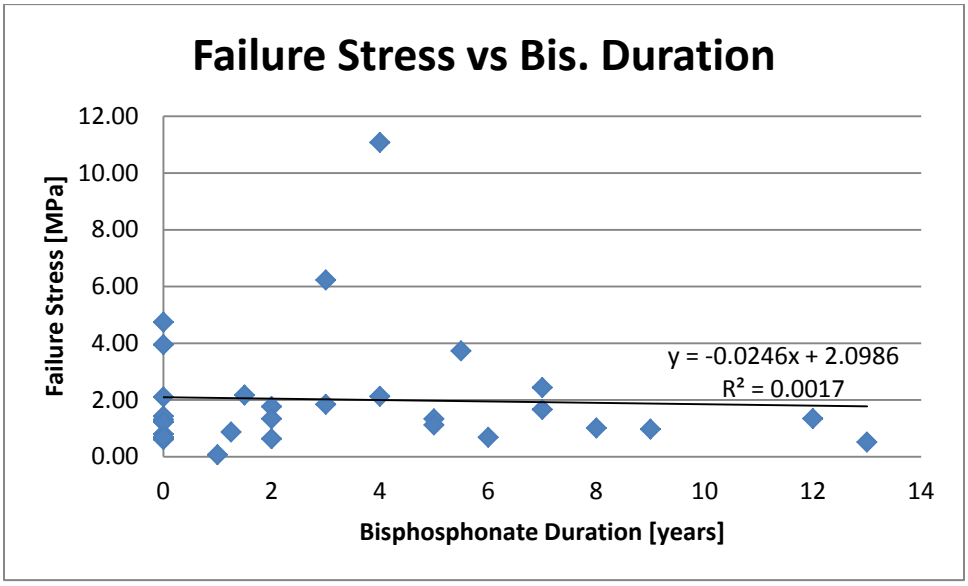

Figure 4-12: Stress Amplification vs. Bis. Duration

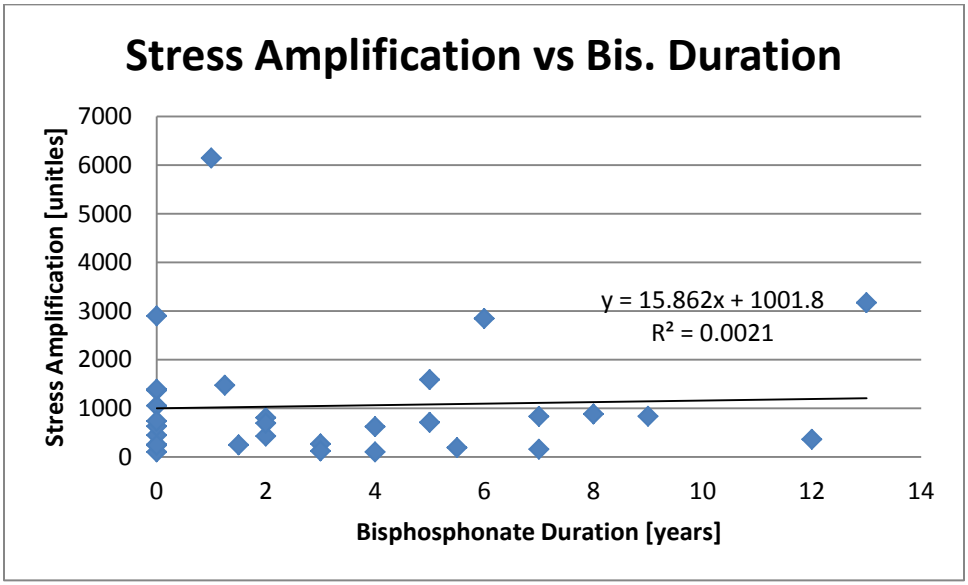

The failure stress and stress amplification ratio show no discernible relationship with bisphosphonate duration. The largest SAR occurred in B19, which had the lowest BV/TV ratio is the study (0.06).

4.4 Statistical Analysis

The basis of most statistical methods is the normal distribution of data. The primary reason for the assumption is that many natural phenomena are a close fit to the Gaussian distribution. Though, since the distribution ranges infinitely in each direction, a perfect fit is rare. For example, a normal distribution applied to this experiment's data would predict the existence of some biopsies with negative strength. In practice, one would not expect to encounter a biopsy with negative strength, regardless of the sample size. Another reason for the normal distribution's ubiquitous use is its ability to be conveniently expressed as an exponential function.

$$f = \frac{1}{\sigma\sqrt{2\pi}} e^{\frac{1}{2}\left(\frac{x-\mu}{\sigma}\right)^2}$$

So, it is justifiable to assume the experimental data follows a normal distribution? Most of the groups failed a Kolmogorov–Smirnov test with a p-value of less than 0.10, which would indicate the data is not normally distributed. Typically, transforming data by taking the inverse or the log can convert it to a normal distribution. After taking the log of the fine-mesh failure load data, it

passed the K-S normality test. However, it had the adverse effect of increasing the p-value from 0.3665 to 0.9290. Taking the inverse of the data did help the normality, but one group still failed the K-S test. The resulting p-value was once again elevated (p=0.5449).

Even with untransformed data, there may be reason to believe that statistical tests based on a normal distribution can be used. The number of biopsies in each group is only 10. For a sample size that small, the K-S test is not powerful enough to reliably determine the distribution of the entire population [79]. Discounting the K-S test, it is necessary to fall back on general statistical principals. The distribution of the entire population is what dictates the applicability of statistical tests, so any evidence of normality in the population will override indications to the contrary in the specific subset collected for this experiment. Unfortunately, bone strength in broiler chickens has been shown to have a log-normal distribution [80]. Experiments in humans have also encountered non-normal distributions [81], sometimes even after transformation [82]. The lack of normality is expected because the variation is due to a large number of interrelated, not independent, variables.

The motivation behind using a normal distribution is the ability to use parametric tests. Non-parametric tests do not assume any distribution, but are not as powerful as parametric tests. That is to say, they are more likely to 'fail to reject' a false null hypothesis (a type II error). On the other hand, if a parametric test is used on non-normal data, the chance of committing a type I error is increased. But, if none of the experimental data comes out to be statistically significant, there is no reason to worry about type I errors. For that reason, a normal distribution is used throughout this research for matters of convenience. In the event that any significant result is found, it will be scrutinized with more rigorous methods.

Even when assuming a normal distribution, no statistical significance was found between the three experimental groups. Looking at Figure 4-9 through Figure 4-12, it is apparent that the data is extremely scattered. In order to see a significant difference, either the standard deviation must be reduced, or more biopsies need to be analyzed. Unfortunately, more biopsies cannot be included from the biopsy bank without altering the inclusion criteria. However, decreasing the standard deviation can be accomplished by removing outliers.

The method chosen to identify outliers was Chauvenet's criterion, which states that a data point may be removed if the probability of obtaining it is less than 1/(2*N). For example, if 10

readings were collected, those with a probability of less than 5% can be discarded. For a normal distribution, 95.4% of data lies within two standard deviations. So, with a sample size of 10, Chauvenet's criterion rejects any point more than 2 standard deviations from the mean.

Rejecting outliers from each group individually would have resulted in discarding many data points. To be slightly more conservative, outliers were only rejected based on the data from all 30 biopsies. The test was performed based on apparent modulus, effective modulus, SAR, and failure load. At a sample size of 30, data is rejected when it is more than 2.394 standard deviations from the mean. When a biopsy was rejected as an outlier based on one parameter, it was removed from the study entirely. For example the SAR for B19 was officially rejected as an outlier. Even though the modulus and failure load for B19 were not rejected based on Chauvenet's criterion, those data points were removed from the calculations. The idea is that the biopsy itself is an outlier, not just one piece of data derived from it.

Chauvenet's criterion identified B21, B26, and B19 as outliers. Biopsy B21 was rejected based on apparent modulus, effective modulus, and failure load. It had a BV/TV of 0.47, which was the highest ratio in the study. It is abnormal for cancellous bone to have such a high ratio, so there was solid ground to reject the biopsy. B26 had the second highest effective modulus. Unlike B21, it had a reasonable BV/TV of 0.20. Referring to **Appendix E**, the microarchitecture of the biopsy stands out. Based on its exceptionally plate-like form, it was rejected without hesitation. Lastly, B19 was rejected due to its large stress amplification ratio. Because SAR showed poor converge, more evidence was needed to comfortably reject it. The biopsy did have the lowest BV/TV ratio in the study (0.06), but more damaging was its poor connectivity. From Figure 4-14 it is evident that the top of the biopsy is only connected to the bottom portion by one trabecula. With the entire load traveling through such a small portion of the biopsy, the results are completely invalid. The von Mises stress, in Figure 4-13, peaks in a highly localized region of the biopsy.

Figure 4-13: Von Mises Stress in B19

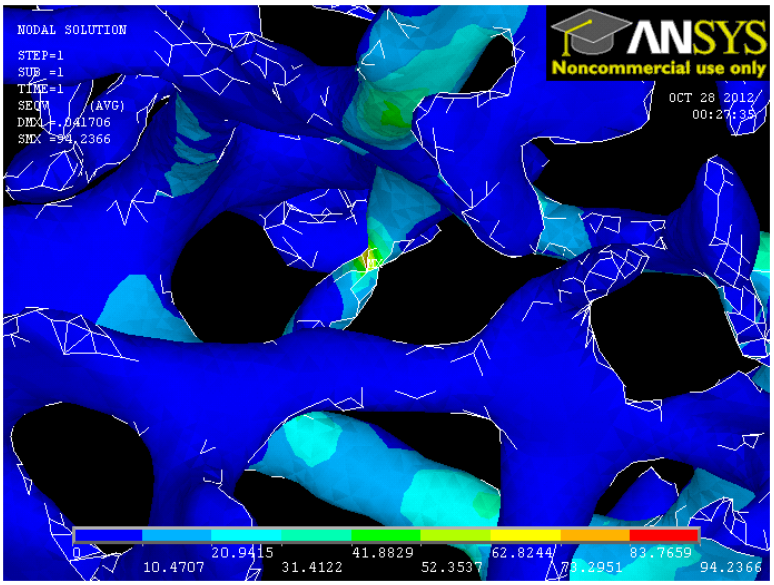

Figure 4-14: Displacement of B19

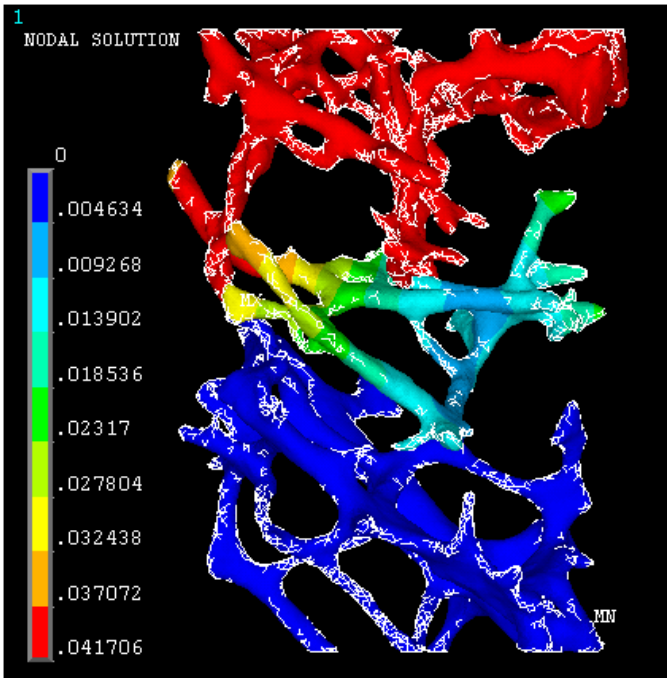

Biopsy B26 was in the control group, and the other two outliers were in the short-term group. The revised data is presented in Table 4-12, along with the unchanged long-term data. Naturally, the standard deviations for the altered groups are much lower than those of the original groups (Table 4-9). However, the change was not enough to produce any significance,

as shown in Table 4-13. In fact, some p-values increased because the difference between the means decreased.

Table 4-12: Fine Mesh Data sans Outliers

Mean ± SD	Control	Short Term	Long Term
E [MPa]	203.9±211.4	340.4±394.4	200.1±184.5
E_{eff} [MPa]	1188.4±825.3	1430.9±1041.5	1099.0±599.0
SAR	1004.2±832.1	583.9±432.1	1159.5±1061.7
σ_{ult} [MPa]	1.42±1.07	2.12±1.75	1.48±0.96

Table 4-13: Fine Mesh P-Values sans Outliers

	ANOVA	Control vs. Short	Control vs. Long	Short Vs. Long
E [MPa]	0.4874	0.4025	0.9675	0.3773
E_{eff} [MPa]	0.6906	0.6806	0.7928	0.4415
SAR	0.3546	0.2091	0.7261	0.1446
σ_{ult} [MPa]	0.4648	0.3448	0.8941	0.3738

4.5 Fixed-Length Finite Element Analysis

In a final attempt to decrease the variability of the data, the biopsies were analyzed at a fixed length. After removing the cortical bone, the length of the biopsies ranged from 4.56 mm to 16.21 mm. The inconsistency in length was not thought to be an issue because a constant strain was applied. However, it is conceivable that the length confounded the results. For example, a long biopsy would be more likely to contain a weak region than a short biopsy, even if both were taken from two identical bones. Consider the analogy of a chain composed of many links. If the individual link strengths are normally distributed, and the chain strength is dictated by the weakest link, then the mean strength of longer chains will be less than that of short chains. The principle has been applied to spun yarn [83], and could arguably be extended to compressive strength of materials with microarchitecture.

The analyzed length was set to be slightly less than the shortest biopsy: 4 mm. This value was chosen to maximize the volume of bone analyzed, while still ensuring that all of the biopsies had some material removed from each end. As well as giving all biopsies an equal probability of containing a weak region, fixing the analyzed volume to a set length had two secondary benefits. First, by analyzing the central portion of each biopsy, any remnants of cortical bone that may have been included in the initial analyzes were removed. Second, the decreased bone volume allowed biopsies B14 and B24 to be analyzed without relaxing the meshing parameters.

Table 4-14: Fixed-Length Data

Mean ± SD	Control	Short Term	Long Term
E [MPa]	331.4±374.4	682.2±837.1	239.5±196.3
E_{eff} [MPa]	1994.1±1807.1	2333.8±1877.6	1458.1±658.0
SAR	701.8±665.2	889.5±1890.2	621.5±687.9
σ_{ult} [MPa]	1.93±1.69	3.60±3.93	1.61±0.96

Table 4-15: CV for Fixed and Original Length Analyses

Coefficient of Variation				
E [MPa]	Fixed L.	1.130	1.227	0.820
	Orig. L.	1.139	1.487	0.922
E_{eff} [MPa]	Fixed L.	0.906	0.804	0.451
	Orig. L.	0.920	0.960	0.545
SAR	Fixed L.	0.948	2.125	1.107
	Orig. L.	0.913	1.669	0.916
σ_{ult} [MPa]	Fixed L.	0.875	1.092	0.596
	Orig. L.	0.832	1.191	0.645

Table 4-16: Fixed-Length P-Values

	ANOVA	Control vs. Short	Control vs. Long	Short Vs. Long
E [MPa]	0.1748	0.2496	0.5041	0.1379
E_{eff} [MPa]	0.4556	0.4123	0.397	0.1914
SAR	0.8818	0.7726	0.7941	0.6817
σ_{ult} [MPa]	0.1892	0.2421	0.6103	0.1517

The fixed-length analysis had coefficients of variation similar to the original-length analysis, yet the ANOVA p-value was reduced in every category. The failure load p-value was reduced from 0.3665 to 0.1892. Of course, that is still well above any commonly-used significance threshold.

Unlike increasing the mesh density, which had a unilateral effect on the failure load and modulus, reducing the region of analysis had a more bidirectional influence. The magnitude of the change was also far greater than when modifying mesh density. The greatest change in failure load going from the coarse mesh to the fine mesh was -16.15%, but the largest change when switching to the 4-mm analysis was 106.08%. The apparent modulus (Figure 4-16) experienced even greater alteration: 190.5%.

Figure 4-15: Effect of Reduced Length on Failure Load

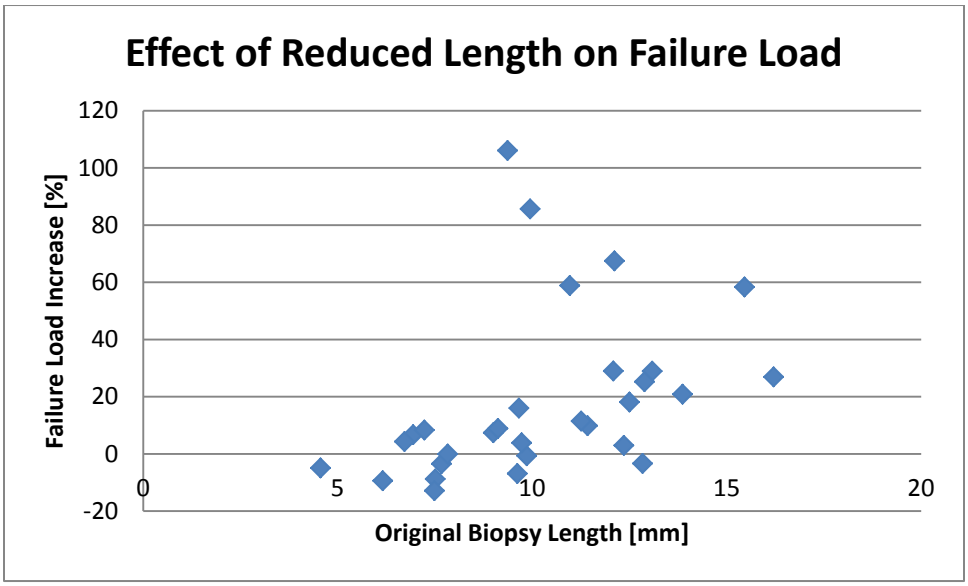

Figure 4-16: Effect of Reduced Length on Apparent Modulus

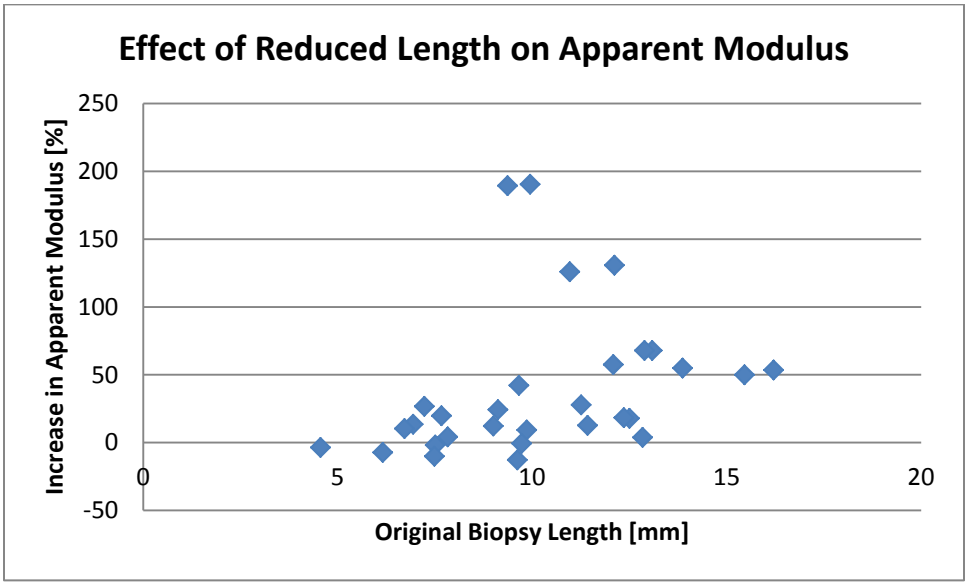

Figure 4-17: Effect of Reduced Length on BV/TV Ratio

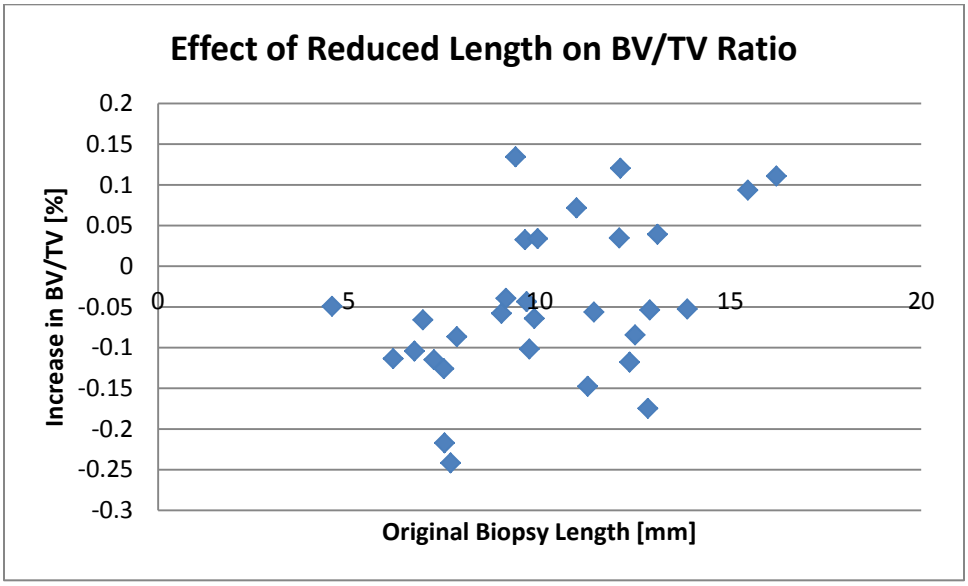

The percent increase in failure load and apparent modulus show a slightly upward trend with original biopsy length. This justifies the rationale behind performing the fixed-length analysis in the first place. The BV/TV ratio, in Figure 4-17, exhibits a surprising amount of variation. If the amount of cross sectional area being analyzed was enough to represent the cancellous bone, less disparity in BV/TV would be expected. The small analyzed bone volume could be responsible for the lack of significance.

Chauvenet's criterion was applied to the fixed-length data, and 4 biopsies were removed. Three of the biopsies were the same ones rejected during the original-length analysis. The newly discarded biopsy (B24) was rejected based on apparent modulus and failure load. It had the second highest BV/TV ratio in the study (0.375). More importantly, it has a streak of cortical bone down its right-hand side as shown in Figure.

Table 4-17: Fixed-Length Data sans Outliers

Mean ± SD	Control	Short Term	Long Term
E [MPa]	235.4±232.7	351.9±281.0	239.5±196.3
E_{eff} [MPa]	1492.6±918.9	1780.8±915.4	1458.1±658.0
SAR	771.5±665.7	361.9±314.5	621.5±687.9
σ_{ult} [MPa]	1.53±1.16	2.08±1.21	1.61±0.96

Table 4-18: Fixed-Length P-Values sans Outliers

	ANOVA	Control vs. Short	Control vs. Long	Short Vs. Long
E [MPa]	0.55	0.3949	0.9678	0.3826
E_{eff} [MPa]	0.7041	0.5436	0.9272	0.4427
SAR	0.4159	0.1321	0.636	0.314
σ_{ult} [MPa]	0.5791	0.3734	0.8616	0.414

With the exception of SAR, all of the p-values increased after removing the outliers. Just as when outliers were removed from the original-length analysis, the movement of the means counteracted the decreased standard deviations.

5 Discussion

5.1 Determination on the Use of Bisphosphonates

Based solely on the data collected, the null hypothesis could not be rejected. However, that does not conclusively mean that the null hypothesis is true. Ultimately, no confident decision can be made about the long-term efficacy of bisphosphonates from this research. The problem lies in the fact that the statistical power of the test was quite low. (The probability of rejecting a false null hypothesis is statistical power.) G*Power v3.1.5 software was used to assess the power of the experimental data post-hoc with α=0.05. For simplicity, only the failure load in the fixed-length analysis is considered here. Comparing the short and long-term groups, the power is 31.3% (effect size=0.6956). That means the probability of committing a type II error is 68.7%. In order to have a power of 80% with the same alpha and effect size, 34 biopsies would be needed in each group. Moreover, the case just presented had one of the lowest p-values of any t-test in this research. Looking at a more representative match-up, like the one between the control group and the long term group, the power is only 7.8% (effect size=0.233). For that effect level, 291 biopsies would be needed in each group to have 80% power.

While the data obtained from the iliac crest biopsies did not show significance, it does match up well with published properties for cancellous bone. Based on physical tests of 48 cylindrical (ø=8mm, L=25mm) cancellous bone specimens, Kopperdahl and Keaveny found that the compressive modulus ranged from 100 to 500 MPa [90]. The stress at yield varied from 0.5 to 3.6 MPa. The median apparent modulus of all 30 biopsies in this study was 212.6 MPa; the median failure load was 1.46 MPa. So, the data collected is centered about well-established properties for human cancellous bone.

The range of the data, however, was greater than that observed by Kopperdahl's research. The disparity may be attributed to his exclusive use of low-density (0.18 +/- 0.04 b/cm^3) specimens, or a difference in anatomical site between the two studies. Cohen et al, found that the FEA-derived modulus of trabecular bone from transiliac biopsies (n=54) was 660±485MPa [85]. His range was 79-2165 MPa, compared to 1.6-2430 MPa in this research.

5.2 Sources of Variation

No research is perfect, particularly in the medical field where experimental design must take a back seat to ethical considerations. It simply is not practical to control every possible variable.

For instance, dictating exercise levels, calcium intake, and ethanol use was not feasible in this study. As the sample size increases the law of large numbers takes over, and the uncontrollable variables—assuming they are independent—should have an equal effect on each experimental group. Unfortunately, it was not possible to increase sample size while maintaining age-matched low-turnover groups. Aside from the small sample size, the power may have been reduced by inadequate biopsy dimensions, lack of control over biopsy orientation, deviation in biopsy location, and sub-optimal geometry capture.

5.2.1 Biopsy Size

The high variability in the FEM estimated failure load most likely stems from the fact that most of the biopsies in this study are only 3 mm in diameter. From there, many of them were cut in half, reducing the usable volume down even further. Trying to extract structural information from a sample that small is difficult. As the biopsy is harvested, a large number of trabecular connections are severed. Each of those connections had a capability to transmit load, but there is no way to accurately model those load paths. The method used in this study to deal with the broken connections is the same as that encountered in the literature, which is to leave them unconstrained. That boundary condition is not how the bone behaves in-vivo, but it does accurately portray a compression test on the extracted bone.

According to Harrigan et al., a representative volume of cancellous bone must contain at least 5 intertrabecular lengths [84], which is 3-5 mm. The cross sectional area of the vertical iliac biopsies in this study ranged from 2.91 to 15.16 mm^2 (8.18±3.03 mm^2). Fourteen of the 30 biopsies in this study had an area less than that of a 3-mm-diameter circle (7.07 mm^2). Even more had at least one bounding dimension less than 3 mm. None of the cross sectional areas exceeded the area of a 5-mm-diameter circle. Published studies which analyze bone biopsies via µFE invariably use more than a 3 mm diameter; a 7.5 mm diameter transiliac biopsy is typical [49,85,86]. HR-PQCT studies utilizing finite element analysis usually analyze the entire cross section of the distal radius [59,87,88]. Studies measuring cancellous bone strength experimentally tend to use cylinders around 8mm in diameter [89,90].

The enormous changes that resulted from using a 4-mm-long region of interest lend credence to the fact that the biopsies in this study are too small for reliable finite element analysis. The intra-bone variation at this size scale caused the estimated failure load to more than double for some biopsies, and decrease by as much as 12.8% for others. On average, the BV/TV ratio was

altered by 9.76%. Had the cross sectional area been larger, the biopsies would have behaved more like a uniform material, instead of a location-dependent structure. In order to obtain a larger cross section in the future, it would not be out of the ordinary to use a 5-7 mm drill for vertical biopsy collection [91].

Biopsy shape has also been shown to have an effect on strength and modulus. Keaveny, et al., compared the mechanical properties of cancellous bovine bone in the form of cylinders (D=5mm, L=10mm) and 5mm cubes [92]. The modulus of the cubes was 36% higher ($p<0.01$) than the cylinders, and their strength was 18% higher ($p<0.05$). The biopsies in this research were cylinders, half-cylinders, or rectangular prisms. The range of shapes unquestionably increased the amount of variation in the data.

A small biopsy leaves less material to analyze, and it also increases the likelihood of altering connections within the biopsy volume. Assuming the interior portion of the biopsies survived drilling unscathed, the act of handling the removed biopsy still presented an opportunity for breaking central trabeculae. This concern is particularly relevant for poorly connected biopsies with low BV/TV.

5.2.2 Biopsy Orientation

Because of the small biopsy size and the use of previously collected biopsies, there was no control over the exact orientation of the biopsy with respect to the pelvic bone. For the vertical biopsies, the entry angle of the trocar dictated the axis of the applied load in the finite element analysis. It is not reasonable to assume that the physician collecting the biopsies used a constant angle, especially considering the fact that no single physician collected all of the biopsies. For the transiliac biopsies, the axis of loading was determined by the VOI defined during the microCT scan. The VOI was selected so that it would be in the same plane as the vertical biopsies, but there was no way to orient them in the same direction. Since there was already angular uncertainty in the vertical biopsies, the lack of knowledge about transiliac orientation was not seen as an impasse. That being said, the lack of control should not be ignored. Since bone adapts to the loading conditions that it is put under, it is expected that biopsy orientation would have a large effect on biopsy strength. Imagine a plate-like architecture such as in biopsy B26. The biopsy would be strong when the loading is in the plane of the plates, and weak when the loading is out of plane.

5.2.3 Biopsy Location within the Ilium

While orientation is important, location also plays a role in biopsy strength. Imagine if a patient had a large number of iliac biopsies performed. Naturally, there would be some distribution to the biopsy strengths. The question is, just how large is the variability? And, how does the variability change as a function of biopsy size? Cancellous bone is non-homogenous and has large features in comparison to the trocar diameter used in this research. Consequently, the deviation between biopsies collected from the same patient could be quite great. Further complicating matters, this study did not take its bone from a consistent portion of the collected biopsy. Many of the biopsies were split into multiple pieces, and no effort was made to always select the same portion. The decision was made because there was no quick way to identify the location of each segment with respect to the whole. In some cases, not all segments were even available because prior research rendered them poor candidates for structural analysis. If each experimental group had a large number of patients, the location variability may not be an issue. With only 10 biopsies per group, every source of variability must be mitigated. Even then, there is no guarantee of statistical significance when extrapolating bone strength from a small portion of bone.

5.2.4 Capture of Biopsy Geometry

Sub-optimal biopsies may be the cause of some of the variation seen between the groups, but there is no changing the biopsies presently in the collection. In order to make the existing biopsies more useful, it may be possible to reduce the erraticism of the downstream operations. There is no guarantee that increasing the fidelity of the scanning, meshing, and analysis would decrease variability, but it is a goal that should be strived for nonetheless.

Even with presently available equipment, the scan could be performed at a higher resolution. A pixel size of 6 microns would be achievable with a sample tube diameter of 12.3 mm and an image size of 2048x2048 pixels. (SCANCO rates the µCT40 at a resolution of <8 microns.) The finer resolution would require more computational power from all subsequent operations, but could potentially be fruitful. Using the 12.3 mm sample tube would require that the biopsies be embedded in a smaller diameter of acrylic. Alternatively, they could be machined down in their present casting.

Before going to that extreme, it should be considered that several studies use a scan resolution near to or greater than 30 microns. Harrison et al. have used a 30 micron voxel size [93] and a

36 micron size [55] to study ovine trabecular bone. An experimentally validated model of a rat vertebra was created by Naomi and Wroe with 75 micron resolution [94]. A myriad of HR-PQCT studies use a voxel size of 80 microns [59,88,95].

On the other side of the coin, there is evidence to suggest that scan resolution can play a large role on the outcome of FEA studies. Using vertebral trabecular cores (D=8mm, L=25mm) Bevell et al. found that increasing the resolution from 20 µm to 40 µm increased the modulus by 42% [97]. Perhaps in an effort to avoid this, multiple studies use a resolution below 20 microns. Liu, Cohen, and others have successfully used 8 micron scanning resolutions [49,81].

Using a higher resolution would make a finer greyscale image of each slice, but the thresholding parameters are ultimately responsible for the bone geometry analyzed. More effort on that front could be beneficial to the accuracy of the model. For example, it may be worthwhile to alter the threshold value until the volume of the model matches the experimentally determined volume of the biopsy [96]. Others have used a variable threshold based on the maximum greyscale value [85].

5.3 Limitations of Study Design

5.3.1 Scope Limited to Cancellous Bone

On top of the variation due to biopsy orientation and location, there are other fundamental factors limiting the applicability of this research. Chief among them is the fact that the research is limited purely to cancellous bone. Fractures are not seen solely in cancellous bone. Fractures occur across the entire bone cross section; both the cancellous and cortical regions fail. Any study limited to only one type is incomplete. Boutroy et al. have found that the percent of load in the distal radius carried by cancellous bone (64%) is greater in fracture patients than control patients [53]. Rats treated with strontium ranelate display a load distribution which is shifted 8% in favor of cortical bone, whereas untreated rats carry an equal amount of load between cortical and cancellous bone [48]. Both of these studies demonstrate that looking at only one type of bone is a risky proposition. At common fracture sites, neither type of bone dominates strength.

That said, the approach is justified on the basis that is does provide some information. For the same amount of cortical bone, weaker cancellous bone will result in lower fracture loads. Also, osteoporotic fractures frequently occur in bones with a large percentage of cancellous bone,

notably vertebrae [2]. Cortical bone has a simple geometry, and its strength can be estimated by measuring its thickness [98]. Cancellous bone is not so simple. Trabecular thickness influences the strength of cancellous bone, but unlike cortical bone it is also affected by connectivity and microarchitecture [49]. So, applying microCT to capture cancellous geometry has merit. However, it must not be forgotten that cancellous bone strength is far from predicting fracture loads. It is only one variable correlated to global failure.

5.3.2 Biopsy Location within the Skeletal System

Accepting the fact that cortical bone is being ignored, there is still a concern regarding the location of cancellous bone used in this study. The ilium is not a frequent fracture site in osteoporotic patients, accounting for only 7% of osteoporotic fractures [2]. Atraumatic fractures typically occur in the vertebrae, and traumatic fractures commonly befall the hip and wrist. While there is a relationship between bone parameters at the ilium and other locations, it still acts as one more layer of complication draped over the already convoluted matter of accurately determining the effectiveness of bisphosphonates. Lamentably, it is not ethical to take biopsies from sites prone to fracture in live patients. The stress concentration from the missing bone would increase the already-elevated risk of fracture. Even if more pertinent biopsy locations were feasible, it would be a moot point; the entire reason for this study's existence is to utilize an existing collection of iliac biopsies.

5.3.3 Inaccurate Boundary Conditions

Even limiting the focus to cancellous bone, the loads applied to the bone in-vivo should be applied to the extracted biopsy. That wasn't done. Consistent with common practice [59,85,92], the biopsies were analyzed for a state of pure compression. Such a loading condition is rarely, if ever, encountered in the ilium. Even elsewhere in the body, an evenly distributed compressive load is hard to imagine. For any biological loading, the applied forces will occur at the joints and at the points of ligament/tendon attachment. In the case of traumatic fracture, loads may be introduced at any point due to impacts with outside objects. In all instances, the true applied load is a combination of axial, bending, torsional, and shear stresses. Moreover, the joints create Hertzian contact stresses, and the tendons and ligaments introduce point loads. In order to predict bone failure, all of the stresses should be modeled. With a small biopsy, modeling the complex loading condition is not practical. Since a simplification had to be made, compression was chosen as the closest achievable analog to biological loading.

Atraumatic fractures, which occur without large external loads, may come closer to a state of uniaxial compression than traumatic fractures. Nonetheless, it would be preferable to model and analyze an entire bone.

5.4 Simplifications in the Finite Element Model

5.4.1 Initially Stress-Free

The fundamental assumptions of a linear elastic model were discussed in the methodology section. In addition to the fundamental assumptions of the model itself, there are a number of assumptions typically made in applying it. For instance, it is assumed that there is no initial stress in the material. Stress in a body with no externally applied loading is called residual stress, and can work for or against a structure. Bone tissue does have residual stresses [99,100], but they were not modeled due to the difficulty of determining the proper values over the complex microarchitecture.

5.4.2 No Buckling Considerations

On top of not modeling residual stress, no buckling behavior was considered. With thin trabeculae, buckling failure may precede material failure. Performing a geometrically nonlinear finite element analysis could better model regions with high deformation and capture any buckling behavior. Linear analysis is the dominant type of FEA in medical research due to its low computational demands and scaling ability, but there is evidence to suggest that nonlinear finite element models are better at predicting failure load when the resolution is 80 microns or less [101,102]. On the other hand, research by Macneil and Boyd supports the use of a linear model to predict bone strength at a resolution of 82 microns [103]. So, while nonlinear analysis has been employed on cancellous bone before [51,55], this research used a linear model for convenience.

5.4.3 Homogenous Material Properties

Just as important as the previous assumptions, the bone material was assumed to be homogeneous, isotropic, and linear. The mechanical properties of trabecular bone are not homogeneous. Rather, they change depending on the location within a trabecula. In one study, the elastic modulus at the center of intertrochanteric trabeculae was 17% higher than that at the exterior [104]. The difference was attributed to variations in mineral and collagen composition. In an effort to capture the heterogeneity of bone material, researchers have

scaled the material properties of bone based on its radiodensity. When correlating calculated and measured failure load, Macneil et al. found that scaled properties improved the R^2 value from 0.972 to 0.983 (N=31) [103]. Harrison et al., using heterogeneous material properties, were able to accurately determine the apparent modulus of ovine bone [93]. Nevertheless, using homogenous properties is commonplace in order to reduce complexity. Heterogeneous properties are relatively easy to apply when the structural mesh is composed of brick elements taken directly from the image voxels. The mesh in this study was based on the STL geometry, so it would have been difficult to map the radiodensity to the mesh.

5.4.4 Isotropic Material Properties

The mechanical properties of bone are also not isotropic [105,106]. This is expected based on the anatomy of bone. It is not formed as one continuous lump; it is laid down in layers. At the smallest length scale the material of bone itself—collagen fibers and hydroxyapatite mineral—behaves like an anisotropic composite material. Utilization of anisotropic properties to model the mandible has been shown to increase peri-implant stress [107]. There is no doubt that modeling the full anisotropic behavior would be best, but it may not be a fruitful endeavor. In diaphyseal cortical bone it is fairly straightforward to apply orientation-dependent properties. In cancellous bone, there is no simple way to accomplish the feat. A coordinate system would have to be created for each trabecula, which is not practical to do manually. An algorithm to estimate the correct orientation for each element would be necessary. Additionally, research on 29 trabecular whale bone specimens discovered that 92% of the variation in Young's moduli was explained by scaling to a constant tissue-level modulus [108]. When using the modulus of the individual samples, the correlation improved to 95%. The researchers concluded that using an "effective isotropic tissue modulus" is an acceptable practice. Accordingly, the isotropic generalization is widely used [55,59,88,93,94].

5.4.5 Linear Material Properties

Bone material, when considering failure, is not linear [106]. By using a linear material model it is impossible to capture the post-yield behavior of the biopsies. The portion of the stress-strain curve for bone after yield is significant, and contributes to the toughness of bone. On the whole-bone level, post-yield behavior may not need to be considered because yield on that scale is a form of failure in itself. However, even for relatively low apparent strains, trabeculae

can undergo large deformation. Ideally, the material in the highly-strained regions would be modeled with the full and accurate stress-strain characteristics of bone.

5.4.6 Failure Theory

No matter how well the material properties are modeled, the final results depend on the application of an appropriate failure criterion. The von Mises criterion is commonly utilized on ductile materials when designing to the yield strength of the material. In order to analyze materials prone to brittle fracture, other criteria should be considered. The maximum principle stress criterion is often applied to brittle materials. The Coulomb-Mohr criterion handles materials which—like bone—have different strengths in tension and compression. (The von Mises criterion can be modified to account for the different strengths [51].) Based on bone's anisotropic nature, the Tsai-Wu failure criterion would be a respectable choice for any researcher successful in modeling the true material properties of cancellous bone. As explained in the methodology, this study uses an experimentally-determined strain accumulation failure criterion. It is popular, but it still has room for improvement.

One notable limitation of the failure criterion in this research is its inability to account for fatigue failures. Osteoporotic bone failure is often a result of cyclic loading, not large static forces. High-trauma fractures do occur by one-time overload, but that opens up a Pandora's Box of modeling issues. The properties of any material, bone no exception, are dependent on the strain rate. To accurately analyze a high-trauma event would require a dynamic model and rate-dependent material properties. Applying such a model to a small vertical core of cancellous bone would not be sensible. Fatigue failures occur by the generation, growth, and coalescence of cracks. The cracks have openings around 1 micron in width [89], hence they cannot be modeled by the SCANCO microCT-40. It is possible to capture their geometry using nanoCT scanners, but the field of view would be severely limited. Even if a representative volume of cancellous bone were scanned at the resolution needed to see microcracks, the computational demands of the FE analysis would be astronomical.

To investigate the effects of cyclic loading and use a tractable number of elements, Guo at al. developed an idealized model of trabecular bone [109]. Using Paris' Law to estimate crack growth and element death to remove broken trabeculae, the results for the high-cycle low-stress analyses were not statistically different ($p>0.2$) than experimentally-obtained S-N curves for bovine trabecular bone. In the future, his methods could be applied to the non-idealized

geometry of scanned biopsies. Commercial software, e.g., ANSYS nCode DesignLife, could also assist in the fatigue analysis.

5.4.7 Summary

The limitations mentioned above seem to cast doubt on the finite element analysis, but it is undeniably a useful analytical tool. The calculation of actual stress and strain in bone is far more meaningful than any structural index. Despite all of the assumptions used, the finite element analysis in this study positively assesses the quality of microarchitecture, which is a major component of cancellous bone strength. Some of the simplifications in the mathematical model have a minimal effect on the outcome, and are only of interest when attempting to explain the last bit of variability in test data. Even if an assumption caused the solution to deviate significantly from the true value, all three groups would be exposed to the same method. So, in effect, they would have been treated equally and caparison between them would still be valid. Unfortunately, in this study, it was not possible to validate the computational results with experimental values. Doing so would destroy the biopsies, eliminating the possibility of their use in all future research.

5.5 Limitations on the Interpretation of Results

Supposing this research had produced a statistically significant difference between short-term and long-term bisphosphonate use, it is crucial to bear in mind that it only would have proven a correlation between bisphosphonate duration and bone strength, not causation. There are a multitude of outside variables which could have caused both the longer duration of bisphosphonate use and the decreased bone strength. As a purely hypothetical example, suppose there is some set of patient characteristics which causes bisphosphonates to be ineffective. Patients with these characteristics would not show much improvement in bone strength. As a result, their bones would still be relatively weak, even after a long period of using bisphosphonates. Patients without the characteristics would show improvement in BMD, and potentially discontinue use of the drug. After looking at the entire pool of patients, it would be tempting to conclude that long-term use decreased patient bone strength. Whereas, in reality, it never did anyone any harm. It helped one subset of people, and was ineffective on the other.

Since the groups in this research are age-matched, it is necessarily true that the long-term use group started bisphosphonate treatment at a younger age. Perhaps they became osteoporotic at an earlier age due to a genetic predisposition to weak bones. As a result, they would remain

on bisphosphonates for a longer duration, and have weaker bones. Patients without the predisposition would require shorter treatment periods, and have stronger bones. As in the previous example, a confounding variable resulted in a misleading correlation. Although this time the confounder was severity of osteoporosis, and not drug efficacy.

5.6 Applicability of the Method

The method developed in this research, while replete with simplifications, is still a useful tool for the analysis of cancellous bone tissue. Though it did not show statistical significance, the blame cannot be placed exclusively on the finite element modeling. A large amount of variation is inherent in trabecular bone, and it was exacerbated by the small cross-sectional area of the biopsies. The model itself shows convergence of modulus and failure load, indicating that the results are mesh independent. Admittedly, linear tetrahedral elements are universally demeaned for having a constant strain, but altering the element type is a simple modification to the current method. A switch to 10-node quadratic tetrahedral elements could be done provided that more computational power is made available. (Using quadratic interpolation functions would reduce the number of elements required for convergence, but there is limited potential for improvement due to the large number of elements required merely to represent the geometry. The net effect is expected to be an increase in the total degrees of freedom.)

6 Conclusion

6.1 Bisphosphonate Treatment Recommendation Based on the Data

The objective of creating a practicable method for the finite element analysis of iliac crest biopsies at the University of Kentucky was achieved. While this research used only established techniques and pre-existing software, they were applied in a unique study of bisphosphonate's effect on bone strength. The work is novel among other finite element studies in that it exploited a pre-existing biopsy bank. It is distinctive for analyzing predominantly 3-4 mm vertical iliac biopsies. Unlike the majority of cancellous bone FEA studies, which have a pre-determined brick element size, this effort included a thorough investigation of convergence. Another departure from the norm was the use a locally-refined mesh. Using 8 micron elements for an entire biopsy is an inefficient use of resources. Small elements should only be used to capture geometry or steep stress gradients. The use of ANSYS software was also unique to some extent. ANSYS has been used in many medical studies, but there is a startling dearth of its presence in microCT-based bone research. Standard practice is to either use software developed by the microCT manufacturer, or an in-house finite element solver. Generally, both of those avenues have limited capability. ANSYS opens the floodgates to a torrent of analysis options.

The goal of assessing individual bone strength was partially realized. Biopsy failure loads were determined, but they do not directly predict bone strength. The higher-order objective of determining the safety of bisphosphonates, and thereby reducing osteoporotic fractures, was arguably a failure. There is simply too much inherent variation in the biopsies studied to observe statistically significant results with groups of 10 biopsies having an average cross sectional area of 8.18 mm^2. To elucidate the size problem, imagine what a biopsy would look like as the diameter of the core drill approached zero. At some point around one intertrabecular length, the biopsy would be nothing but a disjoined collected of bone fragments. Naturally, it is necessary to be far from this state of affairs to extract meaningful information.

The experimental data were unable to demonstrate a correlation between long-term use of bisphosphonates and decreased bone strength. However, the combination of minimal cross sectional area and low sample number resulted in an unsatisfactory statistical power (roughly 20%). Thus, no authoritative conclusions can be drawn about the safety of bisphosphonate use.

6.2 Future Work

Experiments focused on making use of the existing biopsy bank must use larger groups to decrease the probability of making a type II error. Extra samples could be obtained by easing the inclusion criteria. Using exclusively low-turnover patients and age-matching the groups severely limited the number of eligible biopsies. Using older biopsies, those removed prior to 1997, would increase the candidate pool as well. Moving away from bisphosphonate duration studies is another promising route. Experiments could be focused on fracture status, CKD patients, age, BV/TV, turnover, or any number of possible independent variables.

Aside from including more biopsies, refining the exclusion criteria may increase the usefulness of the biopsy bank. Eliminating certain biopsies *a priori* could decrease the variability, thereby giving higher statistical power for a given sample size. Reasons for rejection could be: low cross-sectional area ($<7mm^2$), extreme BV/TV, or exceptionally low connectivity.

The finite element model itself could be modified, but there is not much evidence to suggest that altering the FEM will decrease variability. Purely on a hunch, the boundary conditions could be applied to simulate compressing biopsies in frictionless form-fitting tubes. The idea is that limiting out-of-plane deflection could better model the behavior of bone in-vivo. (Assuming a cylindrical biopsy, the broken trabecular connections at the periphery of the biopsy would not be permitted to move in the radial direction.) In addition to experimenting with boundary conditions, biopsy-specific material properties from nanoindentation could easily be used in future studies. Removing any number of the previously-discussed simplifications, such as isotropy, homogeneity, or linearity could also be investigated. Going forward, the results will be improved by scanning biopsies prior to histological analysis. Using a larger diameter drill, up to the extent that no undue harm is done to the patient, would also be advantageous to the structural analysis.

Appendix A: ANSYS ICEM Log File

ANSYS ICEM CFD STL2DF 14.0 compiled on 10/4/2011
running on Windows (64 bit version)
(c) Copyright 1993 - 2011 Ansys Inc.
Part name... B02110ACR
From file C:/ICEM/tmpdomain0.uns, imported 1 surfaces, 0 curves, 0 points, 0 materials
Warning: new surfaces have 703304 triangles - by default not displaying them
Current Coordinate system is global
Please turn on the surfaces in the Entities Tree to display the surfaces. You may want to do this only for selective parts.
Done importing data.
Global Mesh Size defined
Volume Meshing Parameters defined
Writing tetin file temp_tetra.tin ...
Done saving tetin file.
Running tetra
no need to use topo thin
using user_natural_size = 0.05 for seed rather than 0.25
1 processes
about to subdivide
10,000 tetrahedra
…abbreviated…
1,000,000 tetrahedra
1308979 cells after required subdivision
slow transition
1418770 cells after balanced subdivision
computing diameters
rounding vertices to curves and surfaces
updating node connections
bilateral round to surface
updating node connections
splitting edges at surfaces
25546 edges swapped
611 edges swapped
21 edges swapped
1 edges swapped
0 edges swapped
merging mid points
merging face points
splitting extra edges
62119 split edges
0 split faces
subdividing based on split edges and faces
10 edges removed to subdivide the mesh
problem with edge 75630 75632
…abbreviated…
problem with edge 52090 183789
6 edges removed to subdivide the mesh

problem with edge 75630 75632
…abbreviated…
problem with edge 52090 183789
6 edges removed to subdivide the mesh
problem with edge 75630 75632
…abbreviated…
problem with edge 52090 183789
6 edges removed to subdivide the mesh
the mesh cannot represent the geometry near -0.866881 -0.594010 -0.626010
please check for missing prescribed points or curves
…abbreviated…
the mesh cannot represent the geometry near 0.430012 3.339527 -1.222550
please check for missing prescribed points or curves
updating node connections
splitting edges at surfaces
2200 edges swapped
40 edges swapped
1 edges swapped
0 edges swapped
merging mid points
merging face points
splitting extra edges
13763 split edges
0 split faces
subdividing based on split edges and faces
18 edges removed to subdivide the mesh
2,000,000 tetrahedra
problem with edge 260031 371914
…abbreviated…
problem with edge 358063 389609
... and 8 more messages
16 edges removed to subdivide the mesh
problem with edge 260031 371914
…abbreviated…
problem with edge 364992 381956
... and 6 more messages
16 edges removed to subdivide the mesh
problem with edge 260031 371914
…abbreviated…
problem with edge 364992 381956
... and 6 more messages
16 edges removed to subdivide the mesh
the mesh cannot represent the geometry near 0.400184 0.564274 -0.732260
please check for missing prescribed points or curves
…abbreviated…
the mesh cannot represent the geometry near 0.722511 -5.522153 -1.399328
please check for missing prescribed points or curves
... and 6 more messages

updating node connections
swapping edges
running cutter
computing opaque faces
adding missing faces
0 faces added
63 triangle boxes repaired
Adding new material point ORFN/-1 outside object at (1.45047 4.71113 0.474794)
determining material point containment
Performing flood fill
2030426 elements marked in ORFN
family B02110ACR has 275586 internal faces and 40 boundary faces
but is not marked as internal_wall
going back 41 steps on path
Adding new material point CREATED_MATERIAL_2.1 inside object (0.033588 0.802426 0.194538)
re-doing flood fill
material point CREATED_MATERIAL_2.1 can reach material point ORFN/-1
adding missing face at (x,y,z) = 0.392677, 1.38196, -1.04133
348497 elements unmarked
348497 elements remarked in part ORFN
…abbreviated…
material point CREATED_MATERIAL_2.1 can reach material point ORFN/-1
adding missing face at (x,y,z) = 0.656013, -5.99251, -0.415383
809357 elements unmarked
0 elements remarked in part ORFN
809357 elements marked in CREATED_MATERIAL_2
Adding new material point CREATED_MATERIAL_3.1 inside object (1.29881 -5.95768 -0.0928376)
2 elements marked in CREATED_MATERIAL_3
Adding new material point CREATED_MATERIAL_4.1 inside object (-0.868788 -5.36343 -0.950233)
12 elements marked in CREATED_MATERIAL_4
Adding new material point CREATED_MATERIAL_5.1 inside object (0.212061 0.24967 1.24132)
5 elements marked in CREATED_MATERIAL_5
Adding new material point CREATED_MATERIAL_6.1 inside object (-0.253181 3.67857 0.219311)
2 elements marked in CREATED_MATERIAL_6
1221069 element(s) are in part ORFN
809357 element(s) are in part CREATED_MATERIAL_2
2 element(s) are in part CREATED_MATERIAL_3
12 element(s) are in part CREATED_MATERIAL_4
5 element(s) are in part CREATED_MATERIAL_5
2 element(s) are in part CREATED_MATERIAL_6
computing bar elements
unhandled case in fix_spike_node # 401007
location: -0.554352 -1.11739 -0.755377
iteration 1: 143 points fixed**********
143 spikes fixed

disconnecting orphan cells
writing out domain file
Current Coordinate system is global
New mesh subset "added faces" created
Smoothing surface mesh...
Starting smoothing ...
smooth_elements 0.4 5 smooth TRI_3 float TETRA_4 laplace prism_warp_weight 0.5 nproc 1
number of processors = 1
smooth surface elements
initializing element ratios
beginning iteration
iteration 1 completed (Residual 1.000000)
iteration 2 completed (Residual 0.625877)
iteration 3 completed (Residual 0.256727)
iteration 4 completed (Residual 0.131888)
iteration 5 completed (Residual 0.081069)
Done smoothing.
Starting smoothing ...
smooth_elements 0.4 5 smooth TETRA_4 float PENTA_6 freeze TRI_3 prism_warp_weight 0.5 nproc 1
number of processors = 1
initializing element ratios
beginning iteration
 worst TETRA_4 4.82807e-005
smoothing 8010 TETRA_4's (up to 0.0265147)
23875 vertices selected
iteration 1 complete
 worst TETRA_4 0.00012899
…abbreviated…
smoothing 7863 TETRA_4's (up to 0.193558)
17029 vertices selected
iteration 5 complete
worst TETRA_4 0.000259095
Done smoothing.
Starting smoothing ...
smooth_elements 0.4 5 smooth TETRA_4 smooth TRI_3 float PENTA_6 prism_warp_weight 0.5 nproc 1
number of processors = 1
beginning iteration
 worst TETRA_4 0.000259095
smoothing 7854 TETRA_4's (up to 0.205407)
15754 vertices selected
iteration 1 complete
 worst TETRA_4 0.0262802
…abbreviated…
smoothing 7559 TETRA_4's (up to 0.334458)
21554 vertices selected
iteration 5 complete

worst TETRA_4 0.161777
Done smoothing.
751610 tetrahedra before
583500 elements
initializing element ratios
beginning iteration
 worst TETRA_4 0.161777
smoothing 5835 TETRA_4's (up to 0.224473)
9707 vertices selected
iteration 1 complete
 worst TETRA_4 0.161777
…abbreviated…
smoothing 5812 TETRA_4's (up to 0.341689)
3023 vertices selected
iteration 10 complete
worst TETRA_4 0.161777
520245 elements
beginning iteration
 worst TETRA_4 0.161777
smoothing 5202 TETRA_4's (up to 0.233296)
7038 vertices selected
iteration 1 complete
 worst TETRA_4 0.161777
…abbreviated…
smoothing 5192 TETRA_4's (up to 0.319001)
1961 vertices selected
iteration 10 complete
worst TETRA_4 0.161777
519257 tetrahedra after
Deleted 68190 disconnected vertices

--- Mesh Info ---
Element types :
	TETRA_4 : 519257
	TRI_3 : 246290
Element parts :
	B02110ACR : 246290
	CREATED_MATERIAL_2 : 519253
	CREATED_MATERIAL_4 : 3
	CREATED_MATERIAL_5 : 1
Total elements : 765547
Total nodes : 153980
Min : -1.1641 -6.582 -1.82698
Max : 2.04007 4.678 1.44451

Finished compute mesh

Appendix B: ANSYS.in File

The full B01.in file, with all 32,701 elements, is inconveniently lengthy to include in its entirety. Hence, the repetitious sections of the code were removed. All removed portions have the same syntax as the code immediately surrounding them.

```
/BATCH
/NOPR
/COM, ICEM-ANSYS INTERFACE - Version 13.1 -
/CONFIG,NPROC,1
/PREP7
ET,1,185,,0,,0,,0,0
/NOLIST
NBLOCK ,6,SOLID
(3i8,6e16.9)
     1       0       0 5.184175491E+00 3.446674824E+00 2.767682374E-01
     3       0       0 5.219162464E+00 3.393434763E+00 2.518546581E-01
  …abbreviated…
  17031       0       0 3.809267521E+00 1.429635644E+00 7.225907445E-01
  17035       0       0 4.698551178E+00 2.395274162E+00 2.925945222E-01
N ,R5.3,LOC,     -1
SHPP,WARN
EBLOCK ,19,SOLID
(19i10) !The following block was altered to comma-seperated to fit the page width
       2,1,0,0,0,0,0,0,8,0,27295,6494,5138,8672,8672,11797,11797,11797,11797
       2,1,0,0,0,0,0,0,8,0,27296,962,5114,11631,11631,2637,2637,2637,2637
       …abbreviated…
       2,1,0,0,0,0,0,0,8,0,59994,55,11945,7273,7273,11283,11283,11283,11283
       2,1,0,0,0,0,0,0,8,0,59995,1839,12952,819,819,33,33,33,33

-1
EN ,R5.5,ATTR,     -1
CMBLOCK,CREATED_MATERIAL_2,NODE,13322
(8i10)
       1       3       4       6       7       9      13      14
      15      17      18      21      22      23      24      25
    …abbreviated…
    16996   16997   16998   17001   17002   17003   17004   17005
    17006   17008   17009   17013   17019   17022   17023   17027
    17031   17035
/GOLIST
NSEL,ALL
ESEL,ALL
DOFSEL,ALL
CMSEL,ALL
FINISH
SAVE
/GOPR
/SOLU
```

Appendix C: ANSYS APDL Code

```
/clear                                  !start from a clean slate
*dim,biopsies,CHAR,30                   !Define the biopsy .in files to be analyzed
biopsies(1)='B01'
biopsies(2)='B02'
biopsies(3)='B03'
biopsies(4)='B04'
biopsies(5)='B05'
biopsies(6)='B06'
biopsies(7)='B07'
biopsies(8)='B08'
biopsies(9)='B09'
biopsies(10)='B10'
biopsies(11)='B11'
biopsies(12)='B12'
biopsies(13)='B13'
biopsies(14)='B14'
biopsies(15)='B15'
biopsies(16)='B16'
biopsies(17)='B17'
biopsies(18)='B18'
biopsies(19)='B19'
biopsies(20)='B20'
biopsies(21)='B21'
biopsies(22)='B22'
biopsies(23)='B23'
biopsies(24)='B24'
biopsies(25)='B25'
biopsies(26)='B26'
biopsies(27)='B27'
biopsies(28)='B28'
biopsies(29)='B29'
biopsies(30)='B30'

*dim,results,array,30,7          !Create the array to store results (rows,columns)
*DO,I,1,30                       !Do loop analyzes each biopsy
/INPUT,biopsies(I),in            !Opens an .in file instead of a database file
/prep7                           !enter the preprocessing menu; the input code redirects to
SOLU
numcmp,elem                      !renumber elements starting from 1
allsel                           !Select everything (in case a subset was selected)
*get,ymin,node,0,mnloc,y         !obtain the y axis bounding dimensions
*get,ymax,node,0,mxloc,y
BLength=ymax-ymin                !This will simplify later expressions
nsel,s,loc,y,ymin,ymin+0.05*BLength   !Select nodes in the bottom 5% of the biopsy
d,all,uy,0                       !Define uy=0 for the selected set of nodes
d,all,ux,0                       !Define ux=0 for the selected set of nodes
d,all,uz,0                       !Define uz=0 for the selected set of nodes
```

```
allsel
nsel,s,loc,y,ymax-0.05*BLength,ymax    !Select the nodes in the top 5% from the current set
d,all,uy,-.01*BLength*0.9              !Force the selected nodes to y disp. of 1 percent
compressive strain
d,all,ux,0                             !Define ux=0 for the selected set of nodes
d,all,uz,0                             !Define uz=0 for the selected set of nodes
allsel                                 !Select everything
mat,1                                  !Assign mat No.1 to subsequently defined elements
emodif,all,MAT,1                       !Modify all selected elements; set their material to #1
mp,ex,1,10000                          !Define elastic modulus of material 1 to 10000
mp,nuxy,1,.3                           !Define minor Poisson's ratio of material 1 to 0.3
mp,dens,1,0.001                        !Define mass density of material 1 to 0.001
acel,0,0,0                             !Set the acceleration in x,y,and z direction to 0.
/SOLU                                  !Enter the solution processor
eqslv,pcg                              !Select the PCG Solver
SOLVE                                  !Solve the FE problem
/POST1
*get,ElmNum,elem,0,count               !get number of elements in the selected set
etable,elem_vol,VOLU                   !Create element table with element volumes
SSUM                                   !sum all of the individual volumes
*get,totalVol,ssum,0,item,elem_vol     !get the total biopsy volume
nsel,s,loc,y,(ymax+ymin)/2,ymax        !select the nodes in the top half of the model
prrs,f                                 !print the constrained node reaction solution
FSUM                                   !Sum the node reaction solution
*get,totalFy,FSUM,0,ITEM,FY            !Get the total y direction reaction force
results(I,1)=totalFy                   !Store totalFy in the results array
allsel
!!!!!!!!!!!!!!!!!!!!!!STRAIN METHOD!!!!!!!!!!!!!!!!!!!!!!
etable,strainEQ,EPTO,EQV               !fill element table from equivalent strain
*dim,strainV,array,ElmNum,2    !create an array to hold strain and volume data
*vget,strainV(1,1),ELEM,1,ETAB,strainEQ,,,2          !put the strain in the first column
*vget,strainV(1,2),ELEM,1,ETAB,elem_vol,,,2     !put the volume in the second column
*MOPER,sort_ord,strainV,SORT,,1                  !sort the array by the strain
currentV=0                                       !create variable to track volume
*DO,J,1,ElmNum                                  !loop thorough the array
currentV=currentV+strainV(ElmNum+1-J,2)          !Sum volume at each iteration
        *IF,currentV,GT,0.018*totalVol,THEN      !stop when the 2% element is reached
         strain=strainV(ElmNum+1-J,1)
        *EXIT
        *ENDIF
*ENDDO
f_load=totalFy*0.007/strain                      !Multiply applied load by scale factor
!!!!!!!!!!!!!!!!!!!!!!!!!!!!!!!!!!!!!!!!!!!!!!!!!!!!!!!!!!!!!!!!!!!!!!!!!!!!!!!!!!

etable,stressVM,S,EQV          !Create an element table based on von Mises stress
esort,etab,stressVM,1,1        !Sort the element table by stressVM, in ascending order
*GET,max_VM,SORT,0,MAX         !Save the largest stress as a variable max_VM
results(I,2)=max_VM            !Put results into the array
```

```
results(I,3)=totalVol
results(I,4)=ElmNum
results(I,5)=blength
results(I,6)=f_load
results(I,7)=currentV
/PREP7
!nwrite,biopsies(I),txt          !Use this line to write nodes to file (optional)
*DEL,sort_ord,,NOPR              !Clear Variables before the next analysis
*DEL,totalVol,,NOPR
*DEL,strain,,NOPR
*DEL,ElmNum,,NOPR
*DEL,maxVM,,NOPR
*DEL,totalFy,,NOPR
*DEL,f_load,,NOPR
*DEL,ymin,,NOPR
*DEL,ymax,,NOPR
*DEL,Blength,,NOPR
*DEL,strainV,,NOPR
*DEL,J,,NOPR
*DEL,currentV,,NOPR
*DEL,max_VM,,NOPR
/POST1
ETABLE,ERASE
FINISH
PARSAV,all,paramet,parm          !Must save the outer DO loop variable
/clear
PARRES,new,paramet,parm          !Must restore the outer DO loop variable
*ENDDO
*cfopen,exportedData,txt         !create text file to store output array
*vwrite                          !Write a column header
('biopsy',9x,'Fy',12x,'maxVM',12x,'Volume',6x,'Elem_Num',8x,'Length',9x,'Fail',10x,'CurVol')
*vwrite,biopsies(1),results(1,1),results(1,2),results(1,3),results(1,4),results(1,5),results(1,6),re
sults(1,7)                       !Write data to the opened text file
(A8,2X,E13.5,2X,E13.5,2X,E13.5,2X,E13.5,2X,E13.5,2X,E13.5,2X,E13.5)
```

Appendix D: MATLAB Code

```
%Cross Sectional Area Finder
%By Jonathan Ward/Lucas Wilkerson
%Description: Finds the cross sectional area from the node coordinates of a
%mesh using the Convex Hull algorithm. Data is exported to an excel file.
%Variables Used:
%files     nx1 cell array    string variables of biopsy names
%num       1                 number of biopsies
%f         nx6 to nx10       biopsy names in character matrix form
%data      nx4 double        node numbers and corresponding coordinates
%x         nx1 double        x coordinates of the nodes
%z         nx1 double        z coordinates of the nodes
%K         35x1 double       Convex Hull Index
%A         1                 cross sectional area
%s         1                 Either 1 (xlswrite worked) or 0 (failed)
close all
clear all
clc
files=importdata('biopsy_list_txt.txt');
f=char(files);
for t=1:30
   data=importdata(char(files(t)));
   x=data(:,2);
   z=data(:,4);
   [K,A] = convhull(x,z);
   files{t,2}= A;
   clear x
   clear z
   clear data
   clear A
end
s=xlswrite('area_output.xls',files)
```

Appendix E: Biopsy Images

Figure E-1: Biopsies B01 through B08.

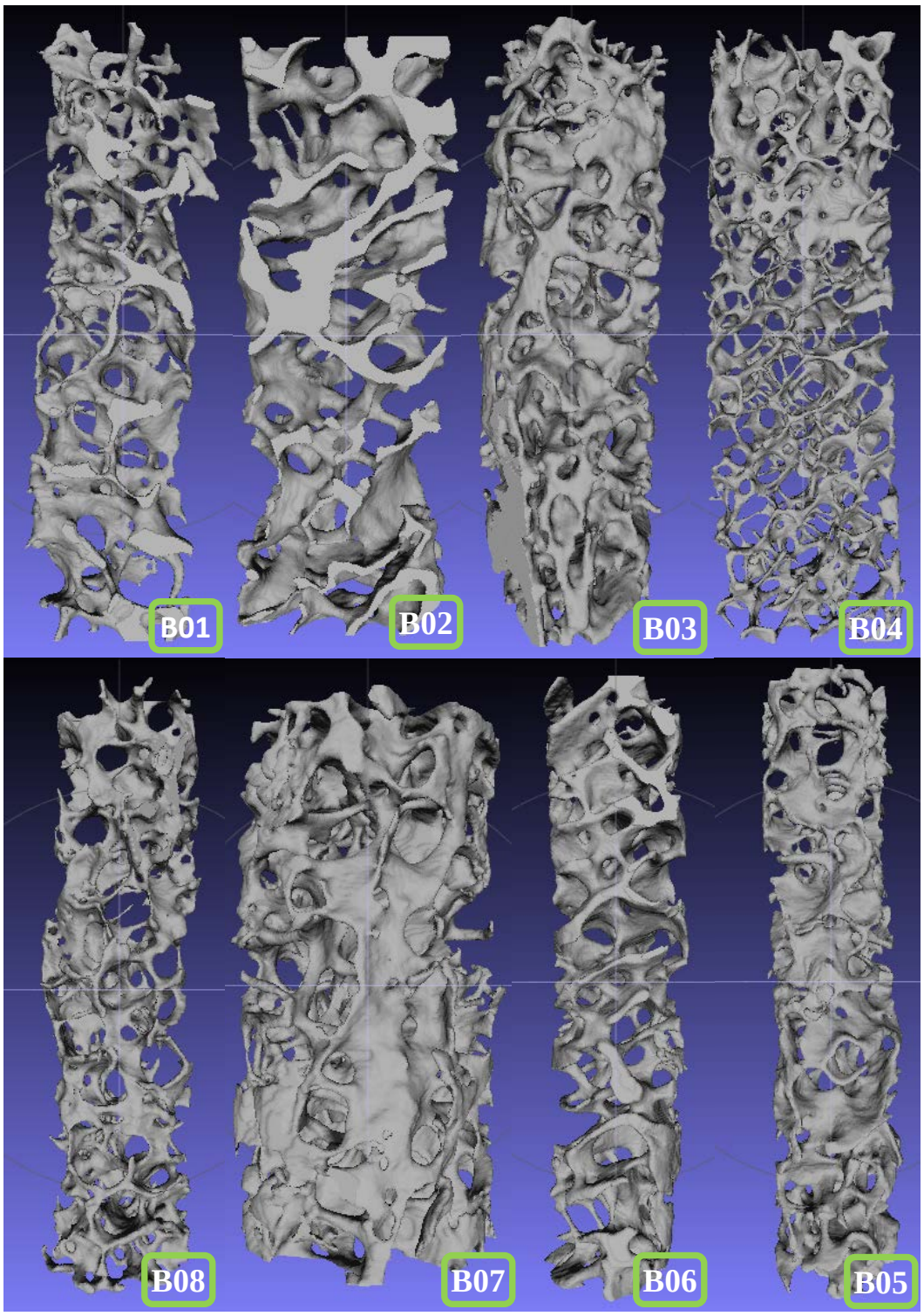

Figure E-2: Biopsies B09 through B14.

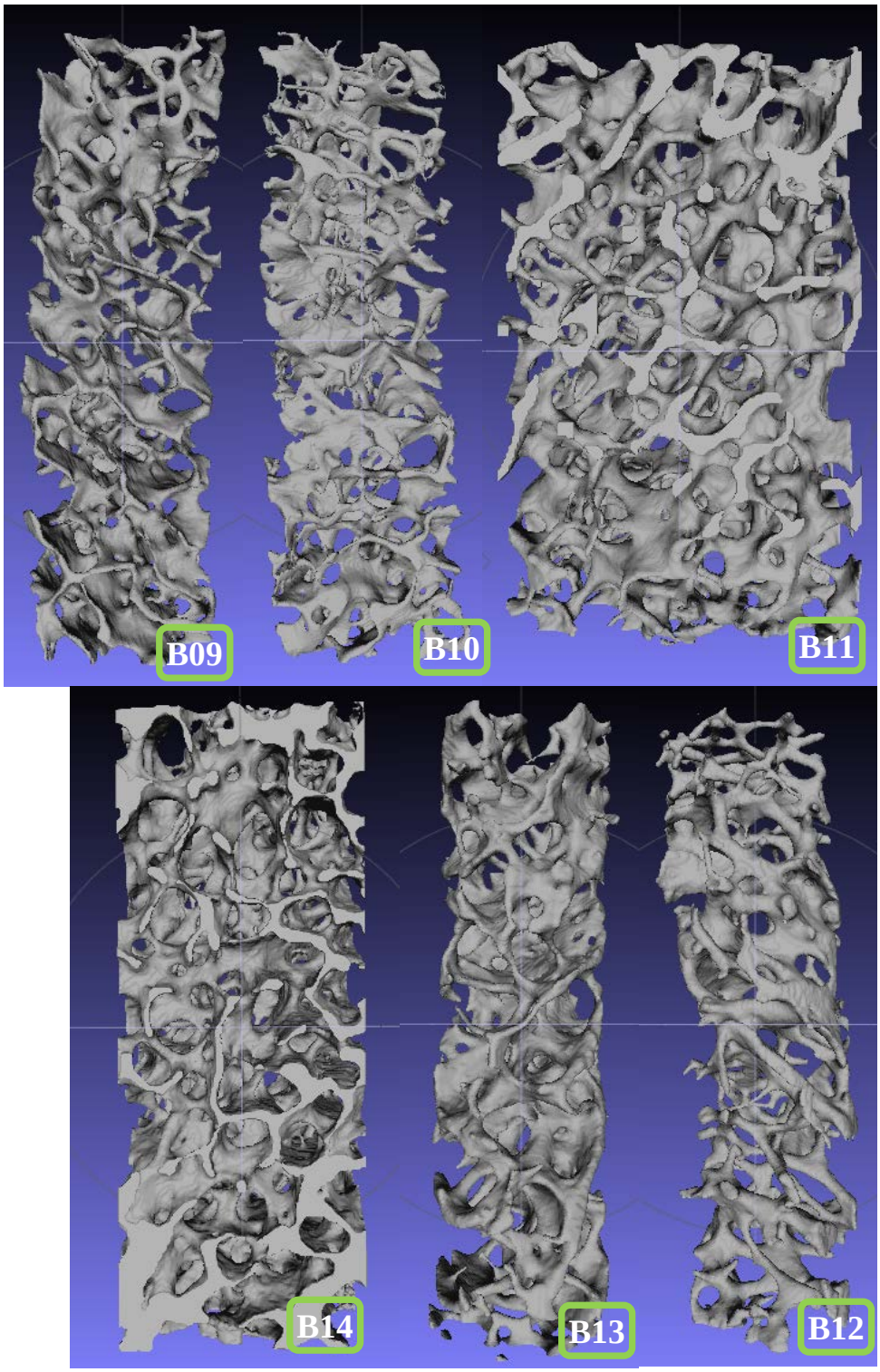

Figure E-3: Biopsies B15 through B20

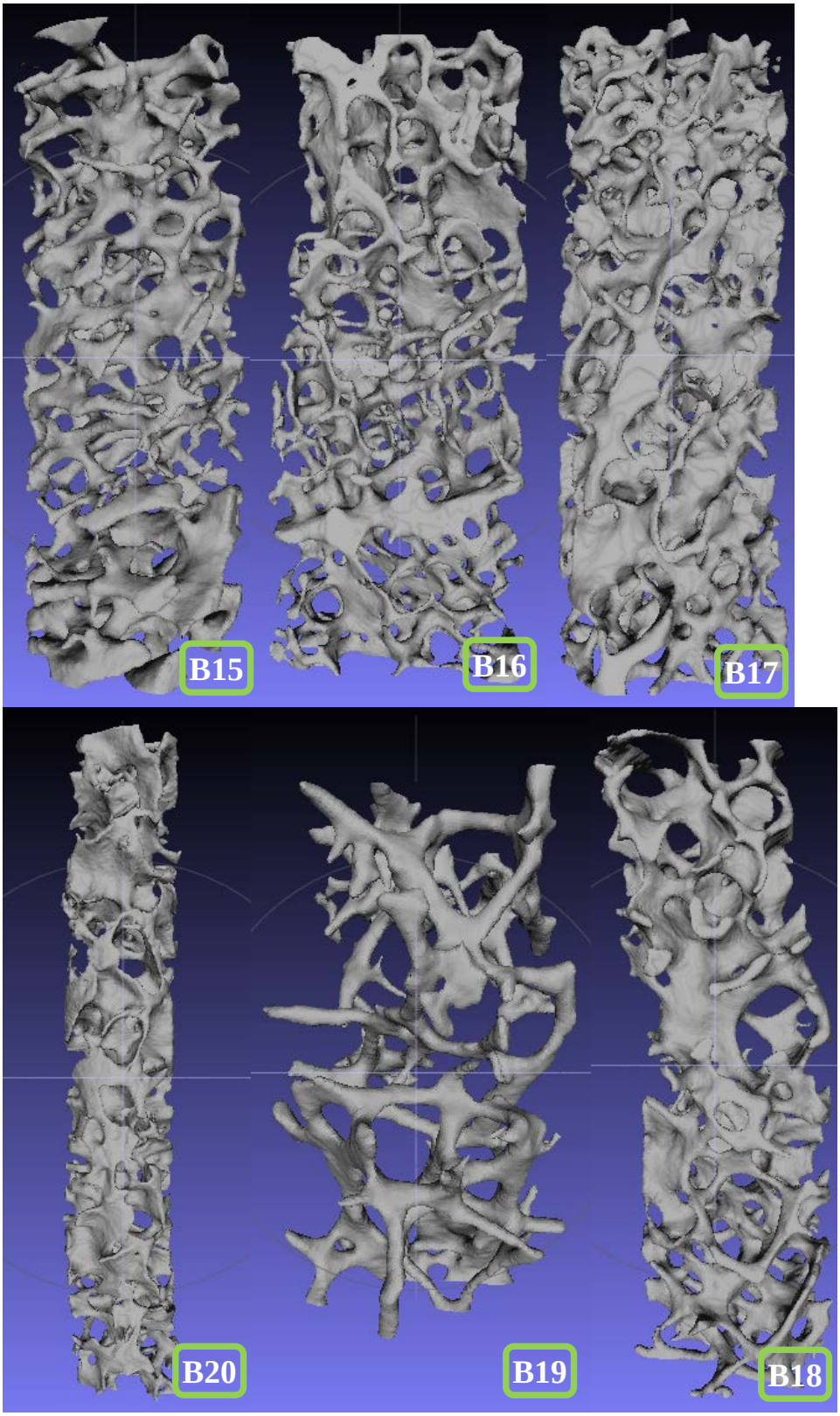

Figure E-4: Biopsies B21 through B26.

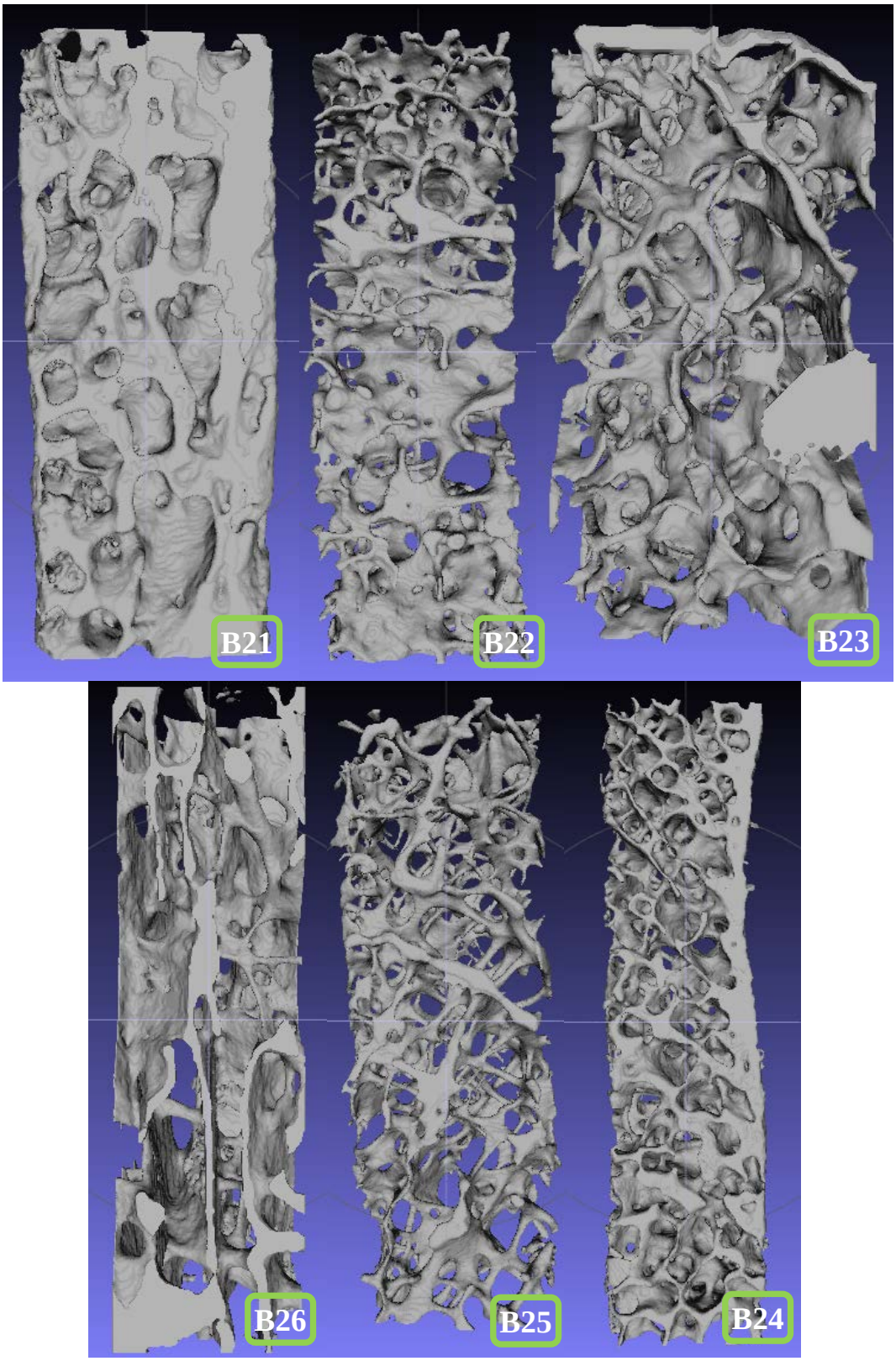

Figure E-5: Biopsies B27 through B30.

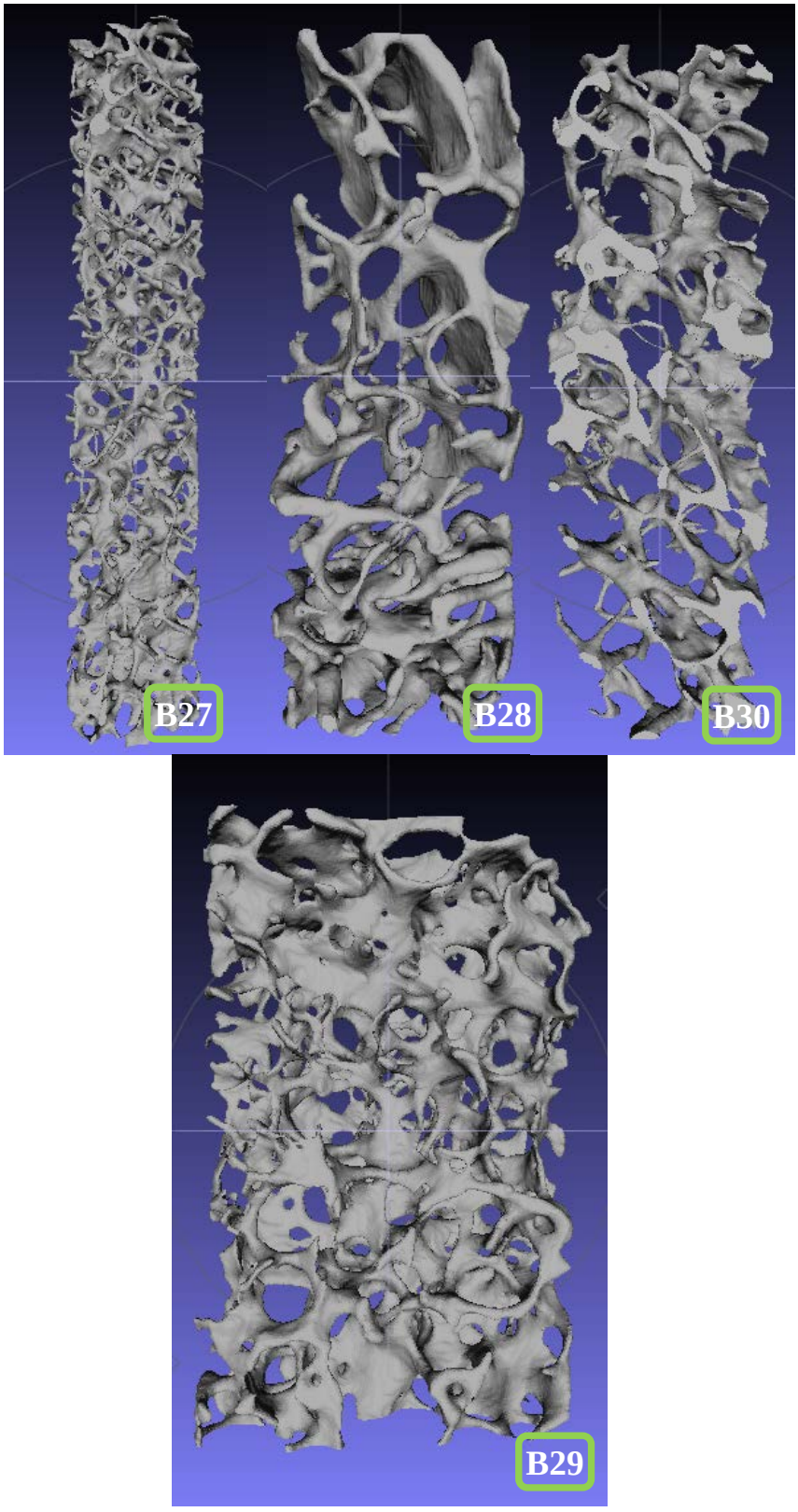

Appendix F: Biopsy Patient Information

Table F-1: Patient Information (Part 1)

biopsy #	UK (y/n)	age	Group	duration yrs	bisph. Name	bisph. Dose (mg)	dose freq.	ovariectomy	HRT	family history of osteoporosis	ethanol abuse	exercise
B28	n	67	0									
B04		53	0						1			
B29	y	61	0					0	0		0	0
B16	y	42	0					1	1		0	
B10	y	72	0					0	1			
B26	n	57	0					0	0			
B25	y	53	0					0	1	0	0	
B23	n	72	0					1	1		0	0
B11	n	41	0					1	0		0	0
B14	n	53	0					1				
B22	y	60	1	2	FOSAMAX			0	0	0	0	0
B24	y	54	1	3	FOSAMAX	70	weekly	1	1	1	1	0
B21	y	59	1	4	FOSAMAX	70	weekly	0	1	0	0	0
B30	y	57	1	1.25	ACTONEL	35	weekly		1		0	
B07	y	58	1	2	FOS., ACT.	70	weekly	0	0	1	1	1
B19	y	63	1	1	BONIVA	150	monthly	0	0		0	0
B20	y	60	1	4	FOSAMAX	70	weekly	0				
B06	y	59	1	3	FOSAMAX	70	weekly	0	1		0	0
B13	y	57	1	1.5	FOSAMAX			0	1	0	1	0
B15	y	55	1	2	FOS., BON., REC.			0	1	0	1	1
B02	y	54	2	7	FOS., ACT.	35	weekly	0	1	0	0	1
B09	y	57	2	8	FOS., ACT.	70	weekly	0	0			
B17	y	58	2	7	FOSAMAX	70	weekly	0	1		0	0
B05	y	54	2	5	FOSAMAX	70	weekly	0	0			
B01	y	64	2	9	FOSAMAX	70	weekly	0	0	0	0	0
B03	n	61	2	5.5	BONIVA	150	monthly	0	1	0	0	
B08	y	63	2	5	FOSAMAX	70	weekly	0	1	0	1	1
B12		65	2	13	FOSAMAX			1	1	0	1	1
B18	y	63	2	12	ACTONEL			0	1	0	0	1
B27	y	67	2	6	FOSAMAX	70	weekly	0	1	0	1	0

Table F-2: Patient Information (Part 2)

biopsy #	bmdspine (t-score)	bmdhip (t-score)	serum calcium	serum phosphate	serum creatinine	alkaline phosphate	bone specific alkaline phsophate	vitd25	vitd125	pth	cap	bgp or osteocalin	treated w/ calcium
B28													
B04			9.7	2.6	0.9			8	32	84		7.6	
B29	-2.6		9.2	3.5	0.7	68				55		17.5	0
B16	-1.4	-2.1	8.7	3.6	0.9	68		25	67	47		6.5	1
B10			9.3	3.5	0.6	47		18	42	25		9.4	1
B26			9.6			110			35.3	30			1
B25	-2		9.1	0.7	3.9		28.9		32				1
B23			9	2.9	2	45		24		56			0
B11			9.6	4.7	0.7	37	25	64	53				0
B14			8.9	4		138		8		5			
B22			9.6	3	0.7	66		53	33	49		4.0	1
B24	-2.42		9.4			46							1
B21	-1	-0.9	9.2	3.9	0.9	87				26			1
B30	-2.9	-1.7	9.1	4.3	0.9	42	22.6	65	63	17		1.7	1
B07	-2.2			3.9	0.8	58		42			34.3	2.6	0
B19	-3	-1.2					10	39			19	19	0
B20	-3.5	-0.9		4.9	1		9	29			13	13	0
B06			9.3	4.3	0.74					22			0
B13	-2.9	-2.3					15.7	41			19	15	1
B15		-1.88			0.65		11.9	36			21	15	1
B02	-2.8	-2.11	9.2	2.8	0.8		10.2	102	25	9		13.7	1
B09	-2.5	-2.5		4.9			10.4	28			22	19	0
B17	-2.2	-2.5	9.4			78		42		47		15	1
B05			10.1	3.7	0.74		21.7	45		33	8	22	0
B01	-3.1	-2.6	9.4	3.6	0.77	62	11.1	34	58		28		0
B03	-0.6		9.1	3.7	1.04			51					1
B08	-1.19	-2.6	9.6	3.6	0.77			52	104		25	14	1
B12			9.7	3.7	0.95	37	6.8	45		27			1
B18	-1.47	-2.01	9.2	4.1	0.77	56	8.3	106		34		9	1
B27	-0.4	-2.9	8.9	3.2	0.87		5.2	57		29			1

Table F-3: Patient Information (Part 3)

biopsy #	bone pain	fracture	mult. fractures (y/n)	fracture trauma	mineralization defect	height	weight	notes
B28		1	y		0			
B04		1						
B29	1	0			1			
B16	0	1	y		1		136	
B10	0	1			1			
B26		1			0			
B25	0	0			0	63	96	
B23	0	0			1	61	154	barrett's esoph.
B11	0	0			1			
B14								
B22	0	0			0			
B24	0	0			0	65	136	
B21	0	1	y	low	0	65	169	
B30	0	1			0			
B07	0	0			0			MS
B19		1		high	1		191	hyperlipidemia
B20	1				1		130	
B06	1	1	y		1		186	CKD III
B13	0	1			1	59	123	OI, RA
B15	1	1	y		1		137	Breast CA
B02	0	0			1	60	125	hypothyroid
B09	0	0			1		139	
B17	0	1		high	1	63	160	
B05	0	0			1		129	OI
B01	0	1	y		1	62	111	
B03	1	1	y	lo./hi.	1	63	217	arthritis
B08	0	0			1	64	106	
B12	0	0			1	62	167	
B18	0	1			1	62	165	OA
B27	0	1		high	1	63	118	

Appendix G: Raw Data

Table G-1: Coarse Mesh Output Data

biopsy	F_y [N]	σ_{max} [MPa]	BV [mm^3]	Elem #	Length [mm]	F_{ult} [N]	Area [mm^2]
B01	6.00	720	5.08	32701	9.66	4.72	4.71
B02	11.33	425	5.74	38375	7.83	8.23	2.91
B03	55.32	870	16.59	67081	9.00	28.26	6.93
B04	9.57	622	12.27	25258	12.84	7.20	8.28
B05	14.85	659	13.06	34873	12.89	11.03	7.07
B06	17.83	606	15.82	29106	12.36	12.88	6.19
B07	40.22	1001	15.23	77787	7.51	24.13	13.26
B08	11.46	777	9.30	43647	11.26	8.16	6.81
B09	7.99	917	7.56	48887	9.62	6.81	5.63
B10	6.36	471	11.31	39221	13.09	6.16	9.47
B11	53.29	1249	14.38	133190	6.94	30.89	14.44
B12	3.86	516	9.35	28723	9.95	4.80	8.01
B13	24.56	899	14.67	47907	9.37	15.54	6.76
B14	126.54	1384	45.74	109320	11.42	65.85	15.16
B15	3.89	404	5.51	46740	7.23	4.16	6.37
B16	17.60	1286	10.16	43095	9.86	11.03	8.17
B17	16.52	1004	6.55	67154	7.49	10.25	5.92
B18	13.43	426	7.61	33474	9.12	9.48	6.56
B19	0.15	85	1.70	27451	4.56	0.53	6.87
B20	32.61	829	23.11	31439	16.21	18.38	7.44
B21	255.10	746	41.33	92402	9.73	110.53	8.98
B22	20.62	680	15.03	45690	12.09	13.61	9.69
B23	27.42	701	11.36	102080	6.72	18.49	12.19
B24	146.59	1110	48.88	66551	15.46	66.63	9.38
B25	8.20	1026	12.54	61843	10.97	7.51	11.28
B26	136.79	928	30.72	68432	12.50	62.20	12.74
B27	4.95	1964	7.57	39351	13.87	4.25	6.61
B28	1.87	238	6.50	42974	7.67	3.02	3.86
B29	15.22	694	5.89	69099	6.16	9.99	8.49
B30	5.06	413	9.09	32076	12.12	4.94	5.33

Table G-2: Coarse Mesh Derived Data

biopsy	TV [mm^3]	BV/TV	P_y [MPa]	SAR	E [MPa]	E_{eff} [MPa]	P_{fail} [MPa]
B01	45.53	0.112	1.27	566.0	127.2	1141.1	1.00
B02	22.78	0.252	3.90	109.0	389.7	1546.0	2.83
B03	62.37	0.266	7.98	109.0	798.3	3000.4	4.08
B04	106.30	0.115	1.16	538.4	115.5	1001.1	0.87
B05	91.17	0.143	2.10	313.8	210.0	1466.1	1.56
B06	76.52	0.207	2.88	210.6	287.9	1392.9	2.08
B07	99.60	0.153	3.03	330.1	303.2	1982.6	1.82
B08	76.70	0.121	1.68	461.7	168.3	1388.2	1.20
B09	54.15	0.140	1.42	646.1	142.0	1017.1	1.21
B10	123.95	0.091	0.67	701.1	67.1	735.9	0.65
B11	100.24	0.143	3.69	338.5	369.0	2571.9	2.14
B12	79.66	0.117	0.48	1071.0	48.2	410.5	0.60
B13	63.31	0.232	3.63	247.4	363.5	1569.0	2.30
B14	173.21	0.264	8.35	165.8	834.6	3160.7	4.34
B15	46.05	0.120	0.61	660.8	61.1	511.3	0.65
B16	80.57	0.126	2.15	597.3	215.4	1708.8	1.35
B17	44.35	0.148	2.79	360.0	278.9	1889.3	1.73
B18	59.80	0.127	2.05	208.2	204.8	1609.3	1.45
B19	31.34	0.054	0.02	3848.8	2.2	40.7	0.08
B20	120.67	0.192	4.38	189.2	438.1	2287.2	2.47
B21	87.40	0.473	28.40	26.3	2839.8	6005.6	12.30
B22	117.12	0.128	2.13	319.3	212.9	1659.1	1.41
B23	81.94	0.139	2.25	311.7	224.9	1621.9	1.52
B24	145.00	0.337	15.63	71.0	1563.0	4636.1	7.10
B25	123.76	0.101	0.73	1412.7	72.7	717.2	0.67
B26	159.21	0.193	10.74	86.4	1074.1	5567.4	4.88
B27	91.65	0.083	0.75	2624.3	74.8	906.0	0.64
B28	29.62	0.219	0.48	492.0	48.5	220.8	0.78
B29	52.33	0.113	1.79	387.5	179.1	1592.1	1.18
B30	64.62	0.141	0.95	435.5	94.8	673.7	0.93

Table G-3: Fine Mesh Output Data

biopsy	F_y [N]	σ_{max} [MPa]	BV [mm^3]	Elem #	Length [mm]	F_{ult} [N]	Area [mm^2]
B01	5.27	937	5.58	301320	9.66	4.57	4.71
B02	8.58	466	5.97	239610	7.83	7.10	2.91
B03	46.77	1295	17.09	647250	9.00	25.86	6.93
B04	6.65	1101	14.30	745960	12.84	6.59	8.28
B05	11.38	1147	14.30	609380	12.89	9.42	7.07
B06	14.08	610	16.93	461860	12.36	11.43	6.19
B07	36.24	1177	16.18	699340	7.51	23.43	13.26
B08	9.49	2218	10.18	519250	11.26	7.63	6.81
B09	5.54	869	8.09	404590	9.62	5.71	5.63
B10	5.01	1533	12.90	590000	13.09	5.76	9.47
B11	49.86	890	15.48	899670	6.94	30.44	14.44
B12	2.64	1048	10.53	418740	9.95	4.11	8.01
B13	21.48	787	15.25	447290	9.37	14.68	6.76
B14	106.68	1697	47.15	941290	11.43	59.95	15.16
B15	3.26	414	6.09	367380	7.23	4.03	6.37
B16	14.95	1928	11.35	562320	9.86	10.68	8.17
B17	14.72	2072	7.00	444060	7.49	9.87	5.92
B18	11.15	621	8.23	346970	9.12	8.84	6.56
B19	0.12	104	1.88	130930	4.56	0.48	6.87
B20	23.63	1974	24.77	723250	16.21	15.86	7.44
B21	219.65	2523	41.41	1140200	9.73	99.50	8.98
B22	17.10	1228	16.49	720860	12.09	13.00	9.69
B23	23.63	868	12.02	610270	6.72	17.42	12.19
B24	120.42	1586	49.77	860050	15.46	58.41	9.38
B25	6.94	857	13.99	710670	10.97	7.32	11.28
B26	129.05	1052	31.93	704390	12.50	60.44	12.74
B27	4.54	1954	9.07	593940	13.87	4.55	6.61
B28	1.38	264	6.93	284470	7.67	2.68	3.86
B29	15.17	1133	6.43	421800	6.16	10.36	8.49
B30	4.05	1121	10.03	431100	12.12	4.65	5.33

Table G-4: Fine Mesh Derived Data

biopsy	TV [mm^3]	BV/TV	P_y [MPa]	SAR	E [MPa]	E_{eff} [MPa]	P_{fail} [MPa]
B01	45.53	0.123	1.12	838.9	111.8	911.3	0.97
B02	22.78	0.262	2.95	158.1	294.9	1125.8	2.44
B03	62.37	0.274	6.75	191.8	675.0	2463.4	3.73
B04	106.30	0.135	0.80	1371.2	80.3	596.7	0.80
B05	91.17	0.157	1.61	713.0	160.8	1025.1	1.33
B06	76.52	0.221	2.27	268.2	227.5	1028.2	1.85
B07	99.61	0.162	2.73	430.8	273.2	1681.8	1.77
B08	76.70	0.133	1.39	1592.1	139.3	1050.0	1.12
B09	54.15	0.149	0.98	882.6	98.5	659.5	1.01
B10	123.95	0.104	0.53	2900.3	52.9	507.8	0.61
B11	100.22	0.154	3.45	257.9	345.3	2236.2	2.11
B12	79.66	0.132	0.33	3173.2	33.0	249.9	0.51
B13	63.30	0.241	3.18	247.5	317.9	1319.7	2.17
B14	173.23	0.272	7.04	241.1	703.6	2584.9	3.95
B15	46.05	0.132	0.51	808.1	51.2	386.8	0.63
B16	80.57	0.141	1.83	1053.8	183.0	1298.9	1.31
B17	44.35	0.158	2.49	833.2	248.6	1574.9	1.67
B18	59.80	0.138	1.70	365.1	170.1	1236.4	1.35
B19	31.34	0.060	0.02	6148.7	1.7	28.1	0.07
B20	120.67	0.205	3.17	622.1	317.3	1546.1	2.13
B21	87.41	0.474	24.45	103.2	2445.2	5161.0	11.08
B22	117.12	0.141	1.76	695.8	176.5	1253.8	1.34
B23	81.94	0.147	1.94	447.8	193.8	1321.3	1.43
B24	145.00	0.343	12.84	123.5	1283.9	3740.6	6.23
B25	123.76	0.113	0.62	1392.4	61.5	544.1	0.65
B26	159.22	0.201	10.13	103.8	1013.3	5053.4	4.75
B27	91.65	0.099	0.69	2846.7	68.6	693.6	0.69
B28	29.62	0.234	0.36	738.4	35.8	152.9	0.69
B29	52.33	0.123	1.79	634.7	178.6	1453.2	1.22
B30	64.62	0.155	0.76	1475.1	76.0	490.0	0.87

Table G-5: Fixed-Length Output Data

biopsy	F_y [N]	σ_{max} [MPa]	BV [mm^3]	Elem #	Length [mm]	F_{ult} [N]	Area [mm^2]
B01	7.49	393	2.27	122990	4.115	5.31	4.71
B02	8.94	436	2.87	120420	4.124	7.10	2.91
B03	52.48	929	7.49	275050	4.188	27.77	6.93
B04	6.90	779	3.81	232990	4.143	6.37	8.28
B05	19.11	714	4.33	168960	4.127	11.80	7.07
B06	16.67	497	5.07	148510	4.199	11.78	6.19
B07	35.59	1246	6.98	338210	4.136	21.38	13.26
B08	12.13	1329	3.18	160630	4.130	8.50	6.81
B09	4.83	385	3.57	175830	4.115	5.32	5.63
B10	8.40	365	4.24	182200	4.141	7.42	9.47
B11	56.64	581	8.58	498010	4.120	32.49	14.44
B12	7.68	2280	4.61	166130	4.212	7.64	8.01
B13	62.16	729	7.72	191180	4.182	30.24	6.76
B14	120.25	922	16.23	462960	4.167	65.86	15.16
B15	4.13	334	3.07	209240	4.120	4.36	6.37
B16	16.35	2225	4.48	232940	4.159	10.61	8.17
B17	13.24	1366	3.36	201060	4.114	8.60	5.92
B18	13.86	399	3.59	142030	4.147	9.63	6.56
B19	0.11	101	1.61	113310	4.118	0.46	6.87
B20	36.28	805	7.12	179720	4.198	20.13	7.44
B21	218.34	1980	16.07	464620	4.203	103.33	8.98
B22	26.94	437	5.80	230280	4.112	16.77	9.69
B23	26.08	4948	6.65	329370	4.148	18.17	12.19
B24	180.69	1370	14.82	328700	4.211	92.50	9.38
B25	15.68	859	5.66	279430	4.139	11.64	11.28
B26	152.17	889	9.82	206020	4.198	71.39	12.74
B27	7.03	1137	2.54	175650	4.096	5.49	6.61
B28	1.66	319	2.83	121990	4.134	2.58	3.86
B29	14.08	900	3.80	258820	4.104	9.39	8.49
B30	9.35	1699	3.83	167040	4.127	7.79	5.33

Table G-6: Fixed-Length Derived Data

biopsy	TV [mm^3]	BV/TV	P_y [MPa]	SAR	E [MPa]	E_{eff} [MPa]	P_{fail} [MPa]
B01	19.39	0.117	1.59	247.5	159.0	1355.3	1.13
B02	12.00	0.239	3.08	141.9	307.5	1285.2	2.44
B03	29.02	0.258	7.57	122.7	757.3	2934.0	4.01
B04	34.30	0.111	0.83	934.7	83.4	750.8	0.77
B05	29.19	0.148	2.70	264.2	270.1	1819.3	1.67
B06	25.99	0.195	2.69	184.4	269.2	1379.3	1.90
B07	54.86	0.127	2.68	464.2	268.3	2109.4	1.61
B08	28.13	0.113	1.78	746.1	178.1	1573.8	1.25
B09	23.16	0.154	0.86	448.0	85.9	557.0	0.94
B10	39.21	0.108	0.89	411.7	88.8	820.4	0.78
B11	59.48	0.144	3.92	148.2	392.3	2719.8	2.25
B12	33.72	0.137	0.96	2376.3	96.0	702.2	0.95
B13	28.26	0.273	9.20	79.3	920.0	3366.6	4.48
B14	63.17	0.257	7.93	116.3	793.1	3087.2	4.34
B15	26.24	0.117	0.65	515.0	64.9	554.1	0.69
B16	33.98	0.132	2.00	1112.4	200.0	1517.4	1.30
B17	24.36	0.138	2.24	611.1	223.6	1620.3	1.45
B18	27.19	0.132	2.11	188.8	211.4	1599.6	1.47
B19	28.30	0.057	0.02	6208.4	1.6	28.5	0.07
B20	31.25	0.228	4.87	165.2	487.3	2137.5	2.70
B21	37.76	0.426	24.31	81.5	2430.6	5711.5	11.50
B22	39.83	0.146	2.78	157.2	278.1	1909.3	1.73
B23	50.58	0.131	2.14	2313.9	213.8	1627.6	1.49
B24	39.50	0.375	19.27	71.1	1926.5	5132.9	9.86
B25	46.70	0.121	1.39	618.4	139.0	1146.9	1.03
B26	53.47	0.184	11.95	74.4	1194.8	6507.6	5.61
B27	27.07	0.094	1.06	1068.8	106.3	1134.2	0.83
B28	15.97	0.177	0.43	744.2	42.9	241.6	0.67
B29	34.86	0.109	1.66	543.3	165.7	1521.3	1.11
B30	22.01	0.174	1.75	968.2	175.4	1009.2	1.46

References

1. "Debunking the Myths." *Home*. National Osteoporosis Foundation, n.d. Web. 22 Oct. 2012. <http://www.nof.org/articles/4>.
2. Burge, Russel, Bess Dawson-Hughes, Daniel H. Solomon, John B. Wong, Alison King, and Anna Tosteson. "Incidence and Economic Burden of Osteoporosis-Related Fractures in the United States, 2005-2025." *Journal of Bone and Mineral Research* 22.3 (2007): 465-75. Print.
3. Odden, Michelle C., Pamela G. Coxson, Andrew Moran, James M. Lightwood, Lee Goldman, and Kirsten Bibbins-Domingo. "The Impact of the Aging Population on Coronary Heart Disease in the United States." *The American Journal of Medicine*124.9 (2011): 827-33.e5. Print.
4. Benton, Melissa, and Andrea White. "Osteoporosis: Recommendations for Resistance Exercise and Supplementation With Calcium and Vitamin D to Promote Bone Health."*Journal of Community Health Nursing* 23.4 (2006): 201-11. Print
5. Smith, R. "Exercise and Osteoporosis." *Bmj* 290.6476 (1985): 1163-164. Print.
6. O'Brien, M. "Osteoporosis and Exercise." *British Journal of Sports Medicine* 30.3 (1996): 191. Print.
7. Mayo Clinic Staff. "Osteoporosis Treatment: Medications Can Help." *Mayo Clinic*. Mayo Foundation for Medical Education and Research, 23 Aug. 2011. Web. 22 Oct. 2012. <http://www.mayoclinic.com/health/osteoporosis-treatment/WO00127>.
8. American Dental Association Counsel on Scientific Affairs. "Dental Management of Patients Receiving Oral Bisphosphonate Therapy." *Journal of the American Dental Assocation* 137.8 (2006): 1144-150. *JADA*. American Dental Assocation, 2006. Web. 19 Aug. 2012. <http://jada.ada.org/cgi/content/full/137/8/1144>.
9. Cagnetta, V., and V. Patella. "The Role of the Immune System in the Physiopathology of Osteoporosis." *Clinical Cases in Mineral and Bone Metabolism* 9(2) (2012): 85-88. Clinical Cases in Mineral and Bone Metabolism, May-June 2012. Web. 23 Oct. 2012. <http://www.ncbi.nlm.nih.gov/pmc/issues/215517/>.
10. Rivadeneira, Fernando. "Hunting Osteoporosis Susceptibility Genes: Bigger Is Better but Diverse Is Also Welcome." Endocrine, 22 Sept. 2012. Web. 23 Oct. 2012. http://www.springerlink.com/content/591134722m17uk00/fulltext.pdf
11. Merom, D., and V. Pye. "Prevalence and Correlates of Participation in Fall Prevention Exercise/physical Activity by Older Adults." *Preventive Medicine* (2012): [Epub ahead of print] Web. 23 Oct. 2012. <http://www.sciencedirect.com/science/article/pii/S0091743512004756>.
12. Ott, S. M. "Long-Term Safety of Bisphosphonates." *Journal of Clinical Endocrinology & Metabolism* 90.3 (2004): 1897-899. Print.
13. Day, J. "Bisphosphonate Treatment Affects Trabecular Bone Apparent Modulus through Micro-architecture Rather than Matrix Properties." *Journal of Orthopaedic Research* 22.3 (2004): 465-71. Print.
14. Tam, Cherk S., and William Anderson. "Tetracycline Labeling of Bone in Vivo." *Calcified Tissue International* 30.1 (1980): 121-25. Print.
15. Malluche, Hartmut H., Hanna Mawad, and Marie-Claude Monier-Faugere. "Bone Biopsy in Patients with Osteoporosis." *Current Osteoporosis Reports* 5.4 (2007): 146-52. Print.
16. Timoshenko, Stephan P. *History of Strength of Materials*. New York: McGraw-Hill, 1953. Print.

17. Johnell, O. "Advances in Osteoporosis : Better Identification of Risk Factors Can Reduce Morbidity and Mortality." *Journal of Internal Medicine* (1996): 239+. Print.
18. Johnell, O., J. A. Kanis, A. Oden, I. Sernbo, I. Redlund-Johnell, C. Petterson, C. De Laet, and B. Jonsson. "Mortality after Osteoporotic Fractures." *Osteoporosis International*15.1 (2004): 38-42. Print.
19. Bolland, M. J., and A. Grey. "The Effect of Treatments for Osteoporosis on Mortality."*Osteoporos Int* (2012) [published online ahead of print] *Http://www.springerlink.com/content/9260nr0445032048/fulltext.pdf*. 18 Oct. 2012. Web. 24 Oct. 2012.
20. Compston, Juliet. "Osteoporosis: Social and Economic Impact." *Radiologic Clinics of North America* 48.3 (2010): 477-82. Print.
21. Black, Dennis M., Steven R. Cummings, Harry K. Genant, Michael C. Nevitt, Lisa Palermo, and Warren Browner. "Axial and Appendicular Bone Density Predict Fractures in Older Women." Journal of Bone and Mineral Research 7.6 (1992): 633-38. Print.
22. Bone, Henry G., Arthur C. Santora, Arghya Chattopadhyay, and Uri Liberman. "Are We Treating Women With Postmenopausal Osteoporosis for Their Low BMD or High Fracture Risk?" *Journal of Bone and Mineral Research* 20.11 (2005): 2064-065. Print.
23. Geusens, Piet, Tineke Van Geel, Kirsten Huntjens, Sven Van Helden, Sandrine Bours, and Joop Van Den Bergh. "Clinical Fractures beyond Low BMD." *International Journal of Clinical Rheumatology* 6.4 (2011): 411-21. Print.
24. Heymsfield, Steven. *Human Body Composition*. Champaign, IL: Human Kinetics, 2005. Print.
25. Whiting, William Charles., and Stuart Rugg. *Dynatomy: Dynamic Human Anatomy*. Vol. 10. Champaign, IL: Human Kinetics, 2006. Print.
26. Hannah, K.M., C.D.L. Thomas, J.G. Clement, F. De Carlo, and A.G. Peele. "Bimodal Distribution of Osteocyte Lacunar Size in the Human Femoral Cortex as Revealed by Micro-CT." *Bone* 47.5 (2010): 866-71. Print.
27. Pazzaglia, Ugo E., and Terenzio Congiu. "The Cast Imaging of the Osteon Lacunar-canalicular System and the Implications with Functional Models of Intracanalicular Flow."*Journal of Anatomy* (2012): [Epub ahead of print] Web. 3 Nov. 2012. <http://onlinelibrary.wiley.com/doi/10.1111/joa.12004/abstract>.
28. Teraoka, K., A. Ito, K. Maekawa, K. Onuma, T. Tateishi, and S. Tsutsumi. "Mechanical Properties of Hydroxyapatite and OH-carbonated Hydroxyapatite Single Crystals."*Journal of Dental Research* 77.7 (1998): 1560-568. Print.
29. Rho, Jae Young, Richard B. Ashman, and Charles H. Turner. "Young's Modulus of Trabecular and Cortical Bone Material: Ultrasonic and Microtensile Measurements."*Journal of Biomechanics* 26.2 (1993): 111-19. Print.
30. Krum, S. A., and M. Brown. "Unraveling Estrogen Action in Osteoporosis." *Cell Cycle* 7.10 (2008): 1348-352. Print.
31. Mariotti, Angelo. "Bisphosphonates and Osteonecrosis of the Jaws." *Journal of Dental Education* 72.8 (2008): 919-29. Print.
32. Neviaser, Andrew S., Joseph M. Lane, Brett A. Lenart, Folorunsho Edobor-Osula, and Dean G. Lorich. "Low-Energy Femoral Shaft Fractures Associated With Alendronate Use."*Journal of Orthopaedic Trauma* 22.5 (2008): 346-50. Print.
33. Van Der Meulen, M. C., and A. L. Boskey. "Atypical Subtrochanteric Femoral Shaft Fractures: Role for Mechanics and Bone Quality." *Arthritis Research Therapy* 14.4

(2012): 220. *PubMed.gov*. NIH, 20 Aug. 2012. Web. 4 Sept. 2012. <http://www.ncbi.nlm.nih.gov/pubmed/22958475>.
34. Gupta, K. K., and J. L. Meek. "A Brief History of the Beginning of The Finite Element Method." *International Journal for Numerical Methods in Engineering* 39.22 (1996): 3761-774. Print.
35. Mackie, R. I. "Object Oriented Programming of the Finite Element Method." *International Journal for Numerical Methods in Engineering* 35.2 (1992): 425-36. Print.
36. Babuška, Ivo, and Theofanis Strouboulis. *The Finite Element Method and Its Reliability*. Oxford England: Clarendon, 2001. Print.
37. Bilezikian, J. "Efficacy of Bisphosphonates in Reducing Fracture Risk in Postmenopausal Osteoporosis." *The American Journal of Medicine* 122.2 (2009): S14-21. Print.
38. Pazianas, Michael, Solomon Epstein, and Mone Zaidi. "Evaluating the Antifracture Efficacy of Bisphosphonates." *Reviews on Recent Clinical Trials* 4.2 (2009): 122-30. Print.
39. Green, J. O., T. Diab, M. R. Allen, B. Vidakovic, D. B. Burr, and R. E. Guldberg. "Three Years of Alendronate Treatment Does Not Continue to Decrease Microstructural Stresses and Strains Associated with Trabecular Microdamage Initiation beyond Those at 1 Year." *Osteoporosis International* 23.9 (2012): 2313-20. Print.
40. Allen, M. R., and D. B. Burr. "Changes in Vertebral Strength-density and Energy Absorption-density Relationships following Bisphosphonate Treatment in Beagle Dogs."*Osteoporosis International* 19.1 (2008): 95-99. Print.
41. Allen, Matthew R., and David B. Burr. "Bisphosphonate Effects on Bone Turnover, Microdamage, and Mechanical Properties: What We Think We Know and What We Know That We Don't Know." *Bone* 49.1 (2011): 56-65. Print.
42. FDA. *Possible Increased Risk of Thigh Bone Fracture with Bisphosphonates*. *U.S. Food and Drug Administration*. N.p., 13 Oct. 2010. Web. 20 Aug. 2012. <http://www.fda.gov/NewsEvents/Newsroom/PressAnnouncements/ucm229171.htm>.
43. Watts, N. B., and D. L. Diab. "Long-Term Use of Bisphosphonates in Osteoporosis." *Journal of Clinical Endocrinology & Metabolism* 95.4 (2010): 1555-565. Print
44. Hampson, Geeta, and Ignac Fogelman. "Clinical Role of Bisphosphonate Therapy."*International Journal of Women's Health* 4 (2012): 455-69. *NCBI*. NIH, 3 Sept. 2012. Web. 15 Mar. 2012. <http://www.ncbi.nlm.nih.gov/pmc/articles/PMC3469225/>.
45. Komatsubara, Satoshi, Satoshi Mori, Tasuku Mashiba, Jilliang Li, Kiichi Nonaka, Yoshio Kaji, Tomoyuki Akiyama, Kensaku Miyamoto, Yongping Cao, Jun Kawanishi, and Hiromichi Norimatsu. "Suppressed Bone Turnover by Long-Term Bisphosphonate Treatment Accumulates Microdamage but Maintains Intrinsic Material Properties in Cortical Bone of Dog Rib." *Journal of Bone and Mineral Research* 19.6 (2004): 999-1005. Print.
46. Forwood, M. "Bisphosphonates Are Associated with Microdamage Accumulation at Clinically Relevant Skeletal Sites in Beagles." *Bone* 27.4 (2000): 27. Print.
47. Chapurlat, Roland D., Monique Arlot, Brigitte Burt-Pichat, Pascale Chavassieux, Jean Paul Roux, Nathalie Portero-Muzy, and Pierre D. Delmas. "Microcrack Frequency and

Bone Remodeling in Postmenopausal Osteoporotic Women on Long-Term Bisphosphonates: A Bone Biopsy Study." *Journal of Bone and Mineral Research*22.10 (2007): 1502-509. Print.

48. Boyd, Steven K., Eva Szabo, and Patrick Ammann. "Increased Bone Strength Is Associated with Improved Bone Microarchitecture in Intact Female Rats Treated with Strontium Ranelate: A Finite Element Analysis Study."Bone 48.5 (2011): 1109-116. Print.
49. Liu, X. Sherry, Adi Cohen, Elizabeth Shane, Emily Stein, Halley Rogers, Shannon L. Kokolus, Perry T. Yin, Donald J. McMahon, Joan M. Lappe, Robert R. Recker, and X. Edward Guo. "Individual Trabeculae Segmentation (ITS)-based Morphological Analysis of High-resolution Peripheral Quantitative Computed Tomography Images Detects Abnormal Trabecular Plate and Rod Microarchitecture in Premenopausal Women with Idiopathic Osteoporosis." *Journal of Bone and Mineral Research* 25.7 (2010): 1496-505. Print.
50. Hansen, Stinus, Kim Brixen, and Claus H. Gravholt. "Compromised Trabecular Microarchitecture and Lower Finite Element Estimates of Radius and Tibia Bone Strength in Adults with Turner Syndrome: A Cross-sectional Study Using High-resolution-pQCT." Journal of Bone and Mineral Research 27.8 (2012): 1794-803. Print.
51. Amin S, S., D. L. Kopperdhal, L. J. Melton, 3rd, S. J. Achenbach, T. M. Therneau, B. L. Riggs, T. M. Keaveny, and S. Khosla. "Association of Hip Strength Estimates by Finite-element Analysis with Fractures in Women and Men." *Journal of Bone and Mineral Research* 26.7 (2011): 1593-600. Print.
52. Brosses, Emily, E. Jolivet, C. Travert, D. Mitton, and W. Skalli. "Prediction of the Vertebral Strength Using a Finite Element Model Derived from Low-dose Biplanar Imaging: Benefits of Subject-specific Material Properties." Spine 37.3 (2012): E156-162.PubMed. Web. 30 Oct. 2012.
53. Boutroy, Stephanie, Bert Van Rietbergen, Elisabeth Sornay-Rendu, Francoise Munoz, Mary L. Bouxsein, and Pierre D. Delmas. "Finite Element Analysis Based on In Vivo HR-pQCT Images of the Distal Radius Is Associated With Wrist Fracture in Postmenopausal Women." *Journal of Bone and Mineral Research* 23.3 (2008): 392-99. Print.
54. Pistoia, W. "Estimation of Distal Radius Failure Load with Micro-finite Element Analysis Models Based on Three-dimensional Peripheral Quantitative Computed Tomography Images." *Bone* 30.6 (2002): 842-48. Print.
55. Harrison, N., D. O'Mahoney, P. McDonnell, and P. McHugh. "Damage and Failure of Trabecular Bone with Non-linear Geometry and Inhomogeneous Material Properties."*Journal of Biomechanics* 39 (2006): S417. Print.
56. "Screening for Osteoporosis." *Recommendation Statement*. U.S. Preventive Services Task Force, July 2010. Web. 25 Oct. 2012. <http://www.uspreventiveservicestaskforce.org/uspstf10/osteoporosis/osteors.htm>
57. "STL 2.0 May Replace Old, Limited File Format." *STL 2.0 May Replace Old, Limited File Format*. Rapid Publishing, LLC, 2009. Web. 20 Sept. 2012. <http://www.rapidtoday.com/stl-file-format.html>.
58. "MeshLab." *MeshLab*. N.p., n.d. Web. 20 Sept. 2012. <http://meshlab.sourceforge.net/>.

59. Dalzell, N., S. Kaptoge, N. Morris, A. Berthier, B. Koller, L. Braak, B. Rietbergen, and J. Reeve. "Bone Micro-architecture and Determinants of Strength in the Radius and Tibia: Age-related Changes in a Population-based Study of Normal Adults Measured with High-resolution PQCT." *Osteoporosis International* 20.10 (2009): 1683-694. Print.
60. Verhulp, E., B. Van Rietbergen, and R. Huiskes. "Load Distribution in the Healthy and Osteoporotic Human Proximal Femur during a Fall to the Side." *Bone* 42.1 (2008): 30-35. Print.
61. Gong, He, Ming Zhang, Ling Qin, and Yajun Hou. "Regional Variations in the Apparent and Tissue-Level Mechanical Parameters of Vertebral Trabecular Bone with Aging Using Micro-Finite Element Analysis." *Annals of Biomedical Engineering* 35.9 (2007): 1622-631. Print.
62. Rhee, Yumie, June-Huyck Hur, Ye-Yeon Won, Sung-Kil Lim, Myong-Hyun Beak, Wen-Quan Cui, Kwang-Gyoun Kim, and Young Eun Kim. "Assessment of Bone Quality Using Finite Element Analysis Based upon Micro-CT Images." *Clinics in Orthopedic Surgery* 1.1 (2009): 40. Print.
63. Karim, Lamya, and Deepak Vashishth. "Role of Trabecular Microarchitecture in the Formation, Accumulation, and Morphology of Microdamage in Human Cancellous Bone." *Journal of Orthopaedic Research* 29.11 (2011): 1739-744. Print.
64. Tang, S.y., and D. Vashishth. "A Non-invasive in Vitro Technique for the Three-dimensional Quantification of Microdamage in Trabecular Bone." *Bone* 40.5 (2007): 1259-264. Print.
65. Pistoia, W., B. Van Rietbergen, E.-M. Lochmüller, C.a. Lill, F. Eckstein, and P. Rüegsegger. "Image-Based Micro-Finite-Element Modeling for Improved Distal Radius Strength Diagnosis." *Journal of Clinical Densitometry* 7.2 (2004): 153-60. Print.
66. Pipkin, A. C. "Constraints in Linearly Elastic Materials." *Journal of Elasticity* 6.2 (1976): 179-93. Print.
67. Todhunter, I., and Karl Pearson. *A History of the Theory of Elasticity and of the Strength of Materials, from Galilei to the Present Time.* Cambridge: University, 1886.*Google Book Search*. Web. 26 Oct. 2012.
68. Rajan, Krishna. "Linear Elastic Properties of Trabecular Bone: A Cellular Solid Approach."*Journal of Materials Science Letters* 4.5 (1985): 609-11. Print.
69. Tanabe, Yuji, and Koichi Kobayashi. "Anisotropy in the Dynamic Non-linear Viscoelastic Properties of Bovine Compact Bone." *Journal of Materials Science: Materials in Medicine* 5.6-7 (1994): 397-401. Print.
70. Joo, W.K., B.I. Kim, Sung In Bae, C.S. Kim, and Jung Il Song. "Mechanical Properties on Nanoindentation Measurements of Osteonic Lamellae in a Human Cortical Bone."*Key Engineering Materials* 353-358 (2007): 2248-252. Print.
71. Zamiri, A., and S. De. "Mechanical Properties of Hydroxyapatite Single Crystals from Nanoindentation Data." *Journal of the Mechanical Behavior of Biomedical Materials* (2010): 146-152. Print.
72. Carnelli, D., D. Gastaldi, V. Sassi, R. Contro, C. Ortiz, and P. Vena. "A Finite Element Model for Direction-Dependent Mechanical Response to Nanoindentation of Cortical Bone Allowing for Anisotropic Post-Yield Behavior of the Tissue." *Journal of Biomechanical Engineering* 132.8 (2010): 1-10. Print.

73. Hambli, R., A. Bettamer, and S. Allaoui. "Finite Element Prediction of Proximal Femur Fracture Pattern Based on Orthotropic Behaviour Law Coupled to Quasi-brittle Damage." *Medical Engineering and Physics* 34.2 (2012): 202-10. Print.
74. *Element Reference*. Apr. 2009. ANSYS Release 12.0 Element Reference. Http://www1.ansys.com/customer/content/documentation/120/ans_elem.pdf
75. Zysset, Philippe K., X. Edward Guo, C. Edward Hoffler, Kristin E. Moore, and Steven A. Goldstein. "Elastic Modulus and Hardness of Cortical and Trabecular Bone Lamellae Measured by Nanoindentation in the Human Femur." *Journal of Biomechanics* 32.10 (1999): 1005-012. Print.
76. Poole, Gene. "Ansys Equation Solvers: Usage and Guidelines." *Http://www.tynecomp.co.uk/*. Tynemouth Computer Services, Apr. 2002. Web. 2 Oct. 2012. <http://www.tynecomp.co.uk/Xansys/solver_2002.pdf>.
77. Eddy, William F. "A New Convex Hull Algorithm for Planar Sets." *ACM Transactions on Mathematical Software (TOMS)* 3.4 (1977): 398-403. Print.
78. Stein, E.M., X.S. Liu, T. L. Nickolas, A. Cohen, V. Thomas, D.J. McMahon, C. Zhang, P.T. Yin, F. Cosman, J. Nieves, X.E. Guo, and E. Shane. "Abnormal Microarchitecture and Reduced Stiffness at the Radius and Tibia in Postmenopausal Women with Fractures." *Journal of Bone and Mineral Research* 25.12 (2010): 2572-581. Print.
79. Motulsky, Harvey J. *The InStat Guide to Choosing and Statistical Tests*. 2001. Software Manual. Http://www.graphpad.com/downloads/InStat3Mac.pdf.
80. Harner, J. P., 3rd, and J. H. Wilson. "Bone Strength Statistical Distribution Functions for Broilers." Poultry Science 64.3 (1985): 585-87. Print.
81. Cohen, A., D. W. Dempster, R. R. Recker, E. M. Stein, J. M. Lappe, H. Zhou, A. J. Wirth, G. H. Van Lenthe, T. Kohler, A. Zwahlen, R. Muller, C. J. Rosen, S. Cremers, T. L. Nickolas, D. J. McMahon, H. Rogers, R. B. Staron, J. LeMaster, and E. Shane. "Abnormal Bone Microarchitecture and Evidence of Osteoblast Dysfunction in Premenopausal Women with Idiopathic Osteoporosis." *Journal of Clinical Endocrinology & Metabolism* 96.10 (2011): 3095-105. Print.
82. Follet, Helene, Stéphanie Viguet-Carrin, Brigitte Burt-Pichat, Baptiste Dépalle, Yohann Bala, Evelyne Gineyts, Francoise Munoz, Monique Arlot, Georges Boivin, Roland D. Chapurlat, Pierre D. Delmas, and Mary L. Bouxsein. "Effects of Preexisting Microdamage, Collagen Cross-links, Degree of Mineralization, Age, and Architecture on Compressive Mechanical Properties of Elderly Human Vertebral Trabecular Bone." *Journal of Orthopaedic Research* 29.4 (2010): 481-88. Print.
83. Ghosh, Anindya. "Journal of Textile and Apparel Technology and Management." *Spun Yarn Strength as a Function of Gauge Length and Extension Rate: A Critical Review*4.2 (2004): 1-13. Web. 17 Oct. 2012. <http://www.tx.ncsu.edu/jtatm/volume4issue2/Articles/Ghosh/Ghosh_full_99_04.pdf>.
84. Harrigan, Timothy P., Murali Jasty, Robert W. Mann, and William H. Harris. "Limitations of the Continuum Assumption in Cancellous Bone." Journal of Biomechanics 21.4 (1988): 269-75. Print.
85. Cohen, A., D. W. Dempster, R. Müller, X. E. Guo, T. L. Nickolas, X. S. Liu, X. H. Zhang, A. J. Wirth, G. H. Van Lenthe, and T. Kohler. "Assessment of Trabecular and Cortical Architecture and Mechanical Competence of Bone by High-resolution Peripheral Computed Tomography: Comparison with Transiliac Bone Biopsy." *Osteoporosis International* 21.1 (2010): 263-73. Print.

86. Chappard, Daniel, Nadine Retailleau-Gaborit, Erick Legrand, Michel Felix Basle, and Maurice Audran. "Comparison Insight Bone Measurements by Histomorphometry and CT." *Journal of Bone and Mineral Research* 20.7 (2005): 1177-184. Print.
87. J.B. Pialat, N. Vilayphiou, S. Boutroy, P.J. Gouttenoire, E. Sornay-Rendu, R. Chapurlat, F. Peyrin, Local topological analysis at the distal radius by HR-pQCT: Application to in vivo bone microarchitecture and fracture assessment in the OFELY study, Bone, Volume 51, Issue 3, September 2012, Pages 362-368, ISSN 8756-3282, 10.1016/j.bone.2012.06.008.
88. Vilayphiou, Nicolas, Roland Chapurlat, Pierre D. Delmas, Stephanie Boutroy, Pawel Szulc, Bert Van Rietbergen, and Francoise Munoz. "Finite Element Analysis Performed on Radius and Tibia HR-pQCT Images and Fragility Fractures at All Sites in Men."*Journal of Bone and Mineral Research* 26.5 (2011): 965-73. Print.
89. Wang, Xiang, Daniel B. Masse, Huijie Leng, Kevin P. Hess, Ryan D. Ross, Ryan K. Roeder, and Glen L. Niebur. "Detection of Trabecular Bone Microdamage by Micro-computed Tomography." *Journal of Biomechanics* 40.15 (2007): 3397-403. Print.
90. D L Kopperdahl and Tony M. Keaveny., "Yield strain behavior of trabecular bone" , J. Biomechanics,31,601-608, (1998).
91. Hernandez, J. D., K. Wesseling, R. Pereira, B. Gales, R. Harrison, and I. B. Salusky. "Technical Approach to Iliac Crest Biopsy." *Clinical Journal of the American Society of Nephrology* 3.Supplement 3 (2008): S164-169. Print.
92. Keaveny, Tony M., Robert E. Borchers, Lorna J. Gibson, and Wilson C. Hayes. "Trabecular Bone Modulus and Strength Can Depend on Specimen Geometry." *Journal of Biomechanics* 26.8 (1993): 991-1000. Print.
93. Noel M. Harrison, Pat F. McDonnell, Denis C. O'Mahoney, Oran D. Kennedy, Fergal J. O'Brien, Peter E. McHugh, Heterogeneous linear elastic trabecular bone modelling using micro-CT attenuation data and experimentally measured heterogeneous tissue properties, Journal of Biomechanics, Volume 41, Issue 11, 7 August 2008, Pages 2589-2596, ISSN 0021-9290, 10.1016/j.jbiomech.2008.05.014.
94. Tsafnat, Naomi, and Stephen Wroe. "An Experimentally Validated Micromechanical Model of a Rat Vertebra under Compressive Loading." Journal of Anatomy (2010): 40-46. Print.
95. Vico, L., Zouch, M., Amirouche, A., Frère, D., Laroche, N., Koller, B., Laib, A., Thomas, T. and Alexandre, C. (2008), High-Resolution pQCT Analysis at the Distal Radius and Tibia Discriminates Patients With Recent Wrist and Femoral Neck Fractures. J Bone Miner Res, 23: 1741–1750. doi: 10.1359/jbmr.080704
96. Ulrich, D., van Rietbergen, B., Weinans, H., and Rüegsegger, P., (1998), Finite Element Analysis of trabecular bone structure: a comparison of image-based meshing techniques, J. Biomech., 31, 1187-1192.
97. Grant Bevill, Senthil K. Eswaran, Farhad Farahmand, Tony M. Keaveny., "The influence of boundary conditions and loading mode on high-resolution finite element-computed trabecular tissue properties" , Bone,44,573-578, (2009).

98. Gomberg, B., P. Saha, and F. Wehrli. "Method for Cortical Bone Structural Analysis From Magnetic Resonance Images." *Academic Radiology* 12.10 (2005): 1320-332. Print.
99. Adachi, T., M. Tanaka, and Y. Tomita. "Uniform Stress State in Bone Structure with Residual Stress." *Journal of Biomechanical Engineering* 120.3 (1998): 342. Print.
100. Yamada, Satoshi, Shigeru Tadano, and Kazuhiro Fujisaki. "Residual Stress Distribution in Rabbit Limb Bones." *Journal of Biomechanics* 44.7 (2011): 1285-290. Print.
101. Bevill, Grant, and Tony M. Keaveny. "Trabecular Bone Strength Predictions Using Finite Element Analysis of Micro-scale Images at Limited Spatial Resolution." *Bone* 44.4 (2009): 579-84. Print.
102. J.H Keyak, Improved prediction of proximal femoral fracture load using nonlinear finite element models, Medical Engineering & Physics, Volume 23, Issue 3, April 2001, Pages 165-173, ISSN 1350-4533, 10.1016/S1350-4533(01)00045-5.
103. Macneil, J., and S. Boyd. "Bone Strength at the Distal Radius Can Be Estimated from High-resolution Peripheral Quantitative Computed Tomography and the Finite Element Method." *Bone* 42.6 (2008): 1203-213. Print.
104. Norman, Jonathan, Joe G. Shapter, Ken Short, Lachlan J. Smith, and Nicola L. Fazzalari. "Micromechanical Properties of Human Trabecular Bone: A Hierarchical Investigation Using Nanoindentation." *Journal of Biomedical Materials Research* 87A.1 (2007): 196-202. Print.
105. Rho, Jae-Young, Marcel Roy, and George M. Pharr. "Comments on 'Elastic Modulus and Hardness of Cortical and Trabecular Bone Lamellae Measured by Nanoindentation in the Human Femur'." Journal of Biomechanics 33.10 (2000): 1335. Print.
106. Viguet-Carrin, S., P. Garnero, and P. D. Delmas. "The Role of Collagen in Bone Strength." *Osteoporosis International* 17.3 (2006): 319-36. Print.
107. O'Mahony, Aisling M., John L. Williams, and Paulette Spencer. "Anisotropic Elasticity of Cortical and Cancellous Bone in the Posterior Mandible Increases Peri-implant Stress and Strain under Oblique Loading." *Clinical Oral Implants Research* 12.6 (2001): 648-57. Print.
108. Jesper Kabel, Bert van Rietbergen, Michel Dalstra, Anders Odgaard, Rik Huiskes, The role of an effective isotropic tissue modulus in the elastic properties of cancellous bone, Journal of Biomechanics, Volume 32, Issue 7, July 1999, Pages 673-680, ISSN 0021-9290, 10.1016/S0021-9290(99)00045-7.
109. Guo, Xiang-Dong E., Thomas A. McMahon, Tony M. Keaveny, Wilson C. Hayes, and Lorna J. Gibson. "Finite Element Modeling of Damage Accumulation in Trabecular Bone under Cyclic Loading." *Journal of Biomechanics* 27.2 (1994): 145-55. Print.

VITA

- Lucas Tyler Wilkerson

- Degrees Awarded:
  - Bachelors of Science in Mechanical Engineering
    - University of Kentucky
    - May 2010
- Professional Positions:
  - Aeronautical Engineer
    - Belcan Corporation: Advanced Engineering and Technology Division
    - May 2010 – present
  - Mechanical Engineering CO-OP
    - Lexmark International, Inc.: Color Fuser Development
    - May 2008 – May 2010
- Honors and Awards
  - University of Kentucky Multi-Year Fellowship
  - University of Kentucky Presidential Scholarship
  - Outstanding Mechanical Engineering Sophomore Award
  - John A. Brittain Scholarship
  - ASME Bluegrass Section Outstanding Scholar Award: Spring 2009